UNIVERSITAT DE BARCELONA

Magnetic Excitations Induced by Surface Acoustic Waves and Spin-Polarized Currents

Nahuel Statuto

PhD thesis

Magnetic Excitations Induced by Surface Acoustic Waves and Spin-Polarized Currents

Nahuel Statuto

under the supervision of

Dr. Ferran Macià Bros
Dr. Joan Manel Hernàndez Ferràs

UNIVERSITAT DE BARCELONA

Magnetic Excitations Induced by Surface Acoustic Waves and Spin-Polarized Currents

Programa de Doctorat en Física

AUTOR: Nahuel Statuto

DIRECTORS: Dr. Ferran Macià Bros i
Dr. Joan Manel Hernàndez Ferràs

TUTOR: Prof. Giancarlo Franzese

UNIVERSITAT DE
BARCELONA

I would like to dedicate this thesis to my loving parents ...

Contents

Preface

This thesis presents the most important results obtained during my years of undergraduate research under the supervision of Dr. Ferran Macià Bros and Dr. Joan Manel Hernàndez Ferràs at the Group of Magnetism at Universitat de Barcelona, and during my stay in the group of Prof. Andrew D. Kent at the Center for Quantum Phenomena at the New York University.

Data storage has grown from 0.5 MB per person in 1986 to 44.5 GB per person in 2007 exposing our appetite for ever-more memory at ever-increasing densities [1] . Implicitly we face the miniaturization of the magnetic devices with the evident low-power consumption assumption. Those technical requirements may become achievable through the study of the magnetization dynamics. The goal of this thesis is to explore and control the magnetization dynamics on magnetic multilayered thin films through two different techniques: the application of STRAIN and SPIN-POLARIZED CURRENTS, which represent lower-power consumption approaches to the control of magnetization dynamics compared with conventional techniques. This fact is reflected in the structure of the thesis that consists of a general introduction, Chapter 1, and then, two independent parts. Each part is divided in different chapters.

The first part of the thesis studies the magnetization dynamics induced by the application of dynamic strain on a magnetic material. The strain deforms the magnetic material and induces a change in the direction and intensity of the magnetic anisotropy. Therefore, the magnetic states are affected by this variation and align with the new direction of magnetic anisotropy inducing dynamics in the magnetization.

The second part of the thesis studies the magnetization dynamics induced by the application of spin-polarized current through the magnetic material that exchanges magnetic moment with the magnetic spins of the electrons in the current. The current density has to be high to induce dynamics on the magnetization ($\sim 10^6 - 10^7$ A/cm^2) and this requires in a reduction of the diameter of the electrical contact $50 - 200$ nm.

The ferromagnetic materials with nanometric thickness used in this thesis are magnetic materials widely used in research. Aside the purely scientific interest, these materials are potentially applicable in information and communication technologies working at high speed.

Magnetization Dynamics Induced by the Application of Oscillating Strain

This part of the thesis is divided in four chapters. The first of them is an introduction, which presents the main physical effect involved in the modification of magnetization through the deformation of a magnetic material: the magnetostriction effect. In addition, surface acoustic waves, which are responsible for inducing deformations dynamically to the magnetic nanomaterial, are defined. We also describe the measurement techniques that, in this part of the thesis, are based mainly on the use of a photoemission electron microscope (PEEM) that uses X-rays to extract magnetic information from the sample. The experiments have been carried out in the ALBA synchrotron, in Cerdanyola del Vallés. The second chapter of this part of the thesis deals with the technique related to the observation and quantification of surface acoustic waves with PEEM. The microscope gives us spatial resolution whereas the pulses of X-rays of the ALBA (pulses of 20 ps) allow us to obtain temporal resolution. Surface acoustic waves travel on the surface of a piezoelectric material that, when deformed, produces a piezoelectric voltage wave. In addition, by confronting two surface acoustic waves we study their interference and the possibility of exciting surface acoustic waves that do not propagate. Standing surface acoustic waves may fix a strain pattern on both the piezoelectric material and on any material deposited on top.

In the third chapter we study nanostructures of $2\times2\mu$m^2 that present a magnetic state with a vortex in the center and four magnetic domains forming a closed

flux. Surface acoustic waves modify the size of each of the four magnetic domains that grow or shrink depending on the phase of the acoustic wave. The main result of this chapter is the simultaneous resolution at the picosecond and nanometer scale of the induce strain and the corresponding magnetic response on the nanostructures. We also proved that manipulation of the magnetization dynamics with surface acoustic waves at the picosecond scale is as efficient as the case with static strain. Finally, we obtain a delay between the surface acoustic waves and their effect on the magnetic states, which depends on the coupling between of the magnetic states with the magnetic resonances.

The fourth chapter of this part of the thesis studies the effect of surface acoustic waves on a thin film of Nickel that extends by $2-3$ mm. We apply surface acoustic waves after the sample is uniformly magnetized with an external magnetic field. A pattern of spin waves appears on the Nickel thin film induced by surface acoustic waves. We also observe that changing the wavelength of the surface acoustic waves changes the wavelength of the magnetic pattern. The main result of this chapter is the observation of spin waves that propagate several millimeters through the Nickel thin film.

The results of this part of the thesis have been mostly published in scientific journals. The technical results of the second chapter have been published in *Journal of Synchrotron Radiation* [2], the results of the third chapter have been published in *Nature Communitations* [3] and the results of the fourth chapter are being prepared for submission.

Magnetization Dynamics Induced by the Spin-Polarized Current

This part of the thesis is divided into three chapters. The first one is an introduction, where the main physical effect involved in the modification of magnetization through the application of spin-polarized currents is presented: the spin-transfer effect. In addition, the first chapter contains a detailed explanation of the sample used in experiments and the measurement techniques based on the giant magnetoresistance effect. The sample consists of two thin magnetic layers separated by a thin layer of a non-magnetic material. One of the magnetic layers (10 nm) is thicker than the other and is used to polarize the current that may induce dynam-

ics in the magnetization of the other layer (4 nm). These two layers are known as *polarizer* and *free layer*. The free layer, where we will investigate the magnetization dynamics, is composed of a combination of layers of Cobalt and Nickel that form a layer that presents perpendicular magnetic anisotropy. Finally, we patterned electrical contacts of a non-magnetic metal, which is used to contact the magnetic layer in a small region, $100-150$ nm in diameter.

The free layer has magnetic damping that is responsible for reducing the magnetization dynamics. If the current passing through the contact is sufficiently large, the effect can compensate the damping allowing the excitation of the magnetization in the form of spin waves. In particular, if these spin waves are localized, a change in the direction of the magnetization may be obtained in the region where the current passes—the nanocontact. This magnetic configuration is known as dissipative magnetic droplet and it is the object of study in the following chapters.

The second chapter of this part of the thesis studies the stability of dissipative magnetic solitons at room and low temperature (4 K). Room-temperature experiments show the existence of low-frequency spectrum ($\sim 10-1000$ MHz) that we attribute to the movement of magnetic object as a whole in the nanocontact region. Then, using micromagnetic simulations, we obtain some possible origins of the low-frequency movement. In general, any non-symmetric distribution of effective field experienced by the magnetic object produces a transverse force that displaces it outside the nanocontact region where damping dominates and destroys it. At the same time, the current applied in the nanocontact recreates it, in a process with a frequency of a few hundreds of MHz. Low-temperature experiments show that these magnetic objects can present more than one stable state with different oscillation frequencies. These states can be "chosen" through the application of both out-of-plane and in-plane external magnetic fields. In addition, we observed a correlation between the appearance of a signal at a low frequency and the instability of the magnetic state.

The third chapter of this part of the thesis focuses on the processes of creation and annihilation of magnetic droplet. This chapter presents two well differentiated parts. In the first, both processes are studied with micromagnetic simulations and in the other part, experiments are carried out with the application of nanosecond pulses of spin-polarized current at room temperature. The theoretical study fo-

cuses on the initial parameters that lead to the creation of dissipative magnetic solitons. We investigate how these parameters can determinate the topology of the resulting soliton. In particular, solitons without topology called *droplets* (whose magnetic configuration can be continuously deformed to a state where all spins are parallel) are studied and compared with topological solitons, with the topology of a circle and known as *dynamical skyrmions* (whose magnetization can not be continuously deformed to a state of parallel spins). Experiments with spin-polarized current pulses show that the characteristic times of the creation (of the order of μs) and of the annihilation (of the order of the ns) of these objects are different. Again, using simulations, we study these processes. We observe that creation is affected by what we call waiting time: the time necessary to initiate the magnetization dynamics before the creation process. This waiting time depends on the initial state of the magnetization and we show how to reduce it or extend it with the application of external magnetic fields.

The results of this part of the thesis have also been published in scientific journals. The results on stability at low and high temperature have been published in two issue of *Physical Review B* [4, 5], the experimental results of creation and annihilation of droplets were published in *Scientific Reports* [6] and the theoretical results on the creation of topological objects have been published in *Nanotechnoly* [7].

The thesis has an appendix where the simulation software is explained. All simulations were performed with MuMax3, a GPU-accelerated micromagnetic simulations program. The code of the principal simulation can be found in Appendix A.

Resumen en Castellano

En esta memoria de tesis se presentan los resultados más importantes obtenidos durante mis estudios de doctorado en el Grupo de Magnetismo y Superconductividad de la Universidad de Barcelona bajo la supervisión de Dr. Ferran Macià Bros y Dr. Joan Manel Hernàndez Ferràs y durante mi estancia en la universidad de New York bajo la supervisión de Prof. Andrew D. Kent.

La tesis gira en torno al estudio de la dinámica de la magnetización en capas y multicapas delgadas ferromagnéticas. Sin embargo, los sistemas estudiados son diversos y pueden clasificarse por la técnica utilizada para la excitación de la dinámica de la magnetización. Este hecho queda plasmado en la estructura de la tesis que consta de una introducción general, Capítulo 1, y luego de dos partes independientes y separadas, a su vez, en varios capítulos. El orden en la exposición de los resultados pretende seguir una linea lógica para su compresión. Como contrapartida, los resultados son presentados sin seguir un orden cronológico.

La primera parte de la tesis estudia la dinámica de la magnetización inducida por la aplicación de tensión dinámicamente sobre el material magnético, que al deformarlo induce en él un cambio en la dirección e intensidad de la anisotropía magnética. Por lo tanto, los estados magnéticos se ven afectados por esta variación y cambian para alinearse con la nueva dirección de anisotropía magnética induciendo dinámica en la magnetización.

La segunda parte de la tesis estudia la dinámica de la magnetización inducida por la aplicación de corriente polarizada a través del material magnético que intercambia momento magnético con los espines magnéticos de los electrones de la corriente. Para que esta transferencia de momento magnético sea efectiva la densidad de corriente ha de ser elevada ($\sim 10^6 - 10^7$ A/cm^2) y para conseguirla se reduce hasta los $50 - 200$ nm el diámetro del contacto eléctrico.

Los materiales ferromagnéticos con grosor nanométrico usados en esta tesis son materiales magnéticos usados ampliamente en la investigación. Aparte del interés puramente científico, estos materiales son potencialmente aplicables en telecomunicaciones o tecnologías del almacenaje y transmisión de información a altas velocidades.

Dinámica de la Magnetización Inducida por la Aplicación de Tensión

Esta parte de la tesis esta dividida en cuatro capítulos. El primero de ellos es una introducción al tema, donde se presenta el principal efecto físico implicado en la modificación de la magnetización a través de la deformación de un material magnético: la magnetostricción. Además, se definen las ondas acústicas superficiales que serán las responsables de inducir deformaciones al nanomaterial magnético de forma dinámica. Finalmente, se explican las técnicas de medida que, en esta parte de la tesis, se basan principalmente en la utilización de un microscopio electrónico por fotoemisión que necesita de rayos X para extraer electrones de la muestra. Por lo tanto, los experimentos han sido llevados a cabo en el sincrotrón ALBA, en Cerdanyola del Vallés, donde los electrones utilizados para formación de imágenes son, una vez se excitan en la muestra, acelerados al microscopio por una diferencia de potencial de unos 20kV. La combinación de ondas acústicas superficiales con microscopía electrónica no es común dada la complejidad técnica que representa la introducción de las ondas acústicas superficiales en el montaje estándar de un microscopio electrónico. Por lo tanto, el segundo capítulo de esta parte de la tesis trata sobre la técnica de observación y cuantificación de las ondas acústicas superficiales con un microscopio electrónico por fotoemisión. El microscopio nos da resolución espacial y los pulsos de rayos X del ALBA (pulsos de 20 ps) nos permite obtener resolución temporal. Las ondas acústicas superficiales viajan sobre la superficie de un material piezoeléctrico que al deformarse produce una onda de voltaje piezoeléctrico. Esta técnica permite la observación directa de la onda piezoeléctrica y la cuantificación la tensión o deformación que podemos aplicar sobre cualquier material depositado posteriormente sobre el piezoeléctrico. Además confrontando dos ondas acústicas superficiales estudiamos su interferencia y la posibilidad de excitar ondas acústicas superficiales que

no se propaguen, fijando así un patrón de deformación tanto sobre el material piezoeléctrico como sobre cualquier material que se deposite encima.

El tercer y cuarto capítulo de esta parte de la tesis estudia, con las técnicas anteriormente desarrolladas, el efecto de las ondas acústicas superficiales sobre nanoestructuras (tercer capítulo) y capas delgadas (cuarto capítulo) de níquel depositadas sobre el material piezoeléctrico. En ambos casos, el níquel depositado presenta anisotropía magnética unidireccional dentro del plano y tiene un espesor de unos 20 nm.

En el tercer capítulo se estudian nanoestructuras de $2\times2\mu m^2$ que presentan un estado magnético con un vórtice en el centro y cuatro dominios magnéticos formando un flujo cerrado. La introducción de las ondas acústicas superficiales modifica el tamaño de cada uno de los cuatro dominios magnéticos que crecen si se encuentran sobre un mínimo de la onda acústica o se reducen si se hallan sobre un máximo. El resultado principal de este capítulo es la resolución simultánea en picosegundos y nanómetros de la onda de tensión causada por las ondas acústicas superficiales y su correspondiente respuesta magnética sobre los estados magnéticos de los cuadrados de níquel. Además probamos que la manipulación de la dinámica de la magnetización con tensión dinámica posible de forma eficiente en la escala del picosegundo. Finalmente, se obtiene el cálculo del retraso entre las ondas acústicas superficiales y su efecto sobre los estados magnéticos. Hemos observado que el retraso puede variar si la excitación de los estados magnéticos se acopla con resonancias magnéticas propias de la configuración magnética de las nanoestructuras.

El cuarto, y último, capítulo de esta parte de la tesis estudia el efecto de las ondas acústicas superficiales sobre una capa delgada de níquel que se extiende por $2-3$ mm. Tras la aplicación de un campo magnético externo para magnetizar uniformemente la muestra se aplican las ondas acústicas superficiales. Sobre el estado magnético de la capa delgada de níquel aparece un patrón de ondas de espín inducido por las ondas acústicas superficiales y al cambiar la longitud de onda de las ondas acústicas superficiales también cambia la longitud de onda del patrón magnético. El resultado principal de este capítulo es la observación de ondas de espín que se propagan varios milímetros por la capa delgada de níquel y de las que podemos controlar su amplitud y su longitud de onda.

Los resultados de esta parte de la tesis han sido publicados en revistas científicas. Los resultados más técnicos del segundo capítulo han sido publicados en la revista *Journal of Synchrotron Radiation* [2], los resultados referentes a las nanoestructuras del tercer capítulo han sido publicadas en *Nature Communitations* [3] y los resultados del cuarto capítulo están siendo preparados para enviar a publicar.

Dinámica de la Magnetización Inducida por la Aplicación de Corriente Polarizada

Esta parte de la tesis esta dividida en tres capítulos. El primero de ellos es una introducción al tema, donde se presenta el principal efecto físico implicado en la modificación de la magnetización a través de la aplicación de corrientes polarizadas: transferencia de momento de los espines. Además, contiene una explicación detallada de la muestra que utilizaremos y las técnicas de medida basadas principalmente en el efecto de magnetoresistencia gigante. La muestra está compuesta por 2 capas delgadas magnéticas separadas por una capa delgada de un material no magnético. Una de las capas magnéticas (de 10 nm) es más gruesa que la otra y se utiliza para polarizar la corriente que luego inducirá dinámica en la magnetización de la otra capa (de 4 nm). Estas dos capas se conocen como *polarizador* y *capa libre*. La capa libre, donde investigaremos la dinámica, está compuesta de una combinación de capas de cobalto y níquel que conforman una capa que presenta anisotropía magnética en la dirección perpendicular a la capa. Finalmente, la muestra multicapas resultante tiene electrodos para poder pasar corriente a través de ella. En los experimentos estos contactos eléctricos tienen entre $100-150$ nm de diámetro.

La capa libre presenta amortiguamiento magnético que es el responsable de reducir la dinámica de la magnetización, pero si la corriente es suficiente, la excitación puede compensar el amortiguamiento permitiendo así la excitación de la magnetización en forma de ondas de espín. En particular, si estas ondas de espín son localizadas, se puede obtener un cambio en el sentido de la magnetización en la región donde pasa la corriente—el nanocontacto. Esta configuración magnética es conocida como solitones magnéticos disipativos y los siguientes capítulos se centran en el estudio de estos objetos magnéticos.

El segundo capítulo de esta parte de la tesis estudia la estabilidad de los solitones magnéticos disipativos a temperatura ambiente y a baja temperatura (4 K). Los experimentos a temperatura ambiente muestran la existencia de espectro de baja frecuencia ($\sim 10-1000$ MHz) que atribuimos al movimiento de objeto magnético como un todo en la región del nanocontacto. Luego, con la ayuda de simulaciones micromagnéticas obtenemos algunos posibles orígenes del movimiento de baja frecuencia. En general, cualquier distribución no simétrica del campo efectivo que experimenta el objeto magnético produce una fuerza transversal que lo desplaza lateralmente fuera del nanocontacto. En cuanto se sale de esta región, el amortiguamiento domina y se destruye. A la vez, la corriente aplicada en el nanocontacto vuelve a crearlo, en un proceso con una frecuencia de unos cientos de MHz. Los experimentos a baja temperatura muestran que estos objetos magnéticos pueden presentar más de un estado estable con diferentes frecuencias de oscilación y que estos estados pueden ser "escogidos" a través de la aplicación de campos magnéticos externos tanto en perpendiculares como paralelos a la capa magnética. Además, observamos una correlación entre la aparición de señal a baja frecuencia con la inestabilidad del estado magnético.

El tercer, y último, capítulo de esta parte de la tesis se centra en los procesos de creación y destrucción de estos objetos magnéticos. Este capítulo presenta dos partes bien diferenciadas. En la primera se estudian ambos procesos de forma teórica con simulaciones micromagnéticas y en la otra parte, se llevan a cabo experimentos con la aplicación de pulsos de nanosegundos de corriente polarizada a temperatura ambiente. El estudio teórico se centra en los parámetros iniciales que conllevan a la creación de los solitones magnéticos disipativos. Además, se investiga como estos parámetros pueden influir en la topología final del soliton resultante. En particular se estudian y comparan solitones sin topología llamados *droplets* (cuya configuración magnética se puede deformar continuamente hasta un estado donde todos los espines sean paralelos) con solitones topológicos, con la topología de un circulo y conocidos como *dynamical skyrmions* (cuya magnetización no puede ser continuamente deformada hasta un estado de espines paralelos). Los experimentos llevados a cabo a temperatura ambiente con pulsos de corriente polarizada muestran que los tiempos característicos de la creación (del orden de los μs) y de la destrucción (del orden de los ns) de estos objetos

son distintos. Otra vez, sirviéndonos de simulaciones, estudiamos estos procesos y observamos que la creación está afectada por lo que llamamos un tiempo de espera, el tiempo necesario para iniciar la dinámica de la magnetización antes del proceso de creación. Este tiempo de espera depende del estado inicial de la magnetización y aprendemos a reducirlo o extenderlo con la aplicación de campos externos.

Los resultados de esta parte de la tesis también han sido en su mayoría publicados en revistas científicas. Los resultados sobre estabilidad a baja y alta temperatura han sido publicados en dos número de la revista *Physical Review B* [4, 5], los resultados experimentales de creación y destrucción de droplets fueron publicados en la revista *Scientific Reports* [6] y los resultados teóricos sobre la creación de objetos topológicos han sido publicados en la revista *Nanotechnoly* [7].

Acknowledgements

Dear reader, as I have said before, this thesis presents the most important results of my years as PhD student. However, it does not reflect anywhere the help that, during all this time, I have received from advisors, lab mates and office mates, family and friends. Excuse me to switch to Spanish and for the length of this section.

Empiezo por el principio y la primera persona a la que tengo que agradecer es a Javier Tejada. Sin la infinita pasión que ponés en tus clases probablemente estaría en otro lugar. Me abriste las puerta al Lab y a la física experimental de las probatinas y los ordenes de magnitud. Gracias.

En 2014 ya vivía en Sants. Mi casa está a unos 3 km de la facultad, por lo que casi siempre iba en bicicleta hasta allí y por aquel entonces Ferran Macià, al que solo había visto 2 veces en el congreso Coma Ruga 2014, ya vivía por allí y también iba y venía en bicicleta. Eso fue clave en mi doctorado, ir en bici a la facultad. Un día por la tarde bajando en bicicleta por Rambla de Badal me encontré con Ferran que también iba a su casa y estuvimos hablando sobre mi futuro. Le planteé mis dudas y él me dijo que me pasara por su despacho y que me contaría que cosas estaba haciendo por si me interesaba. Y así lo hice... y al poco tiempo empecé el doctorado. Gracias Ferran por las infinitas clases particulares de física. Siempre tenés a mano un papel en sucio con el que hacés dos dibujitos y todo parece más fácil. Nunca acabé una conversación con vos sin la sensación de haber aprendido algo y sin estar un poco más motivado. Gracias por transmitir tu entusiasmo sobre cada problema y por ayudarme a afrontarlos.

La vida social y científica del GMAG se lleva a cabo en el Laboratorio 4.22 y el *Lord of the Lab* se llama Joan Manel Hernàndez Ferràs. JM, sos la persona con más intuición física que conozco. Siempre tenés una respuesta para dar que

parece que lleves meses pensando. Gracias por tu inquietud infinita por solucionar cualquier problema y por hacer que el Lab sea un lugar en el que uno se sienta a gusto. He aprendido mucha física viéndote montar (y muchas veces desmontar) experimentos que siempre acaban funcionando. Gracias por la música en el Lab.

El resto del GMAG, Diego, Toni, Sergi, Ricardo, Martí y mi muy querido Juanito. Sin ustedes el GMAG solo sería un grupo de investigación de la UB, no habría asados, ni almuerzos, ni música en el Lab, ni nada. Juanito: mi soporte, y creo que soporte mutuo, en el grupo. ¡Gracias Gian por todo! Por los consejos, los ratos hablando de todo menos física y por esas mañanas cuando cantabas tres notas (a veces en acorde mayor y otras en menor) y gracias a eso sabíamos si sería un buen día o uno de mierda. Sin tus imitaciones mis días son más aburrido.

Jaume, el químico, con el que gasté unos 100 km de teflón. Gracias por los ratos de discusiones científicas, por compartir nuestros primeros experimentos juntos con el SQUID (¡no el bicho marino!) y por pelearnos hasta ganarle a la maldita caña porta muestra.

¡Cuqui! Sin vos no me hubiera reído ni un 15 % de lo que me he reído. Nuestro viaje a USA fue un *hanging out* constante y las noches de sincrotrón con el acordeón, la trompeta y tus inacabables cigarros se quedan para siempre en la memoria. Gracias Blai.

I also want to thank Andy Kent and Chris Hahn for the time I was at NYU. Discuss with them made me feel at home. At NYU it was the first time I spent a night measuring in the lab. In fact, I spent the previous 3 nights to return to Barcelona, which resulted in part of Chapter 7. Thank you.

El despacho 4.11 abandonado de la mano de las estadísticas, 3 diestros y 3 zurdos. Gracias a todos y todas por las charlas y los ratos de desconexión. Gracias Gian, Guille, Mariona, Ana y Elisenda.

Fuera de la universidad Mireia es sin duda la que más a sufrido mi tesis. Me ha escuchado y cuidado mucho, sobre todo en esta etapa final. Gracias Pelonzita.

Mi familia, viejos y hermana, son uno de los pilares de mi estabilidad mental. Ellos saben lo que pienso con solo atenderme el teléfono o mirarme por un segundo, y muchas veces no fui todo lo agradecido que requería la situación. Gracias por no mandarme a la mierda todas las veces que me lo he merecido.

Los pibes. Gracias a todos los amigos que han estado escuchando mis tonterías. Algunos más seguido como los de la comitiva de Sants (Nachito, Kiko y File) y los Quadrivers (Blai G, Blai P_{2do}, Guille, Gian y Matt) y otros no tanto por la distancia como Pepito y Gonza. Gracias Julius por los mates en la font del gat.

Amor, familia y amigos, los 3 pilares de la vida, pero yo tengo 4. La música es otro pilar de mi vida y si digo música digo Matt y Seuma. Me hace mejor media hora de ensayo que un día sin trabajar. Gracias.

Y no puedo olvidarme de Jade; llevarte al pipican por las mañanas con sol me hacen mejor a mi que a vos.

En fin, como dijo Cerati: Gracias totales.

Chapter 1

General Concepts of Magnetism at the Mesoscale

Magnetic materials used in telecommunications and information technology must be as small as possible. Miniaturization allows more storage capacity and lower costs in the production of new technologies. As new and smaller materials are fabricated, new phenomena appear and thus new physics is needed to describe them. The length scale of the emerging magnetic materials, in the order of the nanometer, is the meeting point of both the microscopic quantum world and the macroscopic classic world—the *mesoscale*. Magnetic thin films with nanometric thicknesses are mesoscopic systems that can be combined in magnetic multilayers to obtain new properties arising from the combination of different magnetic materials. Multilayers are of special interest since they can exhibit giant magnetoresistance, which opens a door to applications in data storage technology and magnetic sensing.

The magnetic state of thin films, or multilayers, is determined by the competition of magnetic energies involved in the system. Systems evolve to a final state, which can be dynamic or not, minimizing the total energy and resulting sometimes in magnetic textures different from the uniform state with all spins pointing in a same direction. Control of the evolution of the magnetization is a key process to develop faster devices and technologies, and it implies working at the sub-nanosecond timescale. In this dissertation we study new means to control

the dynamics of magnetization in different magnetic multilayer systems through the application of a strain wave and a spin-polarized current.

In this chapter we study the energies involved in the magnetism of materials. We present the general formalism followed throughout the thesis. The study of the mesoscale requires a semi-classical description of magnetic systems. We generalize the formalism to the semi-classical limit from the quantum origin. In addition, we also introduce the formalism for the study of magnetization dynamics. The most relevant features of nano- and micro-magnetism are described in this chapter. More detailed and rigorous coverage may be found elsewhere, e.g., in the book of J. Stöhr and H. C. Siegmann [8] or S. Bullet [9].

1.1 Magnetic Moment

The magnetic moment, $\boldsymbol{\mu}$, of a magnet is defined as a quantity that determines the torque that a magnetic field will exert on it. A loop of electric current, a bar magnet, an electron, and an atom all have magnetic moments. The total magnetic moment of a body is a certain combination of the magnetic moments of its components, that may interact in very different ways.

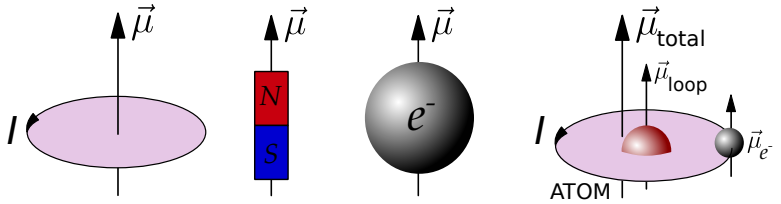

Figure 1.1 **Magnetic moments**. Classical representation of the magnetic moment of a loop of electric current, a bar magnet, an electron, and an atom.

The magnetic moment of an electron, the smallest components of a body has two microscopic contributions: *orbital motion* and *spin*

$$\boldsymbol{\mu}_{\mathrm{l}} = \gamma_{\mathrm{e}} \hbar \boldsymbol{l}, \qquad \boldsymbol{\mu}_{\mathrm{s}} = g_e \gamma_{\mathrm{e}} \hbar \boldsymbol{s},$$

where $\gamma_{\mathrm{e}} = e/2m_e$ is the gyromagnetic factor, with e the charge of the electron and m_{e} its mass, $g_e \approx 2$ the electron spin g-factor, $\boldsymbol{l}$ is the orbital momentum and $\boldsymbol{s}$ the

spin quantum number. These relations can be rewritten as

$$\boldsymbol{\mu}_l = \mu_B \boldsymbol{l}, \qquad \boldsymbol{\mu}_s = -g_e \mu_B \boldsymbol{s},$$

where $\mu_B = \hbar|\gamma_e| = 9.27 \cdot 10^{-24}$ Am^2 is the *Bohr magneton*, that gives the units of quantization of the magnetic moment of the electron.
In an atom with a total orbital momentum $\boldsymbol{L} = \sum_i \boldsymbol{l}_i$ and total spin $\boldsymbol{S} = \sum_i \boldsymbol{s}_i$, the total angular momentum is given by the operator $\boldsymbol{J} = \boldsymbol{L} + \boldsymbol{S}$, and hence its magnetic moment would be $\boldsymbol{\mu} = \gamma\hbar\boldsymbol{J}$.

In the classical description of ferromagnetic materials, one has to take an average of the magnetic moment on a small volume V_0 containing a large number of atoms that are still small to maintain a uniform alignment of spins. Hence, we can define the *magnetization* $\boldsymbol{M}(\boldsymbol{r})$ as a "magnetic moment density", and the magnetic moment distribution $\boldsymbol{\mu}(\boldsymbol{r})$ on a body of volume V is given by

$$\boldsymbol{\mu}(\boldsymbol{r}) = \int_V \mathrm{d}^3 r \, \boldsymbol{M}(\boldsymbol{r}).$$

Additional Information 1.1

The *nuclear magneton* is defined as $\mu_N = \hbar|\gamma_N|$, where $\gamma_N = e/2m_N$. Since $m_N = 10^3 m_e$, the nuclear magnetic moment results smaller than the electronic magnetic moment, $|\boldsymbol{\mu}_N| \approx 10^{-3}|\boldsymbol{\mu}_e|$, and the total magnetic moment of an atom is usually approximated by the electronic magnetic moment. However, the nuclear magnetic moment has a lot of applications, such as nuclear magnetic resonance.

1.2 Magnetic Energy Terms

There exist several sources of energy in magnetic systems. Some of those energies are reviewed in this section. For the sake of simplicity of vocabulary we restrict the following discussion to ferromagnetic materials, although all aspects may be extended to other types of magnetic ordering. The balance between the different energies in a system determines its ground state. In the following, we describe the

most important energies that determine the state of a magnetic system. The first energy term that we are going to study, the Zeeman energy term, is not intrinsic to the magnetic material and depends on the external magnetic field. However, we start with the Zeeman term since some of the others energies are usually written in a similar way.

1.2.1 Zeeman Energy

The *Zeeman energy* term is related with the application of an external magnetic field. The energy of an external field acting on a magnetic moments is

$$E = -\boldsymbol{\mu} \cdot \boldsymbol{B}_0.$$

This effect holds whatever is the origin of the magnetic moment, i.e., classical or quantum. Hence, when acting on a quantum spin $\boldsymbol{s}$ it can be expressed as

$$\mathscr{H}_{\text{Zeeman}} = -\gamma \hbar \boldsymbol{s} \cdot \boldsymbol{B}_0,$$

and in the classical approximation it takes the form

$$E_{\text{Zeeman}} = -\mu_0 \int \mathrm{d}^3 r \; \boldsymbol{M}(\boldsymbol{r}) \cdot \boldsymbol{H}_0. \tag{1.1}$$

This equation shows us that the energy minimum occurs when the magnetization, $\boldsymbol{M}(\boldsymbol{r})$, and the external field, $\boldsymbol{B}_0$, are pointing in the same direction.

1.2.2 Exchange Energy

In ferromagnets, the exchange interaction is related to the Pauli exclusion principle: two electrons with the same spin cannot be in the same spatial state (orbital). Therefore, if the orbitals of the unpaired outer valence electrons from adjacent atoms overlap, the electrostatic energy of the electrons is reduced when their spins are parallel compared to their energy when the spins are anti-parallel, so the parallel-spin state is more stable. In simple terms, the electrons, which repel one another, can move "further apart" by aligning their spins, so the spins of these electrons tend to line up. This difference in energy is called the *exchange energy*

and is described in a simple model, Heisenberg model, with the Hamiltonian

$$\mathscr{H}_{\mathrm{ex}} = -\sum_{n<m} J_{\mathrm{nm}} \boldsymbol{s}_{\mathrm{n}} \cdot \boldsymbol{s}_{\mathrm{m}},$$

where the interaction is between spins $\boldsymbol{s}_{\mathrm{n}}$ and $\boldsymbol{s}_{\mathrm{m}}$, the index n and m denoting positions, and J_{nm} is the exchange constant or exchange integral, which quantifies the energy difference between parallel and anti-parallel alignment of electron spins (for anti-ferromagnets J_{nm} should be negative).

In the classical limit the exchange energy is written

$$E_{\mathrm{ex}} = -\frac{1}{2(\gamma\hbar)^2} \int \mathrm{d}^3 r \int \mathrm{d}^3 r' \, J(r-r') \boldsymbol{M}(\boldsymbol{r}) \cdot \boldsymbol{M}(\boldsymbol{r}').$$

The exchange constant, $J(r-r')$, decreases rapidly with increasing $|r-r'|$, and the expression is reduced, through series expansion up tho the quadratic term, to

$$E_{\mathrm{ex}} = \frac{\mu_0}{2} \int \mathrm{d}^3 r \, \alpha_{\mathrm{ij}} \Big(\frac{\partial \boldsymbol{M}}{\partial r_{\mathrm{i}}} \cdot \frac{\partial \boldsymbol{M}}{\partial r_{\mathrm{j}}} \Big),$$

where

$$\alpha_{\mathrm{ij}} = \alpha_{\mathrm{ji}} = -\frac{1}{2(\gamma\hbar)^2} \int \mathrm{d}^3 r \, J(\boldsymbol{r}) r_{\mathrm{i}} r_{\mathrm{j}}$$

is the *exchange stiffness tensor* and $i, j = x, y, z$. Moreover, in the case of an isotropic material $\alpha_{\mathrm{ij}} = \alpha \delta_{\mathrm{ij}}$, we found the common expression

$$E_{\mathrm{ex}} = A_{\mathrm{ex}} \int \mathrm{d}^3 r \, \nabla^2 \boldsymbol{M}, \tag{1.2}$$

where A_{ex} ($= \mu_0 \alpha / 2 = 2JS^2 N/a$) is the *exchange constant*, being a the nearest neighbor distance (i.e., cell size) and N, the number of sites in the unit cell.

1.2.3 Magnetocrystalline Anisotropy Energy

If we consider a magnet in absence of external magnetic field (no Zeeman energy) and uniformly magnetized (no Exchange energy) the magnetization presents no restriction on its direction in space. However, in real systems, the internal

energy depends on the direction of $\boldsymbol{M}$ with the underlying crystalline direction of the solid. This arises from the combined effect of crystal-field effects (coupling electron orbitals with the lattice) and spin-orbit effects (coupling orbital with spin moments). This internal energy is called *magnetocrystalline anisotropy energy*, E_{mc}. The consequence of E_{mc} is the tendency for magnetization to align along certain axes (or in certain planes) of a solid, called easy directions. The anisotropy of a crystal depends on the lattice symmetry, and it may be uniaxial, biaxial, cubic, etc. The expression for a crystal geometry may be obtained taking into account that the energy should be invariant under rotation of the magnetization. This imposes the terms entering the energy to be even powers of the spin components or, equivalently, of the direction cosines. Limiting ourselves up to the 4th order, the general expression of the Hamiltonian is

$$\mathscr{H}_{\mathrm{A}} = b_{\mathrm{ij}}\boldsymbol{s}_{\mathrm{i}}\boldsymbol{s}_{\mathrm{j}} + c_{\mathrm{ijkl}}\boldsymbol{s}_{\mathrm{i}}\boldsymbol{s}_{\mathrm{j}}\boldsymbol{s}_{\mathrm{k}}\boldsymbol{s}_{\mathrm{l}} + \cdots,$$

where b_{ij} and c_{ijkl} are the tensors of the second rank and fourth rank, and summation over indices $i, j, k, l = x, y, z$ has been omitted. This Hamiltonian in the case of *uniaxial anisotropy* along the Z axis, with spin forming an angle θ with the axis, and dropping out the higher term (the second order term dominates in the majority of cases at room temperature [10]) becomes

$$\mathscr{H}_{\mathrm{A}} = -DS_{\mathrm{z}}^2,$$

with D being a constant, and S_{z} the spin projection in the Z axis. If $D > 0$, the energy is minimum when the spin is aligned along the Z axis, the *easy axis*, whereas if $D < 0$ the energy is maximum when the spin points in the Z axis, and minimum in the perpendicular plane; the Z axis is a hard axis and the XY plane is an *easy plane*.

In the classical approximation, the energy can be written

$$E_{\mathrm{A}} = -\frac{\mu_0}{2}\int \mathrm{d}^3 r\ \beta_{\mathrm{ij}}\boldsymbol{M}_{\mathrm{i}}\boldsymbol{M}_{\mathrm{j}},$$

with β_{ij} the *anisotropy tensor* of second order. However, in the uniaxial situation the only term of the anisotropy different from zero is the term along the easy axis,

chosen along the Z axis, $\beta_{zz} = \beta$. Then, the energy results

$$E_A = -\frac{\mu_0}{2}\beta \int d^3r \left(\boldsymbol{z}\cdot\boldsymbol{M}\right)^2 = K_v \int d^3r \ \sin^2\theta(\boldsymbol{r}) + \text{const.}$$

The strength of anisotropy may be expressed in terms of energy through K_v, the *anisotropy constant*, or in field units through the so-called *anisotropy field*

$$\boldsymbol{H}_K = \frac{2K_v}{\mu_0 M_s}\boldsymbol{z},$$

where M_s is the saturation magnetization. In terms of fields, the energy can be rewritten as

$$E_A = -\frac{1}{2}\mu_0 \int d^3r \ \boldsymbol{M}(\boldsymbol{r})\cdot\boldsymbol{H}_K. \tag{1.3}$$

1.2.4 Magnetostatic energy

Spins in a solid also interact through the long range dipolar magnetic fields due to the fact that they are magnetic dipoles. *Magnetostatic energy*, also called *dipolar energy* and written E_d , is the mutual Zeeman-type energy arising between all moments of a magnetic body through their stray field. The Hamiltonian of the dipolar interaction between spins at locations n and m is

$$\begin{aligned}\mathscr{H}_d &= \frac{\mu_0}{8\pi}(\hbar\gamma)^2 \sum_{n\neq m} \frac{1}{r_{nm}^5}\left[(\boldsymbol{s}_n\cdot\boldsymbol{s}_m)\boldsymbol{r}_{nm}^2 - 3(\boldsymbol{s}_n\cdot\boldsymbol{r}_{nm})(\boldsymbol{s}_m\cdot\boldsymbol{r}_{nm})\right] \\ &= -\frac{\mu_0}{8\pi}(\hbar\gamma)^2 \sum_{n\neq m} \boldsymbol{s}_{ni}\boldsymbol{s}_{mj}\frac{\partial^2}{\partial r_{nmi}\,\partial r_{nmj}}\left(\frac{1}{r_{nm}}\right),\end{aligned}$$

where $\boldsymbol{r}_{nm} = \boldsymbol{r}_n - \boldsymbol{r}_m$ is the vector containing the positions of the n and m spins.

In the classical limit, the Hamiltonian becomes the dipolar energy

$$E_d = -\frac{\mu_0}{8\pi}\int d^3r \int d^3r' \left[\boldsymbol{M}_i(\boldsymbol{r})\boldsymbol{M}_j(\boldsymbol{r}')\frac{\partial^2}{\partial r_i\,\partial r'_j}\left(\frac{1}{|\boldsymbol{r}-\boldsymbol{r}'|}\right)\right]_{|\boldsymbol{r}-\boldsymbol{r}'|^3>V_0},$$

which represent the most difficult contribution to handle in micromagnetism. Indeed, due to its non-local character it may be expressed analytically in only a very restricted number of simple situations. Its numerical evaluation is also very

costly in computation time as all moments interact with all other moments. For this reason micromagnetic simulations are usually run on the multi processor graphic card of the computer instead of the CPU, see Appendix A.

To conclude, the dipolar energy may be written as an interaction between a field, $\boldsymbol{H}_{\mathrm{d}}(\boldsymbol{r})$, and the magnetization

$$E_{\mathrm{d}} = -\frac{1}{2}\mu_0 \int \mathrm{d}^3 r \; \boldsymbol{M}(\boldsymbol{r}) \cdot \boldsymbol{H}_{\mathrm{d}}(\boldsymbol{r}), \tag{1.4}$$

which results in a Zeeman-type energy. The $\frac{1}{2}$ prefactor comes from the fact that the Zeeman interaction between two elementary moments is a mutual energy, which shall not be counted twice upon integration over the entire system.

1.2.5 Magnetic Domains

In the previous paragraphs we introduced different origins of magnetic energy, and discussed the resulting magnetic configurations. When several energies are involved, balances must be found and the physics becomes more complex. In order to minimize the total energy acting on a magnetic material, this material breaks into magnetic domains, which explain why large bodies made of a ferromagnetic material could display no net magnetic moment under zero external magnetic field.

Magnetic domains are regions in a ferromagnetic material over which all moments are aligned. In a ferromagnet of finite size, magnetization breaks into domains to reduce the magnetostatic energy generated by the dipolar field, see Fig. 1.2.

The domains reduce the magnetostatic energy by confining magnetic flux within the magnetic body. However, formation of domains requires formation of domain walls, surfaces where the orientation of the magnetization rotates abruptly (within $10-100$ nm) and this costs energy to the system. This rotation could occurs in the same plane , *Néel domain wall*, or perpendicular, *Bloch domain wall*, to the plane determined by the magnetization in both domains. Whereas the domain structure is determined by the geometry of the body, i.e., mainly exchange and

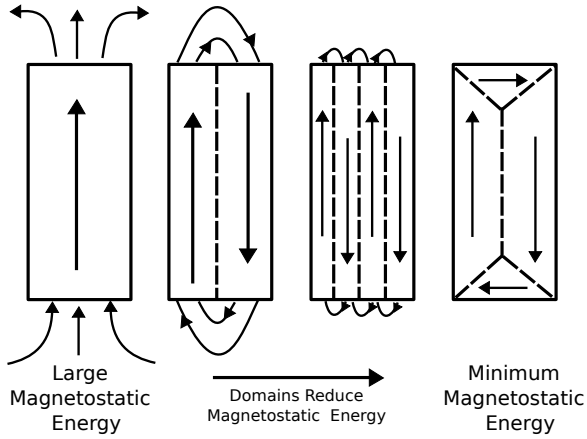

Figure 1.2 **Ferromagnetic material breaking into magnetic domains.** The single domain state (left) has high magnetostatic energy. Introduction of 180° domain walls reduces magnetostatic energy, but raises the exchange energy. Introduction of 90° closure domains minimizes the magnetostatic energy, but increase the anisotropy energy contribution.

magnetostatic energies, the type of domain wall and itsw width is determined by a competition between exchange and anisotropy energies.

1.2.6 Characteristic Quantities

Now, we study general situations where two or more magnetic energies are competing with each other, through the combination of three quantities with different units: *exchange stiffness constant* A_{ex} (J/m), *magnetization* M_{s} and *applied field* H (A/m), and an *anisotropy constant* K_{v} (J/m^3). From competing situations, characteristic quantities emerge in either energy or length scales.

- **Exchange and anisotropy**. In a situation where only magnetic exchange and anisotropy compete, the two relevant quantities in energy are A_{ex} and K_{v}. The only way to combine these quantities to express a length scale, which we expect to arise in the problem, is $\Delta_{\mathrm{u}} = \sqrt{A_{\mathrm{ex}}/K_{\mathrm{v}}}$ (m). We will call Δ_{u} the *anisotropy exchange length* [11]. This is a direct measure of the width of a domain wall where magnetization rotates (limited by exchange) between two domains whose direction is set by K_{v}. Moreover, it can be defined $E_{\mathrm{Bloch}} \approx \sqrt{A_{\mathrm{ex}}K_{\mathrm{v}}}$ (J/m^2), the energy of a Bloch wall per unit area.

- **Exchange and dipolar**. It can be shown that dipolar energy scales with the so called *dipolar constant* $K_\mathrm{d} = 1/2\mu_0 M_\mathrm{s}^2$ (J/m^3), which is a measure of the maximum density of dipolar energy that can arise in a volume. When exchange and dipolar energy compete, the two quantities at play are A_ex and K_d. This is the case in vortex core, and the resulting length scale is $\Delta_d = \sqrt{A_\mathrm{ex}/K_\mathrm{d}}$ (m), which it is called *dipolar exchange length* [12].

- **Exchange, anisotropy and dipolar**. $\mathscr{L}_{SD} = \sqrt{A_\mathrm{ex}K_\mathrm{v}}/K_\mathrm{d}$ (m) is the critical domain size of a compact nanostructure made of a quite hard material. It emerges out of the comparison of two energies, one per unit volume, the other one per unit surface. It is relevant in situations with films with perpendicular magnetocrystalline anisotropy [12].

Additional Information 1.2

Characteristic length scales are of special importance in nanomagnetism, determining the size below which specific phenomena occur. Characteristic length scales emerge from the competition between different energies, against which the size of a system can be checked to determine the magnetization distribution likely to occur.

In table 1.1 we show the magnetic parameters for the most common magnetic materials.

Material	M_s(kA/m)	$\mu_0 M_\mathrm{s}$ (T)	K_v (kJ/m^3)	A_ex (J/m)
Fe	1730	2.174	48	10^{-11}
Co	1420	1.784	530	$1.8{\cdot}10^{-11}$
Ni	490	0.616	-4.5	10^{-11}
$Fe_{20}Ni_{80}$(Permalloy)	835	1.050	~0	$1.3{\cdot}10^{-11}$

Table 1.1 **Main features of a few important magnetic materials**. Magnetization M_s, magnetocristalline anisotropy constant K_v at 300 K and the exchange constant A_ex for important magnetic materials.

1.3 Magnetization Dynamics

The final state of a ferromagnetic material, as we have seen before, is determined by the competition and the balance of magnetic energies. The summation of all the involved energies can be summarized in the total energy

$$E_{\text{total}} = E_{\text{Zeeman}} + E_{\text{ex}} + E_{\text{A}} + E_{\text{d}},$$

and allows us to talk about a total or effective field

$$\mu_0 \mathbf{H}_{\text{eff}} = -\frac{\delta E_{\text{total}}}{\delta \mathbf{M}},$$

which is the time-dependent magnetic field that the ferromagnetic material will experience.

Next, we are interested in the energy balance process, which implies a study of the time evolution of the magnetization. The initial state together with the involved magnetic energies will determine the final state of the magnetization, which can result in a static or dynamic equilibrium state. The time scale where dynamics play a role is typically at the nanosecond time scale. In this section we review the physics of spin precession and the ferromagnetic resonance.

1.3.1 Magnetization Precession Around the Effective Field

Operator dynamics in quantum mechanics implies the computation of

$$\imath\hbar\dot{\boldsymbol{S}} = \left[\boldsymbol{S}, \mathscr{H}\right],$$

where $\left[\boldsymbol{S}, \mathscr{H}\right]$ is the commutator of the total Hamiltonian of the system with the operator $\boldsymbol{S}$, the spin. In the classical approximation we obtain the so called *Landau-Lifshitz equation* (LL) [13]

$$\frac{\mathrm{d}\boldsymbol{M}(\boldsymbol{r}, t)}{\mathrm{d}t} = \gamma\mu_0 \Big[\boldsymbol{M}(\boldsymbol{r}, t) \times \boldsymbol{H}_{\text{eff}}(\boldsymbol{r}, t)\Big], \tag{1.5}$$

where the effective field is considered as a time-dependent since, as we will see further in the thesis, time-dependent interaction can be added to the system in order

to excite the magnetization. The vectorial term $\boldsymbol{M} \times \boldsymbol{H}_{\text{eff}}$ force the magnetization to rotate around the effective field, see Fig. 1.3.

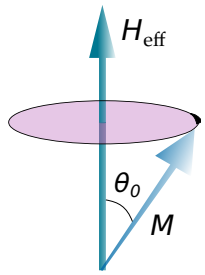

Figure 1.3 **Magnetization precession**. The magnetization precess around the effective field, $\boldsymbol{H}_{\text{eff}}$.

Solving equation 1.5 for the simplest case, where there is only Zeeman energy ($\boldsymbol{H}_{\text{Zeeman}} = H_0 \boldsymbol{z}$) and the system is uniformly magnetized, we obtain

$$\begin{pmatrix} \dot{\mu}_x \\ \dot{\mu}_y \\ \dot{\mu}_z \end{pmatrix} = -\mu_0 |\gamma| \begin{pmatrix} \mu_x \\ \mu_y \\ \mu_z \end{pmatrix} \times \begin{pmatrix} 0 \\ 0 \\ H_0 \end{pmatrix} = -\mu_0 |\gamma| \begin{pmatrix} \mu_y \\ -\mu_x \\ 0 \end{pmatrix} H_0,$$

which results in a differential equation system whose result is a precession around Z axis with a characteristic frequency $\omega_0 = \mu_0 |\gamma| H_0$, where γ is the gyromagnetic ratio. This frequency is called the *ferromagnetic frequency* and depends linearly with the external magnetic field. If a more complex energy landscape is consider the frequency expression will exhibit a dependence in those new terms. The ferromagnetic frequency for a magnetic thin film in the X-Y plane with uniaxial anisotropy along the Z direction and uniformly magnetized (there is no exchange energy dependence) is

$$\omega_0 = \gamma \sqrt{H_{\text{Zeeman}} \cdot \Big[H_{\text{Zeeman}} + \big(4\pi M_{\text{s}} - H_{\text{k}}\big) \Big]},$$

where M_{s} is the magnetization in the saturation. If the external magnetic field is applied in the $X-Y$ plane and

$$\omega_0 = \gamma \Big[H_{\text{Zeeman}} - \big(4\pi M_{\text{s}} - H_{\text{k}}\big) \Big]$$

if it is applied normal to the plane.

Landau-Lifshitz equation assumes a perpetual rotation of the magnetization around the effective field. However, this is not observed in a real systems in which magnetization is coupled with the lattice, conduction electrons, electrons on neighboring orbitals, etc. A new term in LL equation is needed to allow magnetization to be aligned along the effective field after some time, this is *damping*. Damping mechanism is very complex and stochastic and can only be taken into account analytically with a phenomenological term

$$\frac{\mathrm{d}\boldsymbol{M}(\boldsymbol{r},t)}{\mathrm{d}t} = \gamma\mu_0\Big[\boldsymbol{M}(\boldsymbol{r},t)\times\boldsymbol{H}_{\mathrm{eff}}(\boldsymbol{r},t)\Big] - \alpha\frac{\gamma\mu_0}{M_0}\boldsymbol{M}(\boldsymbol{r},t)\times\Big[\boldsymbol{M}(\boldsymbol{r},t)\times\boldsymbol{H}_{\mathrm{eff}}(\boldsymbol{r},t)\Big], \quad (1.6)$$

where $\alpha < 1$ is the *damping constant*. The new term forces to magnetization to the equilibrium position along the effective field.

The possibility to drive precession of magnetization at a specific frequency in ferromagnetic bodies was discovered by Griffiths in 1946 [14]; this is called *ferromagnetic resonance* (FMR). An oscillating external magnetic field is applied to the ferromagnetic material. By sweeping the frequency of the AC external field, ω_{ac}, we should observe a resonance, an absorption of our material, when $\omega_{\mathrm{ac}} = \omega_0$. Fitting the absorption peak we found the ferromagnetic frequency at a specific DC external field (the Zeeman field) and the linewidth of the peak contains information about the damping of the sample. Moreover, sweeping the Zeeman field we found the dependence of the ferromagnetic frequency on it, which allows us to estimate the effective field of the sample. Therefore, FMR is an important technique due to its ability to measure quantities hardly accessible otherwise, such as the gyromagnetic ratio γ, exchange stiffness A_{ex} or the damping constant α. It also yields very precise measurements of saturation magnetization and anisotropy [15].

Additional Information 1.3

- The observation of any resonance is produced by dissipation in the system, which comes from the damping term.

- $|\gamma|/2\pi$, where $\gamma = ge/2m$ ($g = 1$ for orbital magnetic moments, $g \approx 2$ for spin magnetic moments) is often expressed in frequency per Tesla. $|\gamma|/2\pi \approx 14$ GHz/T for orbital moments, and $|\gamma|/2\pi \approx 28$ GHz/T for spin moments.

Part I

Magnetization Dynamics Induced by Surface Acoustic Waves

Chapter 2

Introduction

In this part of the thesis, we expose the results of experiments and simulations on the control of magnetization dynamics through surface acoustic waves (SAWs). This part is divided into four chapters: INTRODUCTION, CONTROL OF SAWS, MAGNETIZATION DYNAMICS IN NI NANOSTRUCTURES, and PROPAGATING AND STANDING SPIN WAVES ON A NI THIN FILMS. The current chapter, INTRODUCTION, is used to define SAWs and the physics involved in the interaction of strain with magnetization, the magnetostriction effect. The chapter also provides a brief state of the art and it describes the experimental setup used in experiments, which is based in two techniques: photoemission electron microscopy (PEEM) and X-ray magnetic circular dichroism (XMCD).

2.1 Background and Definitions

2.1.1 The Magnetostriction Effect

Magnetostriction is the interaction between strain and magnetization, which leads to a change in the distance between atoms in crystal's structure when its magnetization is modified. The opposite effect, the inverse magnetostriction effect, describes how magnetization can be changed upon application of a strain. The magnetorestriction effect arises from the coupling of spin moments to the lattice via orbital electrons. Thus, a change in the lattice caused by strain modifies bonds

between magnetic atoms and changes the magnetic interactions, resulting in induced anisotropies.

Additional Information 2.1

- Some magnetostrictive materials are Iron (Fe), Nickel (Ni) or Cobalt (Co) and their alloys.
- During World War II, early sonar transducers were made of Nickel as a magnetostrictive material. To alleviate the shortage of Nickel, the Japanese navy used an iron-aluminium alloy. In 1998 it was discovered that adding gallium to iron could amplify iron's magnetostrictive effect up to tenfold. This alloy is know as *Galfenol*.

2.1.2 Surface Acoustic Waves (SAWs)

SAWs are propagating strain waves that travel at the surface of materials and they can be generated by applying a radio frequency electric signal in a piezoelectric material through metallic interdigitated transducers (IDTs) electrodes (see Fig. 2.1A for a scheme of SAW generation). The IDTs define the frequency of the SAWs trough the spacing d between the metallic fingers with the formula $f_{SAW} = n\frac{v_{SAW}}{d}$, where n is an integer, representing different harmonics, and v_{SAW} is the SAW propagation velocity (3980 m/s in $LiNbO_3$, which is the piezoelectric material we are going to use in experiments). If the frequency of the RF signal matches with the frequency f_{SAW} then SAWs are excited and launched from the IDT through the piezoelectric material up to millimeter distances.

Once the SAWs are generated, the strain wave that travels through the piezoelectric material is accompanied by the corresponding piezoelectric voltage wave. Figure 2.1B is a scheme of a traveling SAW showing the intensity of the strain modulation in the X-Z plane of a SAW propagating along X. SAWs induce regions with maxima and minima of strain, green colorscale, along X and decay exponentially with depth and the decay length of the order of the SAW wavelength [16, 17]. Blue dashed line represents the piezoelectric potential at the sample surface.

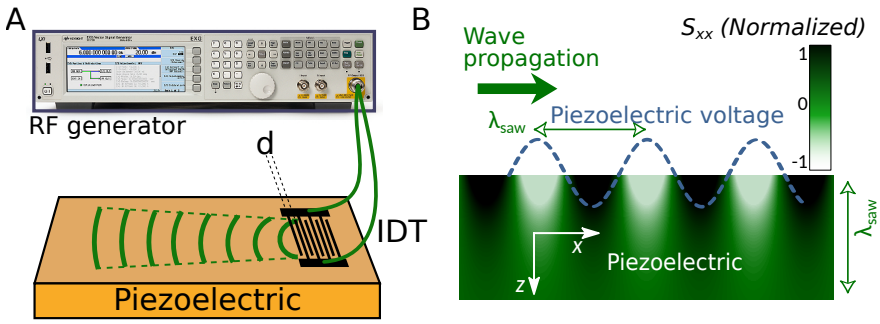

Figure 2.1 **Scheme of a strain wave**. **(A)** Scheme of the generation of the SAWs on a piezoelectric material. **(B)** Schematic plot of the in-plane strain (in green colorscale) induced modulation in the piezoelectric caused by SAWs. Dashed blue line indicates the oscillating piezoelectric voltage modulation.

The SAW frequency range achieved in our experimental setup, which depends on the piezoelectric and the efficiency of the IDTs, starts at hundred of MHz, at the 1st harmonic, until few GHz at the 11th harmonic. Figure 2.2A shows the reflection, S_{11} in dBm, of the IDTs as a function of the RF signal frequency. The lower power reflection peaks show the frequencies where the $f_{RF} = f_{SAW}$ and SAWs are excited. On the other hand, Fig. 2.2B shows the reflection of the IDTs, S_{11}, in dBm, in the time domain. In the sample there are two confronted IDTs separated by 2.8 mm and SAWs go to the opposite IDTs, which is open, and reflect back in 1.4 μs and the power of the reflected SAWs is a $10-20\%$ of the emitted SAWs. Moreover, there is more than one reflection (at least three).

2.2 State of the Art

A conventionally approach to manipulation of magnetization is the use of current flowing through a coil or stripline, which generates non-localized magnetic fields. Another approach is to exploit the spin-torque effect due to a transfer of angular momentum from a spin polarized charge current [18, 19]—technique that we study in the second part of this thesis. Techniques that are not based in the application of charge currents, which avoid heat dissipation, are of strong interest for device applications. A promising strategy for handling magnetic moment variation is the use of electric fields [20, 21], which are able to work at high frequencies with a

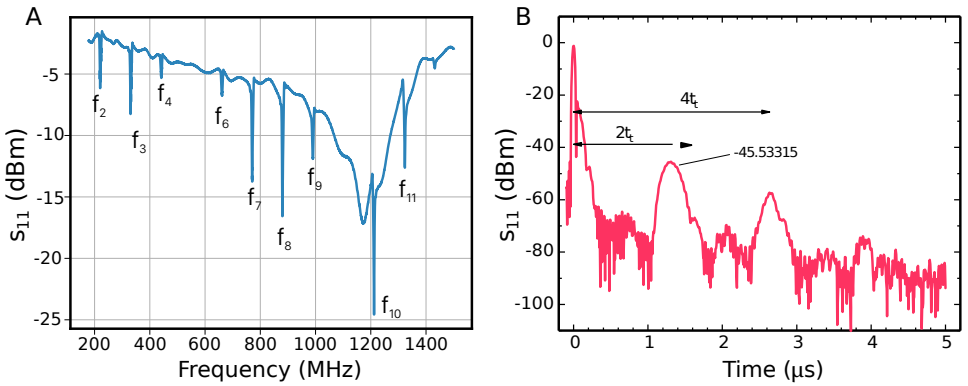

Figure 2.2 **S_{11} as a function of the frequency and time**. **(A)** Reflection of the IDT, S_{11} in dBm, as a function of the RF frequency. The frequencies with lower power reflection, marked by f_i, represent the frequencies for which the SAWs are excited and travel through the piezoelectric. Different harmonics can be excited changing the RF signal frequency. **(B)** Absorption of the IDT, S_{11} in dBm, as a function of time. The SAW takes ≈ 1.4 μs to come back to the IDT and there is signal for at least two more bounces. The measure was made at room temperature and the opposite IDT was leave it open during the measurement.

low power dissipation. The effects of electrical fields on magnetic states are weak. However, electrical fields can be used to induce strain and elastic deformations in nanoscale magnetic materials that could result in changes of the magnetic properties. Studies based on static electrical fields, indicate that the magnetization can be modified by the induced strain even for moderate applied electric fields [22–24]. Finizio et al. were able to induce static strain to a magnetic nanostructured material by the application of static electric fields [24]. However, high-speed excitations are required for technology applications.

Surface acoustic waves (SAWs) are propagating strain waves that are commonly used in electronics since they have the ability to convert a centimeter wave in free space into a micrometer wave in a chip. SAWs can be generated through oscillating electric fields at the surface of piezoelectric materials and they are used in commercial RF signal filters and delay lines, as well as in research, for example for controlling light emission from quantum wells [25].

Regarding magnetic systems, SAWs have been used to generate magnetic avalanches [26], excite spin waves [27] and tilt magnetization [28] in magnetic thin films, switch magnetization in magnetic nanostructures [29] as well as in thin films[30] and molecular magnets [31], to generate spin currents in a ferromagnetic

thin film bilayers [32], and also to excite ferromagnetic resonance modes in Nickel thin films [33]. Those examples show that SAWs represent a good approach to the control of the dynamics of the magnetization. SAWs can work in the low GHz range and meet the condition of low-power consumption required for technology applications.

Despite their frequent use and relevance, very few real-space imaging techniques are available to directly observe and quantify SAWs on their intrinsic timescale [34, 35]. In this part of the thesis new results on the imaging of SAWs on a piezoelectric material are reported. Through this imaging technique the SAW electric amplitude can be directly measured and from the electric amplitude, the associated strain can be calculated. In addition, the study of SAWs interferences is carried out confronting two SAW's sources, where we focus on the possibility of exciting standing strain waves.

The magnetization dynamics induced by SAWs, the final goal of this part of the thesis, is studied after the description of the SAWs imaging techniques. We investigate the magnetization dynamics induced by SAWs in Nickel (Ni) systems since Ni is a soft ferromagnetic material and exhibits a clear influence of strain on their magnetic states [22, 24]. On the one hand, we study Ni nanostructures showing a specific magnetic vortex state and we investigate their response to SAWs. On the other hand, we study the magnetization dynamics on Ni thin films. We excite large amplitude spin waves of different wavelengths on the ferromagnetic materials. Finally, confronting two SAW's sources we generate standing spin waves.

2.3 Experimental Setup

For the well understanding of the measurements in following chapters we consider necessary to present a brief technical description of some of the equipment used at ALBA synchrotron, where the measures were performed. The piezoelectric material used in experiments is 128° Y-cut $LiNbO_3$ and the values of density, dielectric constant, elastic, and piezoelectric coefficients are taken from Roditi International Corporation [36]. Unidirectional IDTs were patterned with photolithography and deposited with electron beam evaporation (10 nm Ti | 40 nm Al | 10 nm Ti).

The ALBA synchrotron provides X-rays pulses of about 20 ps length at a repetition rate of 500 MHz in multibunch mode, see Fig. 2.3. Synchrotron pulses allow us to achieve time-resolved measurements faster than the characteristic time response of the microscope. The energy range of the provided X-rays, in the CIRCE endstation [37], covers from 0.1 to 2.0 keV and, after an energy scan, the energy corresponding with the peak of the energy absorption of our material is chosen. At the maximum absorption energy photoelectrons emerge from the sample surface are obtained and are used to image the sample.

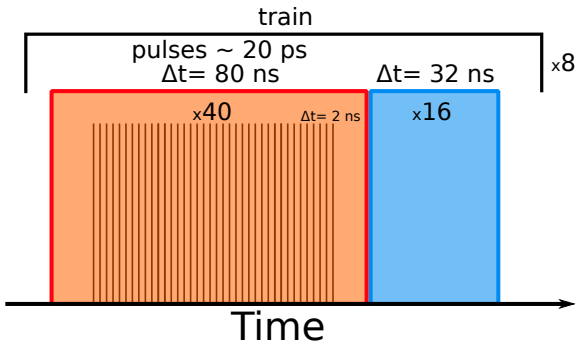

Figure 2.3 **Intensity provided by ALBA**. Schematic of the multibunch mode filling pattern (intensity versus time) of the ALBA synchrotron. The ring has 448 buckets, each of 2 ns duration (500 MHz) and are equally distributed in a filling pattern consisting of 8 trains of 40 buckets filled with electrons separated by 16 empty buckets.

Hybrid Mode Filling Patterns

The 500 MHz repetition rate presented before represents the straightforward choice to investigate SAWs in ALBA synchrotron. However, different frequencies may be desirable for applications such as studying sample-specific resonances excited by SAWs.

For this goal, hybrid mode filling patterns have become available at the ALBA synchrotron by single-bunch selective injection [38]. This hybrid mode consist in 224 buckets, which are filled in a row and after a gap, 32 single bunches are filled one every 4 buckets (125 MHz repetition rate, 8 ns spaced in time), Fig. 2.4.

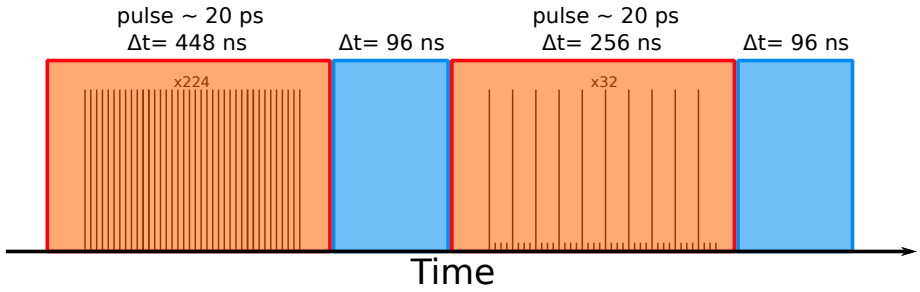

Figure 2.4 **Intensity provided by ALBA**. Schematic of the multibunch hybrid mode filling pattern (intensity versus time) of the ALBA synchrotron.

2.3.1 Microscopes

Electron microscopy (EM) is a technique for obtaining high resolution images that uses electrons instead of photons. The high resolution of EM images result from the use of electrons, which have very short wavelengths, as a source of illuminating radiation. The two most familiar types of EM are called Transmission Electron Microscopes (TEMs) and Scanning Electron Microscopes (SEMs). Both techniques require an electron emitter. Those emitted electrons pass through the sample and arrive to the microscope in the TEM technique whereas in the SEM technique the electrons arrive to the sample and are reflected to the microscope.

The measurements reported in this part of the thesis were made with a Photo Emission Electron Microscope (PEEM). PEEM technique, which is based on SEM, uses electrons that leave the sample, which are previously excited with X-rays. As a result of the X-ray absorption, electrons are excited from core levels into unoccupied states, leaving empty core states. Electrons from a higher energy level may fall into the vacancy, resulting in a release of energy. Although most often this energy is released in the form of an emitted photon, the energy can also be transferred to another electron, which is ejected from the atom creating a cascade of low-energy electrons of which some escape into vacuum and are directed towards the analyzer by applying an electric field of 20 kV between the grounded sample and the microscope. The PEEM is tuned to use low-energy electrons, also called secondary electrons, to form the image. Those electrons have a small range of kinetic energy of about ~1 eV and for finetuning to the maximum intensity a bias voltage can be adjusted in the microscope. This voltage can be tuned between

-5 to 100 V and affects to the contrast of the resultant image and represents the kinetic energy of the accepted electrons that are used to generate the image.

2.3.2 Magnetic Contrast with XMCD Technique

PEEM images can be combined with X-ray Magnetic Circular Dichroism (XMCD) to observe magnetic contrast in magnetic materials. In X-ray absorption spectroscopy (XAS) electrons are excited from a core state to a valence state. For a magnetic transition metal this can be the transition from a 2p core state into free states in the valence band, dominated by the 3d valence electrons. Because of the spin-orbit interaction, the 2p core states are energetically split into $2p_{1/2}$ and $2p_{3/2}$ levels. If light is circularly polarized, depending on the helicity of the light, the quantity of electrons that are excited into the unoccupied 3d states will be different for the different spin directions. In a ferromagnet the density of unoccupied states is different for the two spin directions (Fig. 2.5A). Therefore, the number of possible transitions depends on the alignment of the light helicity with respect to the direction of the magnetization. Figure 2.5B shows the absorption peaks in Fe

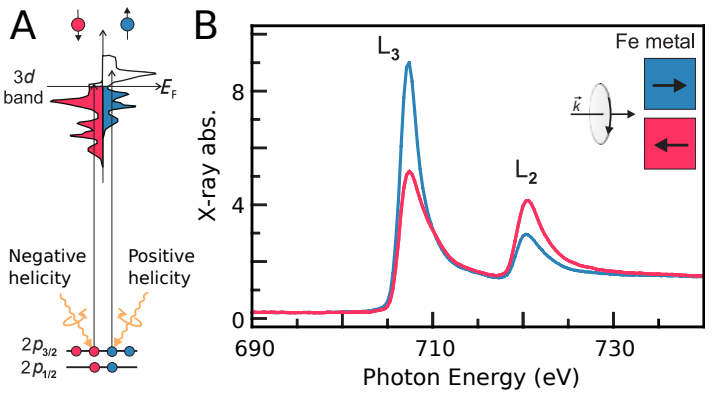

Figure 2.5 **X-rays absorption**. The XMCD effect illustrated for the L-edge absorption in Fe metal. We show the case of circularly polarized X-rays with positive angular momentum (helicity), and the color coded spectra corresponds to the shown sample magnetization directions. Figure adapted from ref. [8] (page 398).

taking the same polarization for the X-rays and changing the magnetic state (color code show the magnetic direction) of the observed region. The two peaks at each

curve are called L_3-edge, at lower energy with the greatest intensity, while the peak at higher energy has less intensity and is called the L_2-edge.

In order to observe the magnetization in a magnetic sample PEEM images are taken with different photon helicities. Thus, subtracting images just the magnetic regions are not canceled, since they are different, giving us information about the direction of the magnetization respect to the photon incident direction, the X-rays direction. Although X-rays length penetration is of the order of microns on metals, PEEM is a surface sensitive technique since the emitted electrons originate from a very superficial layer. Most of the signal is generated in the top 2-5 nanometers.

Fig. 2.6 shows a PEEM image (panel A) and an XMCD image (panel B) of the same 2×2 μm square of a ferromagnetic material. The X-rays illuminate the sample at the Nickel L_3 absorption edge energy, 861 eV, and the photoexcited electrons arrive to the PEEM. Using the positive and negative circular polarization we can access to the magnetic information of the ferromagnetic square. XMCD image shows four different magnetic states, arrows inside XMCD image, defining a close flux with a vortex at the central point. This ground state arises from the competition of magnetic energies described in Section 1.2 and it is known as the *Landau flux closure state*. White and black regions represent magnetization parallel and antiparallel to X-rays direction, whereas the gray regions have magnetization perpendicular to X-rays direction.

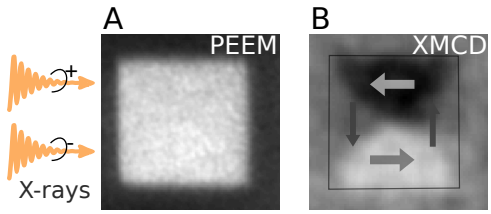

Figure 2.6 **PEEM and XMCD images**. PEEM (**A**) and XMCD (**B**) images of the same 2×2 μm ferromagnetic square. X-rays illuminate the sample with photons in both polarizations and both images combined gives us the XMCD image. White and black regions represent magnetization parallel and antiparallel to the X-rays direction whereas gray regions represent magnetization perpendicular to the X-rays direction (the arrows indicate the magnetic state). This magnetic state is know as the Landau flux closure state.

2.3.3 Synchronizing Electrical Excitation with X-rays Beam

The synchrotron X-rays radiation combined with PEEM microscopy becomes in a powerful non-invasive tool for micro- and nano-magnetism, nanoscience and technology, and surface science investigation [39]. The resulting technique is time and space resolved and can be used to study magnetization dynamics—the aim of this thesis. In CIRCE beamline, at ALBA synchrotron, the sample can be excited with external magnetic fields and with an external electric oscillatory signal [40]. Sample holders with integrated electromagnets for uniaxial magnetic fields can be used and the maximum applicable field is below 100 mT.

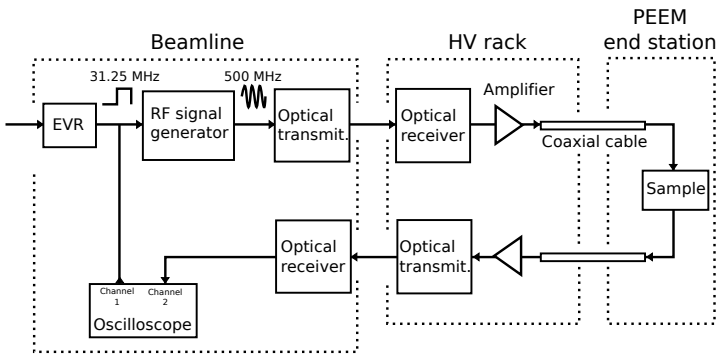

Figure 2.7 **Electrical excitation synchronized with X-rays beam**. Diagram of the setup used for synchronous 500 MHz excitation of the sample, in configuration to monitor the signal under measurement conditions. Figure adapted from Fig. 7B , Foerster et al. [40]

The external oscillatory signal can be excited at a specific phase with respect to the stroboscopic synchrotron light pulses. A vector signal generator is synchronized with the ALBA master clock signal through the so called event receiver (EVR) [41]. The electric signal is converted to optical and passed by optical fiber into the high voltage rack by an in-house module, thus providing complete galvanic separation. Figure 2.7 shows a scheme of how a sample can be excited with an oscillatory signal. After the optical separation, the signal is amplified by a commercial RF amplifier connected by a coaxial cable to the sample. The two-channel optical communication system is designed for use in an input/return configuration to

measure the transmission through the sample. Moreover, it can be adapted to provide 2 RF inputs into the high voltage rack.

2.3.4 Electron Gating

The utilization of an electron gating is an alternative procedure in order to access to different frequencies that does not requires modifications of the filling pattern mode. The electron gating is coupled to the microscope and allows us to select an specific repetition rate, which should be submultiple of the fundamental synchrotron frequency.

Chapter 3

Control of Surface Acoustic Waves

This chapter is dedicated to the imaging of SAWs in a single crystal of a $LiNbO_3$ piezoelectric. Experiments to directly detect, control and quantify the SAWs are described and discussed. First, we show that the piezoelectric wave associated to SAWs can be detected in PEEM images. The direct observation of the voltage waves leads to the quantification of the strain that is applied to the piezoelectric material. We obtain a time- and space-resolved quantification of the strain on the top of the piezoelectric material. Additionally, with a second SAW's source, we investigate interference patterns. Standing and propagating components of the resulting SAWs are quantified from a PEEM image analysis and the role of different parameters of the RF excitations for the tuning of high-standing-component SAWs is investigated.

3.1 Observation and Quantification of SAWs

Our setup at ALBA synchrotron, Fig. 3.1, allows us to excite SAWs in a $LiNbO_3$ single crystal, which are phase synchronized with the X-ray light pulses illuminating the sample (see Section 2.3.3). The piezoelectric contains IDTs for the excitation of SAWs, which were designed to launch SAWs of a frequency $f_{SAW} = 499.654$ MHz at room temperature, which is exactly the repetition rate of X-ray bunches in multibunch mode, see Section 2.3. The differential potential between the sample and the PEEM was set at 10 kV instead of 20 kV as usually set in PEEM imaging

technique to avoid electric arches. This has an impact on the resolution of the PEEM.

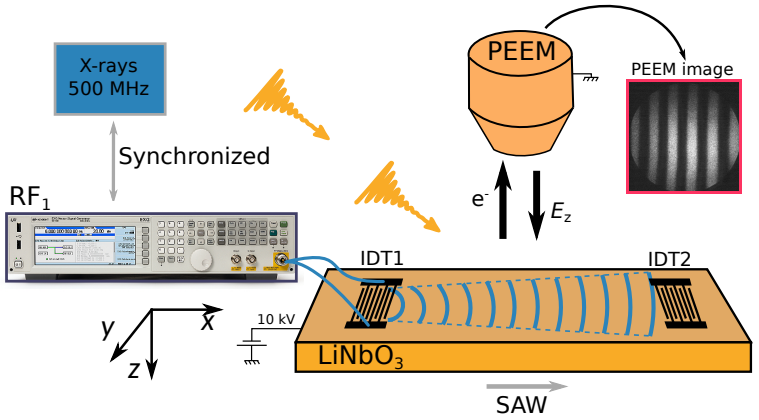

Figure 3.1 **Schematic plot of the set-up at the ALBA synchrotron**. Circularly polarized X-rays illuminate the sample in the form of 20 ps pulses with a repetition rate of $f_0 \approx 500$ MHz. The IDT_1 receives an AC electric signal of the same frequency, which is phase locked to the synchrotron repetition rate, generating a piezoelectric SAW that propagates through the $LiNbO_3$ substrate.

The piezoelectric voltage wave can be directly observed in a PEEM image when SAWs are turned on. The dark and bright regions, which represent the minimum and the maximum of the wave, present a periodicity that matches with the SAW wave length, $\lambda_{SAW} = 8\ \mu$m. Figure 3.2 shows a phase sequence of PEEM images where the piezoelectric voltage wave can be directly observed[1]. Green lines represent the wave front traveling whereas red and yellow boxes show the bright and dark regions respectively.

The piezoelectric is illuminated with X-rays and the emitted low-energy photoelectrons arrive to the PEEM microscope. SAWs generate a voltage wave on the top of the sample, which affect the electrons that leave the sample towards the microscope. The energy of those electrons is different whether they come from a maxima or a minima of strain. The resulting image has dark color for electrons with less energy, $E_e = 10$ kV $-\epsilon$, and bright color, for electrons with more

[1] PEEM images were taken with a detune of 0.1 Hz between the SAW and the X-rays. Detuning was applied in order to observe SAW displacement. Here, we refer them as a phase sequence.

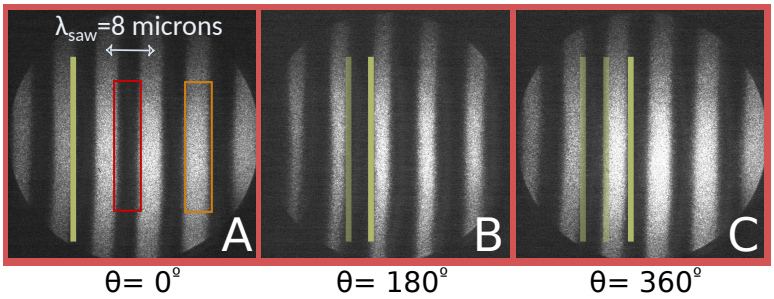

Figure 3.2 **Observing SAWs**. PEEM images with a field of view of 50 μm of the piezoelectric substrate when the SAWs are excited at -16 dBm for different relative phases. The parallel dark and bright regions correspond to the piezoelectric wave with the same periodicity of the SAW, $\lambda_{\mathrm{SAW}} = 8$ μm. The wave front, green line, is displaced to the right at different phases.

energy, $E_{\mathrm{e}} = 10$ kV $+\epsilon$, where ϵ is the amplitude of the piezoelectric voltage wave. Therefore, PEEM images provide a local measurement of strain strength.

The calculation of ϵ becomes the first step for the quantification of the strain applied to the piezoelectric. Thus, we study the intensity of photoelectrons in both dark and bright regions, rectangles in Fig. 3.2A , corresponding to opposite phases of the wave. Figure 3.3 shows the number of photoelectrons as a function of the bias voltage at those opposite areas (the color of the curves corresponds to the color of the rectangles in Fig. 3.2) when the SAWs were excited at a nominal -16 dBm in the RF signal generator.

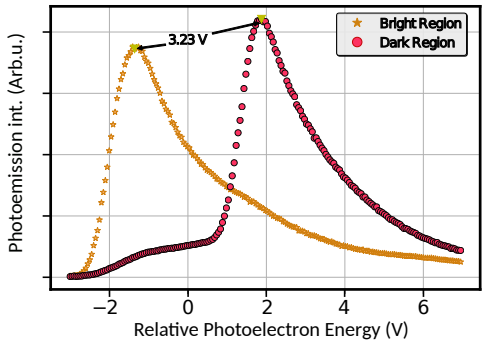

Figure 3.3 **Photoemission intensity**. Two photoelectron energy scans of the photoemission intensity corresponding to a bright and a dark zone (indicated in Fig. 3.2A with red and orange boxes). The difference between peaks is the peak-to-peak amplitude of the SAW-induce piezoelectric potential.

Peaks correspond to the energy where more photoelectrons are detected. Those peaks are different whether the measurement corresponds to a dark region, yellow line and lower energy, or bright region, red line and more energetic electrons. The energy between the two curve's peak, 3.2 V, corresponds to the peak-to-peak amplitude of the SAW-induced piezoelectric potential,ϵ, added to the 10 kV applied at the sample surface for PEEM detection.

Repeating this measurement for different nominal power of the SAWs results in a lineal relation for low values of the RF power and the peak-to-peak voltage. Figure 3.4 indicates that the amplitude of the voltage wave saturates for higher RF power of the SAWs.

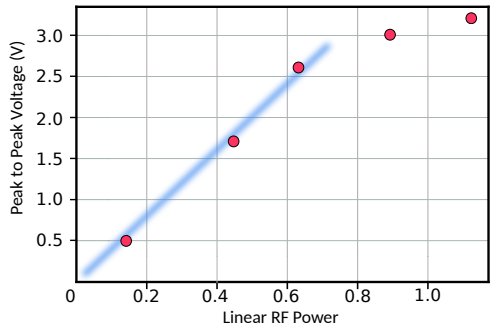

Figure 3.4 **Piezoelectric potential**. Relation of the nominal RF power with the peak-to-peak amplitude of the SAW-induce piezoelectric potential.

The measurement of the amplitude of the surface electric potential associated with the SAW allows us to obtain a quantification of the strain induced by SAWs [3]. We plot in Fig. 3.5 the oscillation along x of the piezoelectric potential with a peak-to-peak amplitude of 3.2 V (blue dashed curve), together with its corresponding longitudinal in-plane strain component, S_{xx} (solid curve). We notice that the piezoelectric potential, and therefore the out-of-plane electric field, $E_z = -\partial_z \phi_{\mathrm{SAW}}$, is in phase with S_{xx}.

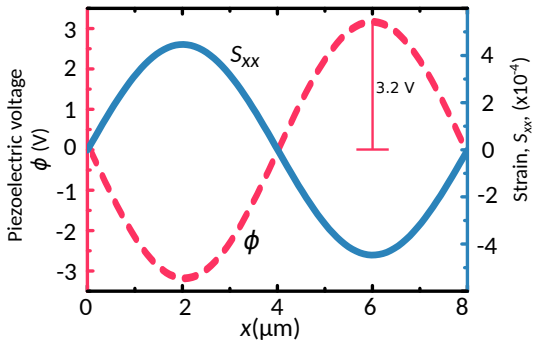

Figure 3.5 **Strain wave**. Calculation of the in-plane strain component (right-hand-side axis) and the piezoelectric voltage (left-hand-side axis) at the sample surface for a SAW with a $\lambda_{SAW} = 8\ \mu$m.

3.2 Propagating and Standing SAWs

We are interested in the interferences that may cause on the piezoelectric material the superposition of two different SAW's sources. A particular case of wave interference is the excitation of a standing wave, where the resultant wave does no propagate and present nodes and antinodes. Standing SAWs (SSAWs) are interesting because they may allow us to stabilize spatial patterns over any desired period of time. SSAWs can be generated by exciting two opposite IDTs [42] or by using the reflections created in opposed IDTs in resonant structures [43]. In real experiments one may have to deal with general superposition of standing and propagating waves. In fact, in the most simple picture where there is just one IDT connected there is at least the reflection of the propagating SAW (see Fig. 2.2B) at the end of the piezoelectric substrate.

In this section SSAWs are studied and quantified on a piezoelectric material with PEEM imaging technique. Figure. 3.6 shows a scheme of the experimental setup needed for their excitation. The signal generators (RF_1 and RF_2), now we have two and they are synchronized, are phase locked to the synchrotron repetition rate. Both RFs excite SAWs in opposite directions. Panels A and B of Fig. 3.6 are sequences of PEEM images (with a field of view (FOV) of $\approx 50\ \mu$m) at the same region when there is one or two SAWs sources turned on and different images were taken by changing the relative phase of the SAWs. In Fig. 3.6A the RF_1 is turned on at -27 dBm and the RF2 is off and the phase sequence shows that SAWs move

continuously from left to right whereas in Fig. 3.6B both IDTs are turned on at $RF_{1,2} = -27$ dBm and there is no continuous displacement. Both panels shows a $\lambda_{SAW} = 8\ \mu$m periodicity.

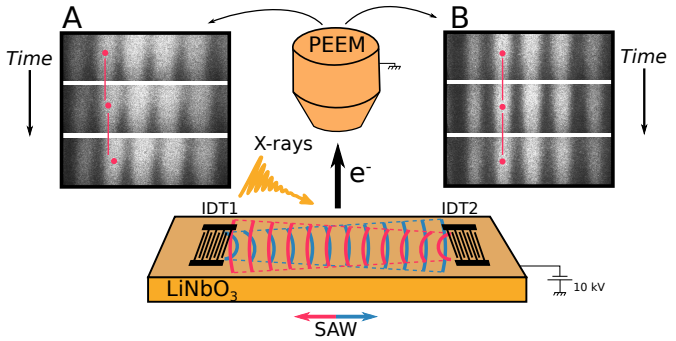

Figure 3.6 **Experimental setup**. IDTs receives an AC electric signal of the same frequency from *different* signal generators, which are phase locked to the synchrotron repetition rate. SAWs are generated in the piezoelectric and propagates from each IDT, through the $LiNbO_3$ substrate, to the other (red and green lines). Panels (**A**) and (**B**) are both vertical phase sequences of three PEEM images of the SAW. Panel **(A)** shows a propagating situation whereas the panel **(B)** shows the standing case where the peaks do not change their position when the relative phase changes.

We model the interference of two confronting SAWs as $A(x,t)_{\text{both}} = \epsilon\cos(\omega_0 t - kx) + (1-\epsilon)\cos(\omega_0 t + kx)$, where $\epsilon = V_1/(V_1+V_2) \in [0,1]$ with V_1 and V_2 the voltage of the waves from IDT1 and IDT2 respectively. We define $r_{\text{prop}} = 2\epsilon - 1 \in [-1,1]$ as the *ratio of propagating wave*. If $r_{\text{prop}} = 0$ ($\epsilon = 1/2$), the wave is totally standing whereas if $r_{\text{prop}} = -1, 1$ ($\epsilon = 0, 1$), the wave is totally propagating. Then, we can rewrite the previous expression as

$$A(x,t)_{\text{both}} = \cos(kx)\cos(\omega_0 t) + r_{\text{prop}}\sin(kx)\sin(\omega_0 t).$$

The amplitude, A_{ft}, and the phase, Φ_{ft}, of the resultant wave $A(x,t)_{\text{both}}$ give us two ways to calculate the r_{prop}

$$|r_{\text{prop}}| = \min[A_{\text{ft}}]/\max[A_{\text{ft}}], \tag{3.1}$$

$$|r_{\text{prop}}| = \sqrt{\min[\Phi'_{\text{ft}}]/\max[\Phi'_{\text{ft}}]}, \tag{3.2}$$

where Φ'_{ft} is the spatial derivative of the phase. From those expressions we can compute the ratio of propagating and standing wave from experimental data. We take PEEM images varying the phase continuously for many periods of the resulting wave ($\approx$ 1500 images) when both signal generators are turned on.

For the analysis of the PEEM images, we focus on each point in the image and we study how they evolve as a function of the relative phase. We perform the fast Fourier transform (FFT) of the variation of each point of the PEEM image sequence and calculate the amplitude and the phase of the resulting oscillation. In the simplest case, where SAWs propagate on the piezoelectric crystal, all the

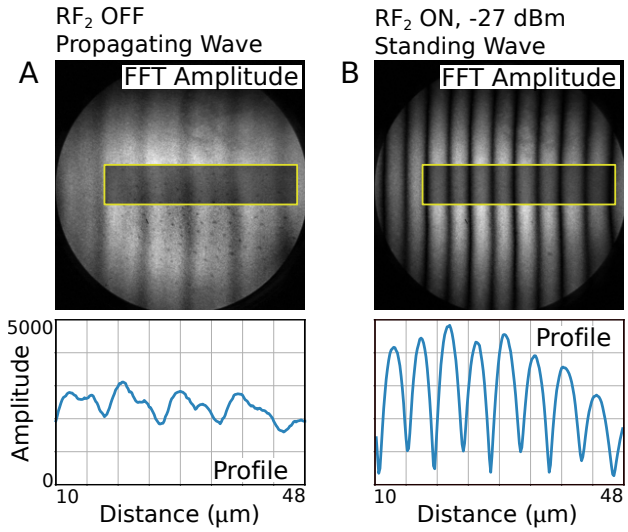

Figure 3.7 **FFT amplitude and profiles**. Amplitude of the oscillation of each point of the PEEM image for the case of propagating **(A)** and standing waves (**B**). The bottom panels shows the profile of the amplitudes inside the rectangle (averaged along the vertical y direction to get the dependence on the horizontal coordinate, x). For the case of propagating wave the RF_1 was fixed -27 dBm and for the case of standing wave both RF_1 and RF_2 were at the same power (-27 dBm).

points in the image should exhibit the same oscillation amplitude and the phase between two different point separated in the propagation direction should change continuously. On the other hand, if the resulting wave is a SSAW, there will be points that do not oscillate and the points that oscillate, they present different

amplitudes. Moreover, between two different nodes all points should oscillate with the same relative phase and it should vary in discrete steps between nodes.

Warning 3.1

In Fig. 3.7 the images are not PEEM images. Those images represent the amplitude of each point calculated using the FFT of a stack of PEEM images with different phases.

Figure 3.7 shows the FFT amplitude of the oscillation of each point of a PEEM image sequence in a grey scale, where black means zero amplitude. The left panel shows the amplitude of a propagating wave whereas the right panel shows the amplitude of the points in a standing wave situation, both RFs connected at the same power. At the bottom panels there are the profiles of the average of the square shaded regions of top panels. For the case of PSAW, the amplitude

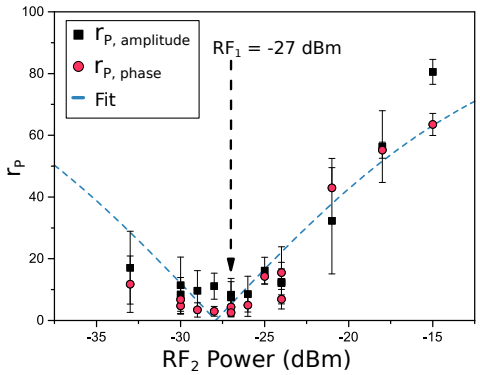

Figure 3.8 **Ratio of Propagating Wave**. The ratio of propagating wave as a function of the power on the RF_2 while the RF_1 was fixed at -27 dBm. Black squares represent the ratio calculated from the data obtained from the FFT amplitude, from formula 3.1, whereas the red dots is the same ration calculated from the FFT phase information, from formula 3.2. The minimum ratio of propagating wave is obtained when both RF_1 and RF_2 are present similar power (-27 dBm for RF_1 and -28 dBm for RF_2). The fit, blue dash line, is obtained from the relation between r_{prop} and the power in dBm.

presents a small variation from maxima and minima points whereas for the SSAW there is a big difference between maxima and minima, which are close to zero. However, profiles indicate that both PSAW and SSAW are not pure since we expect

the same amplitude for all points in the PSAW and the nodes in the SSAW should not oscillate and have a zero amplitude, however, we also have to take into account that the experimental noise is always greater than zero, see Fig. 3.7.

In order to estimate the quality of the PSAW (or the SSAW) we compute the value of r_{prop} using formula 3.1. Figure 3.8 shows the value (in %) of the the r_{prop} calculated from the FFT amplitude (black squares) and the r_{prop} calculated from the FFT phase (red dots) for the case where RF_1 was fixed at -27 dBm and the power of RF_2 runs from -33 to -15 dBm. The fit of the data (blue line) is obtained from the theoretical relation between r_{prop} and the power in dBm. The minimum value of the ratio of propagating wave is obtained from the fit when the power of both RF generators are similar: -27 dBm for RF_1 and -28 dBm for RF_2. The resulting wave presents less that 5% of propagating wave, which means that is almost a standing.

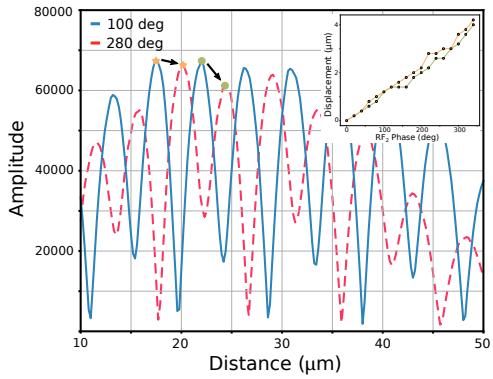

Figure 3.9 **Standing wave displacement with the phase**. Profiles calculated from the FFT amplitude for the case when both RF_1 and RF_2 were at the same power (-27 dBm). The blue line shows the profile when the phase of RF_2 is 100 deg and the red dashed line for 280 deg. The markers (green and yellow) show the displacement of the peaks for the case of 180 deg and the inset plot shows the displacement of those peaks from 0 to 360 deg.

Finally, we study the role of the relative phase between the two SAW sources. Figure 3.9 shows two profiles of the amplitude of the FFT images for the case of 100 deg (blue line) and 280 deg (red dashed line) between the RFs. In both cases the r_{prop} is below 10% and the quality of the SSAW does not present a strong dependence on the relative phase. However, a change in the relative phase moves

the position of the maxima and minima in the profile. The markers (green stars and yellow dots) show the displacement of two different peaks along 180 deg. The inset of Fig. 3.9 shows how those peaks move when the phase changes from 0 deg to 340 deg. Both peaks present the same displacement close to 3.5 μm in the image (the images are 50×50 μm).

3.3 Conclusions

PEEM images gave us information about the electron energy distribution emitted from the surface of the sample. Those electrons carry information about the piezoelectric voltage wave, which was directly observed, both propagating and standing SAW. The amplitude of the piezoelectric voltage wave was measured from the electron intensity at different areas in PEEM images and then, we estimated the total strain applied to the piezoelectric crystal. We obtained a time- and space-resolved calculation of the strain induced at the surface of the piezoelectric by the SAWs. Finally, we have shown a procedure, based in PEEM imaging, to distinguish and analyze quantitatively a mixture of standing and propagating SAWs. The method allowed us to quantify the proportion of SSAW and PSAW of any interference of SAWs produced by one or more SAW's sources. We conclude that it is complicated to obtain experimentally a pure standing or a pure propagating SAW.

Chapter 4

Magnetization Dynamics in Ni Nanostructures

In this chapter we study the magnetization dynamics induced by SAWs on Nickel (Ni) square nanostructures. We provide direct and a simultaneous observation of both strain waves and magnetization modes with high spatial and temporal resolution. PEEM images give us information of the strain waves and XMCD images allow us to access the magnetization modes. We find a delay between the strain wave and the magnetic response of the Ni squares and we use micromagnetic simulations to identify the magnetic resonances in our sample.

4.1 The Effect of SAWs on Ni Nanostructures

About 20 nm thick Ni nanostructures were defined with electron beam lithography and deposited by means of e-beam evaporation onto the piezoelectric substrate and in the acoustic path between the two IDTs. Figure 4.1A shows a PEEM image with many different Ni nanostructures with different sizes and forms such as ellipses or squares. Moreover, on the image the piezoelectric voltage wave is also visible.

The Ni sample was characterized with SQUID magnetometry to determine the saturation magnetization and with FMR spectroscopy to determine the damping parameter and the growth-induced in-plane uniaxial anisotropy. The in-plane

uniaxial anisotropy compete with other internals magnetic energies such as the exchange energy and the magnetostatic energy, which depends on the shape of the Ni nanostructure, in order to establish the ground magnetic state, see Section 1.2. Figure 4.1B shows the corresponding XMCD image where ground magnetic states of all the nanostructures are visible. We focus on square Ni nanostructures with size of 2×2 μm^2 because they present a magnetic state with a central vortex known as Landau flux closure state. Figure 4.1C shows a zoom of two of the Ni nanostrucutures, red boxes in panels A and B, that present this specific magnetic state.

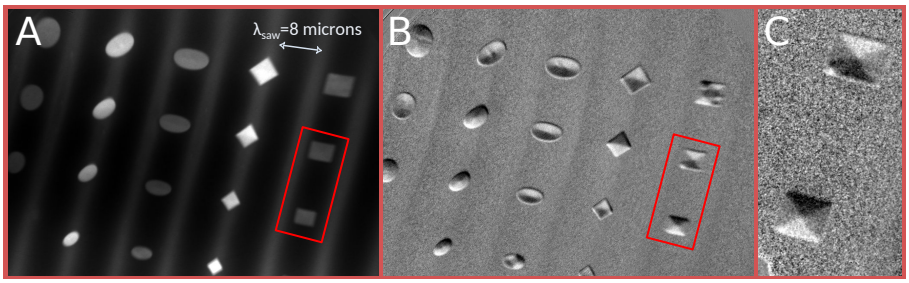

Figure 4.1 **PEEM and XMCD images of the Ni nanostructures**. **(A)** PEEM and **(B)** XMCD images of a Ni nanostructures with different forms and sizes. **(C)** Zoom of two Ni squares that present a magnetic state with a central vortex known as Landau flux closure state.

Finizio et al. in 2014 were able to manipulate magnetic domains in Ni 2×2 μm^2 squares that present a Landau flux closure state through the application of static strain [24]. Combining PEEM, XMCD, and SAWs we study 2×2 μm^2 Ni squares that are aligned with the SAW propagation direction (X direction) presenting a magnetic state similar to Fig. 4.1C. We focus on the response of the magnetic states of the Ni squares to the application of dynamic strain induced by SAWs.

Multiple Ni squares that meet the condition described above were selected. We consider the center of the square as 0 deg respect to piezoelectric wave and the relative phase of the SAW is changed electronically. Figure 4.2A and B show the PEEM and XMCD images, respectively, for the same Ni square. In Fig. 4.2A it is easy to distinguish the piezoelectric wave, dark and bright regions, whereas in Fig. 4.2B we observe how the magnetic state changes when the phase of the SAW is

changed. White and black regions represent the parallel and antiparallel magnetic regions with respect to the X-ray, arrows in first image of panel B , and the grey regions represent the intermediate states.

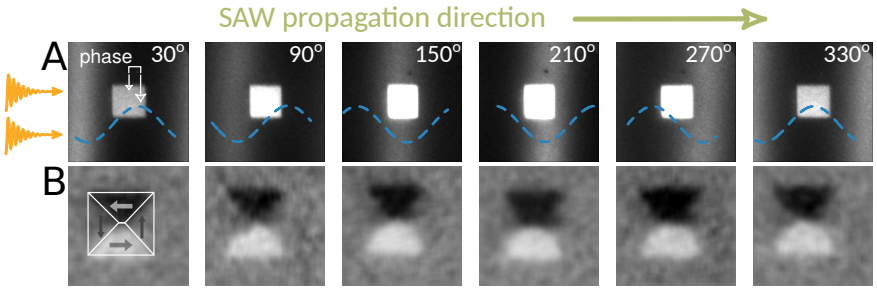

Figure 4.2 **Simultaneous images of SAW and magnetic domains**. **(A)** PEEM and **(B)** XMCD images of a 2×2 μm^2 Ni square at different phases of the SAW. Images correspond to phase lapses of 60° (that correspond to 333 ps). PEEM images are 8×8 μm^2; XMCD images are 4×4 μm^2. X-ray, represented by the yellow lines, form an angle of 90 deg with the Ni square edge.

The magnetic state of a Ni structure changes when the relative phase of SAW is changed. Depending on whether the maximum of the strain wave is on one side or the other side of the square, the white and black regions are smaller, phase of 90 deg, or bigger, phase of 270 deg. The strain, through the inverse magnetorestriction effect, see Section 2.1.1, modifies the in-plane anisotropy of the Ni and parallel regions are enhanced or reduced depending on the strain. A schematic plot of the effect of a strain wave on the Ni square is shown at Fig. 4.3A.

The total area of white and black domains (magnetization along the X-rays direction) at each phase of the SAW was calculated and Fig. 4.3B shows the black and white fraction of the total area. Small white squares are the data and the red curve is the best sinusoidal fit. The response to SAWs of domain configurations were analyzed from multiple squares within the same piezoelectric substrate by acquiring 20×20μm^2 size XMCD images at different phase delays between SAW and X-ray pulses. Moreover, in the background, we plot in green the strain wave with no Y-scale.

We observe a considerable delay between the magnetization oscillation and the strain wave that amounts to ≈ 270 ps (phase delay of ≈ 48 deg). The delay can not be attributed to a delay on the sound propagation from the $LiNbO_3$ to the Ni

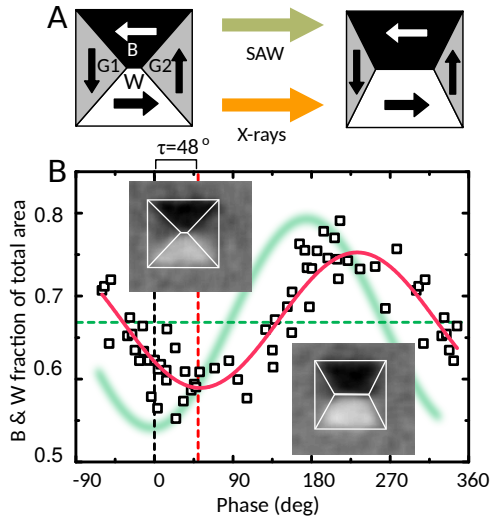

Figure 4.3 **Quantification of the magnetic domain configuration**. **(A)** Schematic plots of the effect of SAW on Ni squares. **(B)** Analysis of the domain configuration from multiple (4) Ni squares of 2×2 μm^2 as a function of the individual phase with respect to the SAW for the configuration shown in **(A)**. We computed the area of black and white domains (amount of magnetization along the X-ray incidence direction) and red curve is a sinusoidal fit for the data. A schematic strain wave is plotted in green (with no scale) to indicate the phase values corresponding to maximum and minimum strain corresponding to a response without delay.

squares. In 2005, Raabe et al. observed three different excitations on permalloy ($N_{81}Fe_{19}$) squares with Landau flux closure state of various orientations with 6 μm length and 30 nm thickness. They performed temporal and spatial resolved measurements that allowed them to quantitative analyze the excitations. They observed precessional motion of the magnetization within the domains as well as a domain wall mode and vortex motion [44]. We attribute the delay to a coupling between the SAWs and internal magnetic resonances of the system. In order to study them we use micromagnetic simulations.

4.2 Micromagnetic Simulations: Magnetic Resonances

Simulations were performed using MuMax^3 [45], see the technical description of the micromagnetic software in Appendix A. We consider a two-dimensional layer of Ni (2×2 μm^2) with parameters taken from sample characterization: satu-

ration magnetization $M_s = 490 \times 10^3$ A m^{-1}, Gilbert damping constant $\alpha = 0.03$, and exchange constant $A_{ex} = 5 \times 10^{-12}$ Jm^{-1}. The SAWs were simulated as an anisotropy wave propagating along the X direction. We introduce a fixed uniaxial anisotropy $k_{\mathrm{U}} = 1200$ J m^{-3}, also taken from characterization, and an additional oscillating term of $k_{\mathrm{ME,ac}}$ having the wavelength set by the SAW ($\lambda_{\mathrm{SAW}} \approx 8\ \mu$m). The value of the oscillating term was adjusted comparing the experimental variations in the magnetic-domain configuration observed in the XMCD images with the simulations, Fig. 4.4A. The oscillation of the domain areas is well reproduced by a strain-induced modulation of the magnetic anisotropy of amplitude $k_{\mathrm{ME,ac}} \approx 1$ kJm^{-3} superimposed to a preexisting uniaxial anisotropy, ~ 1.2 kJm^{-3}, caused by the deposition process.

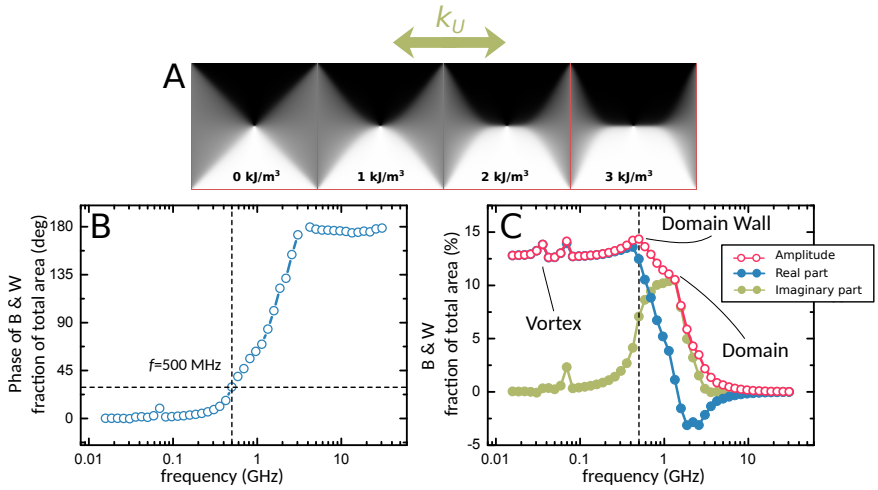

Figure 4.4 **Simulations of Ni squares excited with SAWs**. **(A)** Magnetic domain configurations corresponding to different uniaxial anisotropies. Magnetic-domain configuration on a Ni square $2 \times 2\ \mu$m^2 with 20 nanometer in thickness, considering that the anisotropy axis is along the square sides. **(B)** phase and **(C)** amplitude, in phase (real part), and out of phase (imaginary part) parts of the magnetic response of the system to an oscillating anisotropy as a function of the frequency. We plot the same quantities we analyzed for the experiment, Fig 4.3B fraction area of black and white domains. Dashed lines (black) in panel **(B)** mark the frequency of $f = 500$ MHz, which corresponds to the frequency used in the experiments.

The experimental setup just accepts a SAWs frequency of 500 MHz. However, with simulations we cover frequencies from tens of MHz to tens of GHz in order

to find all the possible magnetic resonances. Figure 4.4B and C show the phase and the amplitude, in phase (real part), and out of phase (imaginary part) of the magnetic response of the simulated Ni square as a function of the frequency of the SAWs. The magnetic response was calculated as the fraction area of black and white domains. In Fig. 4.4B dashed lines correspond to the experimental frequency and present a phase of 30 deg (the experiment results shows a phase of 48 deg). However, at Fig. 4.4C we can identified three different magnetic resonance processes, which correspond to precessional motion within the magnetic domain at ~ 2 GHz, domain-wall resonance at ~ 500 MHz (see Fig. 4.5B), and vortex motion at ~ 50 MHz (see Fig. 4.5A).

The found magnetic resonances are in agreement with Raabe et al. observations [44]. Therefore, we conclude that because of our experimental setup the magnetic response of the Ni is coupled with the domain-wall resonance and the response is affected by the corresponding delay. The domain-wall resonances in the studied Ni squares can not be removed because is related with the SAW direction. The SAWs produce that the black and white regions becomes bigger or smaller by changing the anisotropy parallel or perpendicular to the magnetization. Thus, we need to try a new approach in order to avoid the coupling between the excitation and the magnetic resonances of the Ni squares.

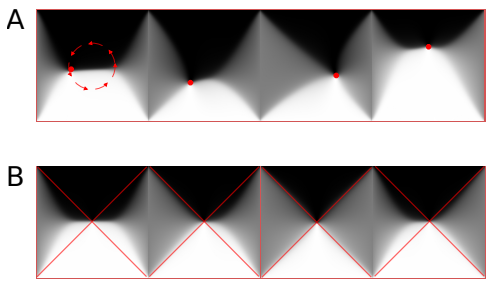

Figure 4.5 **Micromagnetic simulations of the magnetic resonances**. **(A)** Resonance of the vortex for an excitation of 50 MHz. Red dot represent the position of the vortex in the Landau state. The vortex moves around the equilibrium position. **(B)** Resonance of the domain-walls for an excitation of 500 MHz. The red lines represent the equilibrium position, when the $K_u = 0$, of the domain walls and the intersection match with the vortex, which is always at the same position.

4.3 New Configuration for Ni Structures

In simulations we can change the angle between the SAWs and the magnetic regions, which experimentally means changing the angle between the SAWs and the sample orientation. We expect that those regions are not increased or reduced but tilted, see Fig 4.6A. Simulations of the new configuration show that we can expect a smaller dephase between strain wave and their corresponding effect on magnetic states.

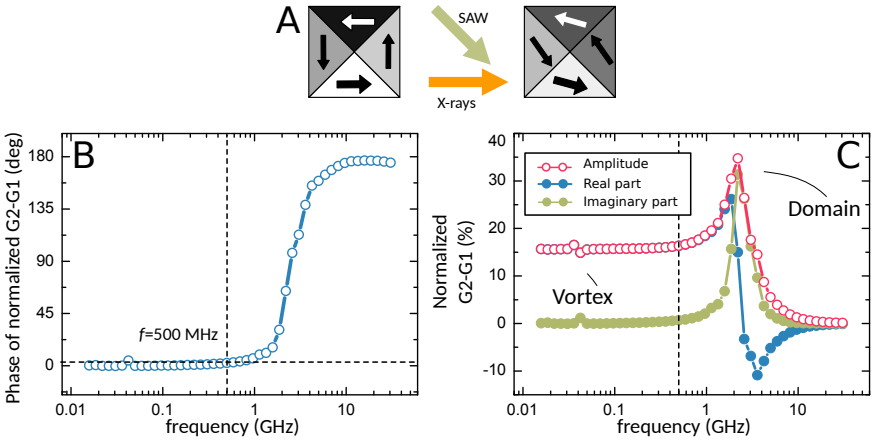

Figure 4.6 **Simulations of Ni squares perturbed by tilted SAWs**. **(A)** Schematic plots of the effect of SAW on Ni squares for configurations where SAWs were forming a 45 deg with the squares' sides. **(B)** Phase and **(C)** amplitude, in phase (real part), and out of phase (imaginary part) parts of the magnetic response of the system to an oscillating anisotropy as a function of the frequency when the varying anisotropy axis is along the square diagonals. We plotted the variation of the normalized difference between gray intensities between the two gray domains. Dashed lines (black) in the lower panels mark the frequency of f = 500 MHz, which corresponds to the frequency used in the experiments. For this configuration the phase at f = 500 MHz is smaller than 3 deg.

Figure 4.6B, obtained from simulations, shows phase and amplitude (real and imaginary part) of the magnetic response of the system when the angle between the SAWs and the sample orientation is 45 deg. The magnetization in this new configuration presents a small dephase, smaller than 3 deg (Fig. 4.6B), and in Fig. 4.6C it can be identify just two, instead of three, of the magnetic resonances: the vortex resonance at ~ 50 MHz and the magnetic domain resonance at ~ 2 GHz.

The domain-wall resonance was canceled on purpose by the new of the Ni squares respect to the SAWs.

For the experiments, the Ni squares were 45 deg tilted and we performed the same measurements done for Fig. 4.2. Figure 4.7A shows a PEEM image of many Ni squares tilted with respect to the SAWs, which are visible (dark and bright regions). In Fig. 4.7B and Fig. 4.7C we show two PEEM and XMCD images of the Ni structure inside the red box in Fig. 4.7A at different relative phases. The SAWs are directly observed in PEEM images on the top-left and bottom-right regions. Figure 4.7C shows that the excitation do not work in the same way as in Fig. 4.2 since the regions do not grow or shrink and there is not domain-wall displacement. The new configuration promotes that the white and black regions becomes more grey and the grey regions become more white and black (see Fig. 4.6A for a schematic idea of the variation of the magnetic regions).

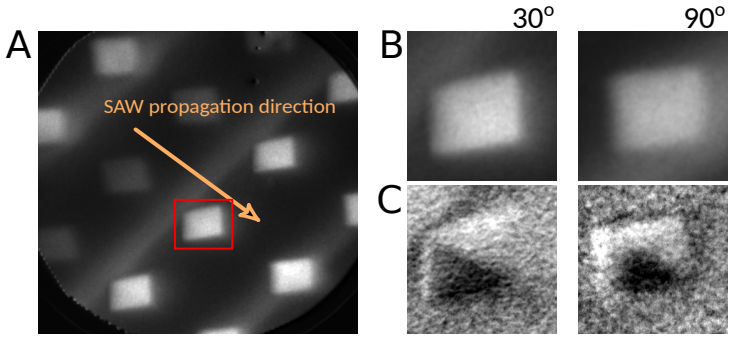

Figure 4.7 **Simultaneous images of SAW and magnetic domains with the new configuration**. **(A)** PEEM image of many Ni squares with a FOV of 50 μm^2. The SAWs are visible at the yellow arrow direction. **(B)** PEEM and **(C)** XMCD images of the 2×2 μm^2 Ni square inside the red box in panel **(A)** when the SAW propagation direction form a 45 deg with the X-rays. Images correspond to phase lapses of 60 deg. Both images are 4×4 μm^2.

The analysis of the domain configuration for the 45 deg tilted Ni squares is plotted in Fig. 4.8 in a similar way than in Fig. 4.2B . However, to analyze the domain configuration, the measurement of the black and white domain areas is not an adequate quantity since the domains do not grow and shrink. Instead we calculate the normalized difference in intensity of the two gray domains normalized by the intensity of the overall black and white domains, $(I(G1) - I(G2))/(I(W) - I(B))$,

see Fig. 4.3A. This new quantity is not zero in absence of strain (0.18 instead) due to the presence of the growth-induced anisotropy. Moreover, we plot, as we did before, the strain curve (in green) and a fit for the data (red curve). The phase between the strain and their magnetic response is smaller for this configuration 90 ps (phase delay of 15± 3 deg)

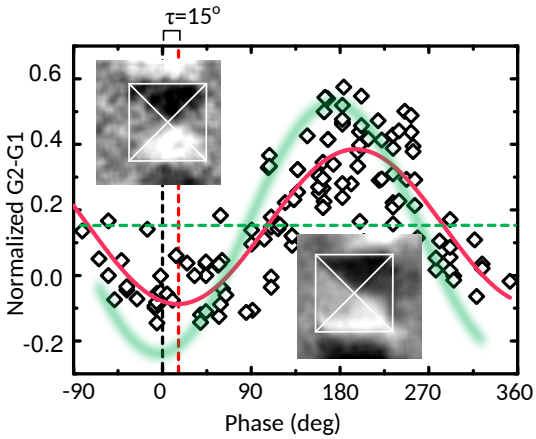

Figure 4.8 **Simultaneous images of SAW and magnetic domains for a 45 deg tilted SAWs**. Analysis of the domain configuration from multiple Ni squares of 2×2 μm^2 as a function of the individual phase with respect to the SAW for the configuration shown in Fig. 4.7A. We compute the intensity difference of the relative normalized gray domains, $(I(G1)-I(G2))/(I(W)-I(B))$. A best fit to the data with a sinusoidal function is plotted in red and a schematic strain wave is plotted in green (with no scale) to indicate the phase values corresponding to maximum and minimum strain corresponding to a response without delay.

4.4 Conclusions

We obtained simultaneous images at the picosecond and nanometer scale of the surface acoustic waves and the corresponding magnetic response on Ni nanostructures by using stroboscopic PEEM and XMCD. We proved the manipulation of the magnetization dynamics with surface acoustic waves at the picosecond scale and we showed how magnetization dynamics depends on its orientation with respect to the SAW-induced strain. We found a delay between the strain wave and the magnetic response of the Ni squares that strongly depends on this orientation.

Chapter 5

Propagating and Standing Spin Waves on a Ni Thin Film

In this chapter we investigate the magnetization dynamics induced by SAWs on an extended Nickel (Ni) thin film deposited on top of a piezoelectric material. Spin waves in a ferromagnet are coherent dispersive waves, with frequencies in the low GHz regime and with wavelengths of hundreds of nanometers. We found that SAWs are able to excite large amplitude spin waves on the magnetic material with up to 25 degrees variation in the magnetization orientation. We study the amplitude of the spin waves as a function of RF power of the SAWs as well as the magnetic field. By changing the frequency of the SAWs, spin waves with different wavelength can be exited. Finally, confronting two SAW's sources standing SAWs as well as standing spin waves are observed in the piezoelectric and in the Ni thin films, respectively.

5.1 Observing Strain Spin Waves

In the region between the two IDTs 2 μm of Ni of about 20 nm of thickness was deposited. In addition to the magnetic strips a copper stripes were also added in order to provide a zero level reference of the XMCD signal. The experimental setup used in this chapter was previously presented in Section 2.3.1 and is based on PEEM-XMCD. Figure 5.1 shows a schematic plot of the sample configuration

where two IDTs are connected to excite both standing and propagating SAWs. The X-rays direction is parallel to the SAWs propagation direction.

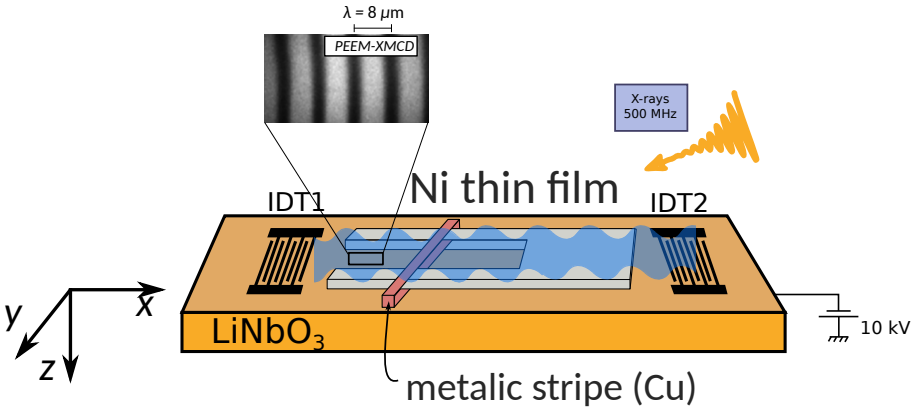

Figure 5.1 **Scheme of the experimental setup**. Schematic plot of the IDTs on the piezoelectric substrate ($LiNbO_3$). The X-rays illuminate the sample with short pulses of 20 ps and a frequency of 500 MHz. The interdigital transducer, IDT, is excited with an AC electric signal which generates a SAW propagating through the $LiNbO_3$. Images at the center of the acoustic path, and away from it, are taken with a PEEM microscope. Vertical stripes result from the piezoelectric voltage associated to the SAW.

SAW-induced strain on the top of the piezoelectric material induces in turn a variation in the magnetic anisotropy of a ferromagnetic material. This variation oscillates between the SAW propagation direction and its orthogonal direction. We applied a small magnetic field, ~5 mT (a magnetic field of about 3 mT is enough to reverse the magnetization of the Ni layer), with an angle of ~50 degrees with respect to the SAW propagation direction in order to maximize the effect of the induced magnetoelastic effect.

In Fig. 5.2 we show two different ways to obtain magnetic contrast with our experimental setup. Figure 5.2A shows an XMCD image of the magnetic contrast of the Ni film. As in previous chapter, the X-rays illuminate the Ni at its L_3 absorption edge energy, see Section 2.3.2, while SAWs were excited at 500 MHz. The ferromagnetic material shows a wave pattern, which presents the same wavelength of the SAWs, whereas on the piezoelectric material, on the top of the image, no contrast is observed. On the other hand, Fig. 5.2B correspond to a subtraction of two PEEM images with the same X-ray helicity and with opposite SAW phase at the

same region of panel A. In this case, both the ferromagnetic and the piezoelectric material present a wave pattern with 8μm wavelength. The contrast in the Ni film is caused by magnetic changes induced by the SAW as in XMCD images, but now we also detect the surface potential in the piezoelectric. XCMD and phase-subtraction PEEM techniques reveal both the variations of the magnetization and the variations produced by SAWs respectively.

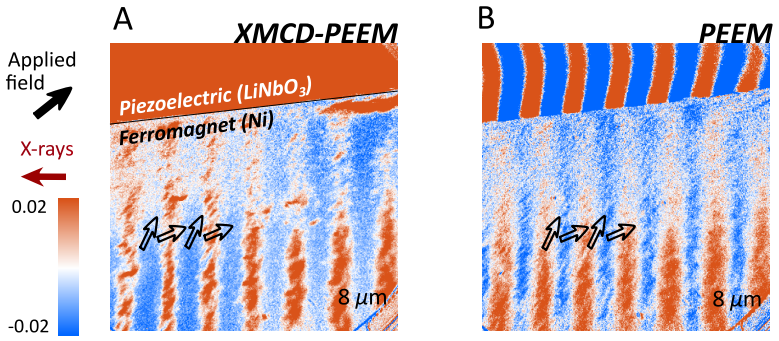

Figure 5.2 **XMCD and subtracted PEEM images**. **(A)** XMCD Image with a field of view of $50 \times 50\mu m^2$ showing both the ferromagnetic (Ni) and the piezoelectric ($LiNbO_3$) materials in presence of a SAW—stripes indicate the presence of a magnetic wave.**(B)** PEEM image of the same location as in **(A)** in presence of a SAW, this time the image corresponds to a subtraction of two images with opposite phases—stripes in the ferromagnet correspond to a magnetic wave and stripes in the piezoelectric correspond to the strain wave.

From Fig. 5.2A we can calculate the amplitude of the strain spin waves. Then, comparing with the magnetization signal at the opposite direction we can estimate the amplitude of the strain spin waves in degrees. The XMCD signal indicate a variation of 0.02 in the magnetic wave and ± 0.05 between opposite polarity magnetic fields, which represent an rotation if the magnetization of the strain spin waves of about 25 degrees (peak to peak).

Figure 5.3 shows traces of the strain spin waves at different RF power of the excitation of SAWs. Using the relation between RF power and the voltage wave amplitude in the piezoelectric similar to Fig. 3.4, in Chapter 2, and converting the voltage amplitude into strain we can summarize dependence of the magnetic wave amplitude with strain. Figure 5.3 shows the linear dependence of the SAW amplitude—the applied strain—with the spin wave amplitude.

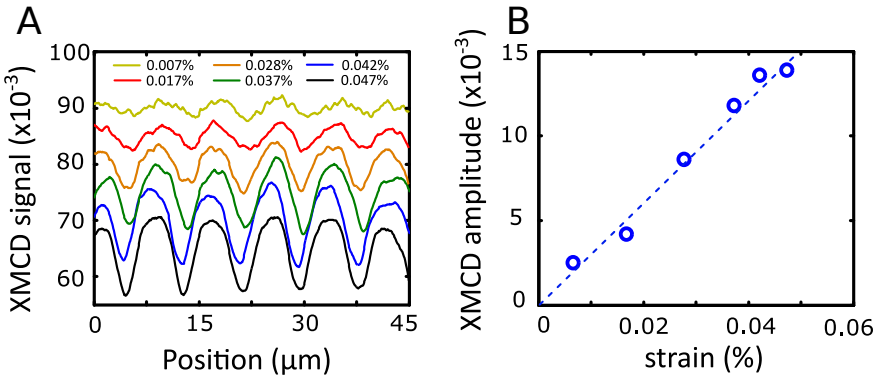

Figure 5.3 **Strain spin waves**. **(A)** Profiles of the strain spin wave in the ferromagnet from XMCD images taken at different SAW amplitude. **(B)** Summarizes the linear dependence of the strain spin wave with the SAW amplitude.

5.1.1 Spin Waves of Different Wavelength

In Section 2.3 we show that at ALBA synchrotron we are able to get access to submultiple of the synchrotron repetition rate by changing the electron bunch filling pattern [38] or by adding an electron gating to the PEEM. The IDTs deposited on the piezoelectric were designed to launch SAWs at 125 MHz as fundamental harmonic and 500 MHz (the ALBA principal repetition rate) as 4th harmonic. Adapting the PEEM microscope with a electron gating we were able to excite strain spin waves at different frequencies 125, 250, 375, and 500 MHz with wavelength of 32, 16, 12, and 8 μm and in all cases reaching a magnetization oscillation of several degrees between opposite SAW phases. Figure 5.4 shows XMCD images of the same Ni region excited at different frequencies.

5.2 The Effect of an External Magnetic Field

We apply an external magnetic field in order to maximize the amplitude of the spin waves. The value of the magnetic field can drastically change the amplitude of the resulting spin waves. Ni is a soft ferromagnetic material and for a low values of the external magnetic field its magnetization aligns completely with the applied field.

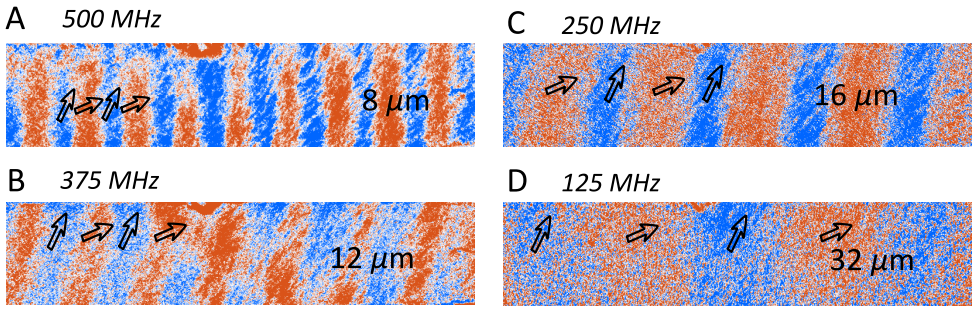

Figure 5.4 **Strain spin waves at different wavelengths**. **(A-D)** XMCD images of strain spin waves of frequencies 500, 375, 250, and 125 MHz having wavelengths of 8, 12, 16, and 32 μm, respectively.

The observed magnetization excitations are magnetization oscillations around the external magnetic field direction driven by the dynamic SAW-induced strain. If we reverse the external magnetic field the magnetization should also reverse. Figure 5.5 shows three XMCD images for different values of the external field where spin waves can be observed as well as the piezoelectric material and the copper stripe. In Fig. 5.5A the magnetization of the spin waves opposes the magnetic field, which is below its coercive value (3 mT). The XMCD image in Fig. 5.5B was taken for a value of 2.3 mT of external field and as the field value is close to coercive field the magnetic region exhibits magnetic domains, regions where the magnetization is aligned with the external field (blue regions). Finally, in Fig. 5.5C the external field is higher enough to reverse all the magnetization. However, along the field sweep the spin waves are present in all three panels, even inside the magnetic domains of Fig. 5.5B.

Blue and black boxes in panels A and C of Fig. 5.5 are used to obtain a profile of the magnetization. Boxes include part of the copper stripes that indicate the reference level in XMCD signal. Figure 5.6A shows a profile of the magnetization in the XMCD's images of panel A and C of Fig. 5.5. Blue line corresponds to the profile of the magnetization inside the blue square in Fig. 5.5A whereas black line corresponds to a profile of the magnetization in black square in Fig. 5.5C. Together with the black line we show another curve with an external field of 9.5 mT, dashed green line, that indicates that a higher value of the magnetic field fixes the magnetization and the spin wave amplitude vanishes. In fact, lower (or

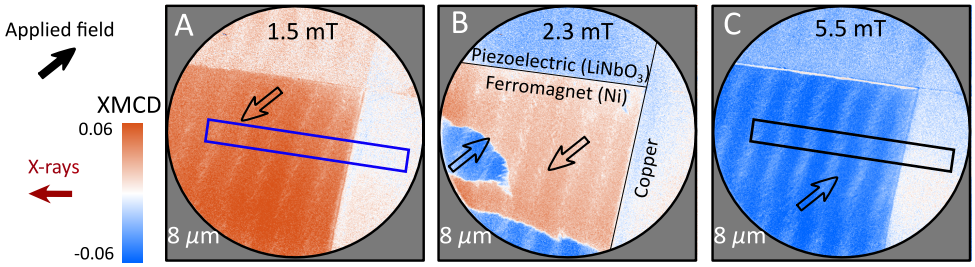

Figure 5.5 **Strain spin wave at different magnetic fields**. **(A-C)** XMCD Image of a strain spin wave under different applied magnetic fields. The image includes the ferromagnetic (Ni) film and the piezoelectric ($LiNbO_3$) substrate together with a non-magnetic metallic structure (Cu). The arrows indicate the magnetization direction within the ferromagnetic film.

zero) values of the external field also result in small-amplitude spin wave, blue line presents a lower amplitude respect to the black line. A summary of the dependence of the amplitude of the spin waves as a function of the external field is shown in Fig. 5.6B, where it is observed that lower as well as higher values of the field result in smaller amplitude. The maximum of the amplitude occurs when the field is about 5.5 mT, black line in panel A.

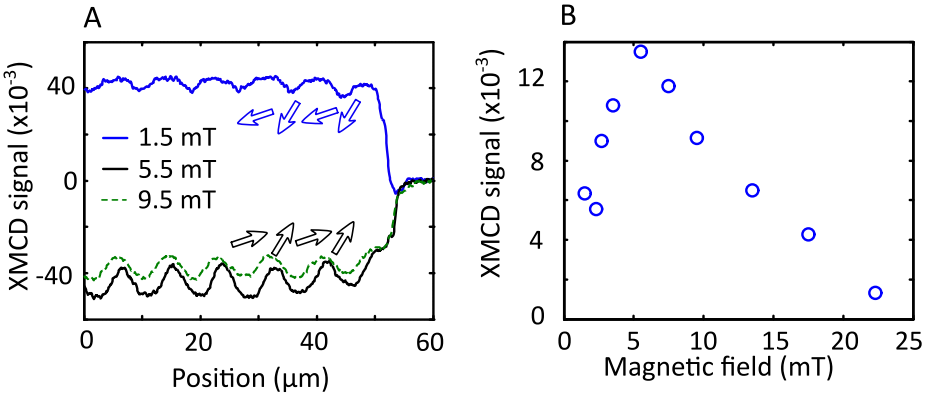

Figure 5.6 **Profiles and amplitude of the strain spin waves at different magnetic fields**. **(A)** Horizontal cuts from Fig. 5.5A and Fig. 5.5C and from an additional field of 9.5 mT (image not shown). Schematic arrows indicate the magnetization direction at different wave points. **(B)** Spin wave amplitude as a function of the external applied field.

5.3 Standing Spin Waves

In Section 3.2 of Chapter 3 we present a PEEM-based technique to quantify propagating (PSAWs) and standing (SSAWs) SAWs. Now, confronting two IDTs we are able to excite interference SAWs patterns and then, spin waves with this SAW-induced patterns. We follow the same procedure used in Section 3.2 to analyze both propagating and standing SAWs. We take sequences of PEEM images for different relative phases respect to the synchrotron frequency. Whereas in Section 3.2 the studied waves were directly observable at the PEEM images, spin waves can not be observed in PEEM images. Then, besides to take a phase sequence of PEEM images, we have to subtract PEEM images with opposite phases as we show in Section 5.1. We obtain a phase sequence of subtracted PEEM (sPEEM) images where spin waves are observable.

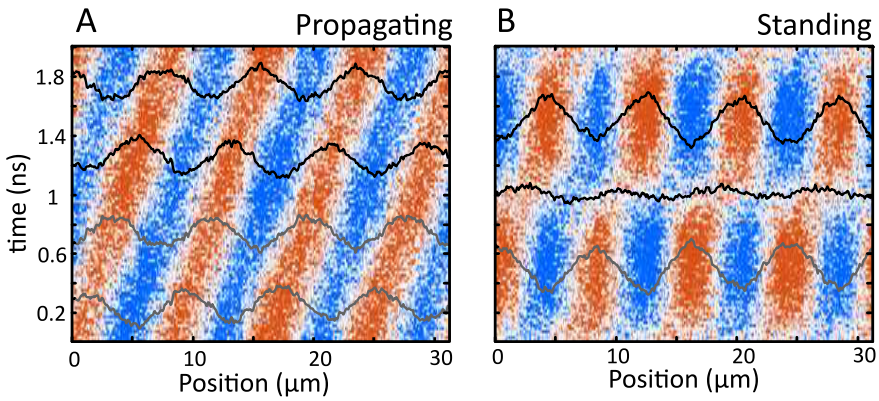

Figure 5.7 **Propagating and standing strain spin waves**. Time evolution of a strain spin wave in a ferromagnetic material (Ni) for a propagating wave **(A)** and for a standing wave **(B)**. The waves are created with two IDT facing each other and separated 6 mm. A small detuning between the wave and the synchrotron frequencies combined with a subtraction of opposite phases allows the visualization of the strain spin waves. Figures correspond to averaged traces of each video image, which can be seen as a different phase or time.

Figure 5.7 shows the phase evolution (Y-axis in units of time) of averaged traces of the oscillation amplitude as a function of the position. Figure 5.7A corresponds to a PSAW and Fig. 5.7B to a SSAW and the colorscale represents the change of the magnetization in time. Whereas for the propagating spin waves there is a

continuous change, for the case of a standing spin wave there are nodes where there is no oscillation of the magnetization. Profiles of the magnetization along the X direction are superposed at both panels showing no amplitude at the nodes.

5.4 Conclusions

We have shown the coupling between SAWs and magnetization dynamics in an extended Ni thin film. We excited spin waves the same wavelength on a Ni thin film and observed them using PEEM-XMCD. Moreover, exciting SAWs at different frequencies (125, 250 and 375 MHz) we have observed spin waves of different wavelength and introducing another SAW's source we were able to observe standing spin waves. From the observation of the magnetization in XMCD images we calculated the amplitude of the spin waves (about 25 deg). Finally, we found that the spin wave amplitude presents a maximum at a small external magnetic field, which might be related to the ferromagnetic resonance.

Part II

Study of the Interaction of the Magnetization Dynamics and the Spin-Polarized Current: Magnetic Solitons

Chapter 6

Introduction

This part of the thesis is dedicated to the control of magnetization dynamics using spin-polarized currents in spin-torque oscillators made of ferromagnetic thin films with perpendicular magnetic anisotropy, and is divided in three chapters: INTRODUCTION, STABILITY OF DISSIPATIVE MAGNETIC SOLITONS and CREATION AND ANNIHILATION OF DISSIPATIVE MAGNETIC SOLITONS. The current chapter, INTRODUCTION, is used to introduce the specific background concepts needed for the understanding of the next chapters and for describing the experimental setup used along Part II. Concepts as giant magnetoresistance and spin-transfer torque are described and used to explain the most common device configurations used to excite magnetization dynamics with the spin-transfer torque effect. Then, the concept of magnetic solitons as a solutions of the Landau-Lifschitz (LL) equation, eq. 1.5, is addressed. Next, we provide a brief state of the art regarding the use of spin-polarized currents in spin-torque oscillators to magnetic thin films. Finally, the experimental setup is described. We show how magnetoresistance is used to study our magnetic samples when we excite them with spin-polarized currents through the spin-transfer torque effect.

6.1 Background and Definitions

6.1.1 Giant Magnetoresistance

Magnetoresistance (MR) is the tendency of a material to change the value of its electrical resistance when an external magnetic field is applied. William Thomson (Lord Kelvin) first discovered ordinary magnetoresistance in 1856. He experimented with Iron and Nickel and discovered that the resistance increases when the current is in the same direction as the magnetic force and decreases when the current is at 90° to the magnetic force. The effect discovered by Lord Kelvin is known as *anisotropic magnetoresistance* (AMR) [46]. There is a variety of effects that can be called magnetoresistance and are classified by the material where the MR effect occurs. Geometrical magnetoresistance or the common positive magnetoresistance occurs in non-magnetic metals and semiconductors. In magnetic materials it can be found the negative magnetoresistance or the anisotropic magnetoresistance. Finally, in magnetic multilayers giant magnetoresistance (GMR)[47, 48], tunnel magnetoresistance (TMR)[49], colossal magnetoresistance (CMR)[50], and extraordinary magnetoresistance (EMR)[51] can be observed.

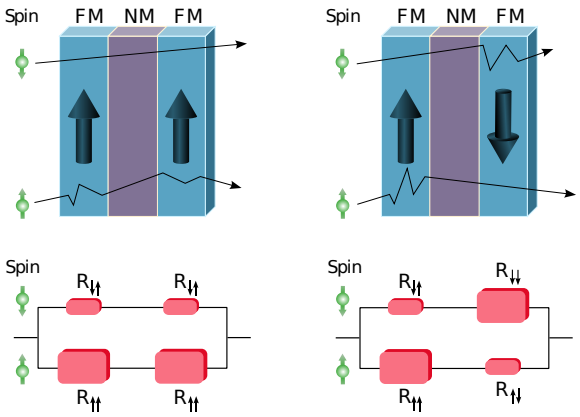

Figure 6.1 **Scheme of a P-state and AP-state configuration**. GMR effect in a magnetic bilayer structure consisting of two ferromagnetic (FM) layers separated by a non magnetic layer (NM). Electrons scatter differently according to the orientations of their spins. The scattering may be considered as an equivalent resistance. Adapted from "Spin-valve GMR" by Guillom, used under CC.

In 2007, Albert Fert and Peter Grünberg were jointly awarded the Nobel Prize for the discovery of GMR, which is applied in magnetic field sensors to read data in hard disk drives, biosensors and other devices [52]. GMR magnetic structures are also used in magnetoresistive random-access memory (MRAM) as cells that store one bit of information [18].

In bilayer structures that can have their relative magnetization parallel (P) or antiparallel (AP), the resistance is lower in the P-state than in the AP-state. The variations can reach 50% [48] and are produced by a difference in the scattering properties of electrons having their spins parallel or antiparallel to the magnetization of the layer, see Fig. 6.1. A normal incident current is assumed to contain the same proportion of parallel and antiparallel electron spins, the scattering of both components must be taken into account when electrons traverse the multilayer. Bottom panels of Fig. 6.1 show the two possible situations being the total resistance of the P-state lower than the AP-state. This effect is specially useful because the magnetization of one layer may be controlled with, for example, an external field, which allows a control on the measured resistance.

6.1.2 Spin-Transfer Torque

There is an additional effect associated to the electrons flowing through a magnetic layer. In 1996 Slonczewski predicted the *spin-transfer torque* effect (STT) [53]. He predicted that a spin-polarized current creates a mutual transference of spin angular momentum with a magnetic layer, which is manifested in their dynamic response, see Fig. 6.2A.

The STT effect depends on the polarization direction of the electrons and the strength and sign of the current. For a current polarized parallel to the magnetization the STT vanishes and in other cases, depending on the sign of the current, the effect of the spin-polarized current opposes or favors damping, see Fig. 6.2B.

The STT effect can be model as a new phenomenological term in the LL equation. This term should depend on the polarization direction of the current, the magnetization in the layer, and the sign and strength of the current. Rewriting the LL equation studied in Section 1.3 and taking into the account the STT effect we

obtain

$$\frac{\mathrm{d}\boldsymbol{M}}{\mathrm{d}t} = |\gamma|\mu_0\Big[\boldsymbol{M}\times\boldsymbol{H}_{\mathrm{eff}}\Big] - \alpha\frac{\gamma\mu_0}{M_0}\boldsymbol{M}\times\Big[\boldsymbol{M}\times\boldsymbol{H}_{\mathrm{eff}}\Big] + \underbrace{\sigma\boldsymbol{M}\times\Big[\boldsymbol{M}\times\boldsymbol{m}_{\mathrm{p}}\Big]}_{\text{STT term}}, \tag{6.1}$$

being $\boldsymbol{M} = \boldsymbol{M}(\boldsymbol{r},t)$, $\boldsymbol{H}_{\mathrm{eff}} = \boldsymbol{H}_{\mathrm{eff}}(\boldsymbol{r},t)$, $\boldsymbol{m}_{\mathrm{p}}$ the direction of the polarization of the spin-polarized current and σ is proportional to the current density (A/m^2) (for more details on the parameters see Appendix A). The vector cross product, $\boldsymbol{M}\times\big[\boldsymbol{M}\times\boldsymbol{m}_{\mathrm{p}}\big]$, is in the direction of spin angular momentum transverse to the magnetization and in the plane containing $\boldsymbol{M}$ and $\boldsymbol{m}_{\mathrm{p}}$ [54]

$$\boldsymbol{M}\times\big[\boldsymbol{M}\times\boldsymbol{m}_{\mathrm{p}}\big] = \big(\boldsymbol{M}\cdot\boldsymbol{m}_{\mathrm{p}}\big)\boldsymbol{M} - \boldsymbol{m}_{\mathrm{p}}.$$

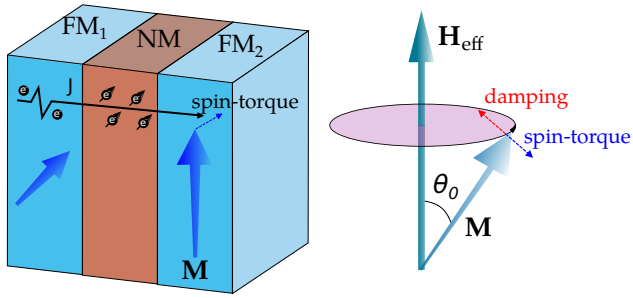

Figure 6.2 **Scheme of the STT effect**. Electrons flow through the first magnetic layer and become polarized. The second magnetic layer exchanges momentum with those polarized electrons that induce a magnetization dynamics.

The ferromagnetic sandwich configuration (FM/NM/FM of Fig. 6.1) represents the common configuration for STT devices. The first FM_1 layer has fixed magnetization and acts as a *polarizing layer* (PL), which is the responsible of the electron spin polarization. The FM_2 layer is called the *free layer* (FL) and its magnetization may be perturbed by the polarized electrons. The interaction between polarized electrons and the magnetization in a FL may change the relative orientation between the PL and the FL, and hence produce a change in the resistance, typically through the GMR.

Recently, a new experimental approach, which considers a pure spin currents, was proved on Pt|[Co|Ni] structures [55] in order to produce STT effect. The device is based on the spin Hall effect in Pt [56], which converts a dc electrical current flowing in the plane into a spin current flowing out of plane, with spin polarization oriented in-plane, perpendicular to the direction of current. The spin current is injected into the FL, exerting STT on its magnetization. However, in this thesis we are going to work only with the multilayer approach.

6.1.3 Spin-Transfer Torque Nano-Oscillators

High-current densities are needed to produce excitations in a FL. Reducing the area traversed by current we achieve current densities in the order of $10^6 - 10^7$ A/cm^2. In recent years two different device configurations emerged [57]. On the one hand, a non-magnetic metal is used as electrical contact to the magnetic layer in a small region, $50 - 200$ nm in diameter, the so called *nanocontact*. The current passes through the FL, which is an extended layer, see Fig. 6.3A. On the other hand, the whole magnetic layer is used as an electrical contact and the current passes through it. This configurations is known as *nanopilar*, see Fig. 6.3B.

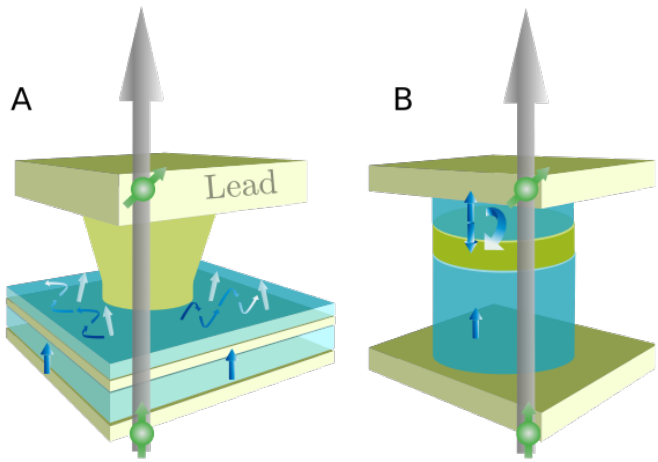

Figure 6.3 **STNOs configurations**. Two different configurations to obtain high-current densities on magnetic layers. **(A)** Nanocontact, **(B)** nanopillar with two ferromagnetic materials. Adapted from Fig. 2 in ref [57]

Depending on the device configuration the result of the application of spin-polarized current may be different. The magnetization of a FL in a nanopilar can be completely switched [58, 59] or exhibit a magnetic vortex configuration [60]. If we consider an extend magnetic layer with a non-magnetic nanocontact on top, the application of spin-polarized current results in a big range of magnetic configurations such as spin wave generation [61], magnetic bullets [62, 63], and magnetic vortices [64].

A *spin torque nano-oscillator* (STNO) is a device that presents oscillating magnetization excited beneath a nanocontact and in some cases spin waves emission. The magnetization dynamics induce a time-dependent change in the resistance at the characteristic ferromagnetic frequency (in the GHz range) and the measurement of the dc resistance as a function of the applied current points out the relative alignment between the FL and the PL due to the MR.

6.1.4 Magnetic Solitons

Solitons are localized excitations that occur in dynamical systems. In the case of magnetic solitons, these local excitations are produced by an attractive potential of the spin waves occurring from the precession of the magnetization around equilibrium, when there is no damping [65]. Magnetic solitons are consider as a dynamical solutions of the conservative LL equation (Eq. 1.5). These solutions were extensively studied by Ivanov and Kosevich between 1976 and 1990 [65, 66]. They theorized that the spin waves generated by the oscillations of the magnetization in a uniaxial ferromagnet interacted in an effective attractive potential that localized the excitation. Ivanov et al. wrote: “The bound state of a large number of magnons is a *magnon drop*. This drop is in fact the embryo of a region with opposite direction of the magnetization in a infinite single-domain ferromagnet”.

Real materials have non-zero damping, making complicated the existence of magnetic solitons. Hoefer et al. proposed that a particular magnetic soliton, *dissipative droplet soliton*, can be generated in materials with damping thanks to the spin-transfer torque effect, which is produced by the application of a spin-polarized current [67]. Dissipative magnetic droplet solitons, hereafter referred to as droplet solitons, are related to the conservative magnon droplets that have

been studied in uniaxial ferromagnets by Ivanov and Kosevich. Droplet solitons are expected to be strongly localized in the contact region, as well as to have spins precessing in phase in the film plane [67]. In addition, with sufficient current the magnetization in the contact has been predicted to be almost completely reversed relative to the film magnetization outside the contact.

Solutions for the LL equation considering damping were extensively studied by Hoefer et al. in thin film ferromagnetic layer with perpendicular magnetic anisotropy (PMA). Those solutions can be classified according with their topology trough the topological charge or skyrmion number (SN) of the magnetization vector $\boldsymbol{M}$ in two dimensions [68]

$$SN = \frac{1}{4\pi}\int \boldsymbol{M}\Big(\frac{\partial \boldsymbol{M}}{\partial x}\times\frac{\partial \boldsymbol{M}}{\partial y}\Big)\mathrm{d}x\mathrm{d}y. \tag{6.2}$$

Along this thesis both $SN = 0, 1$ will be considered. Whereas $SN = 0$, the so called *droplet soliton*, can be continuously deformed to the uniform ferromagnetic state the $SN = 1$ soliton presents a topological spin texture different to the ground or FM state. Figure 6.4 shows a scheme of the domain wall of a magnetic soliton. On the one hand, panel a shows the magnetization of the domain wall of a non-topological soliton, $SN = 0$, whereas on the other hand, panel b shows how a topological domain wall looks like. The topology of localized solitons is concentrated on the domain wall that separates the antiparallel domains.

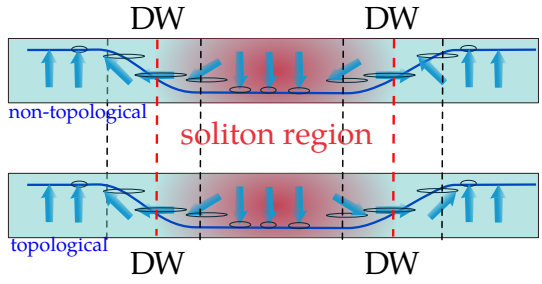

Figure 6.4 **Domain Walls**. Scheme of the domain wall of a non-topological and topological magnetic solitons.

6.2 State of the Art

The first work to consider the existence of spin-transfer torque dates from late 1970s, when Berger et al. predicted that spin-transfer torque should be able to move magnetic domain walls [69]. A few years later, Berger's group published the experimental evidence that domain walls in ferromagnetic films can be moved by the application of large current pulses [70, 71]. The fact that the current was as high as 45 A was an impediment in order to popularize the result.

In 1996, Slonczewski [53] and Berger [72] independently predicted that current flowing perpendicular to the plane in a metallic multilayer could generate a spin-transfer torque strong enough to reorient the magnetization in one of the layers. In magnetic nanopillars that consist of a thick and a thin magnetic layer separated by a nonmagnetic layer, the thick-fixed layer polarizes the current and dynamics is usually induced in the thin-free layer. Spin-transfer torque competes with damping and, at a threshold current, leads to excitation of the magnetization, which results in spin waves on the thin magnetic layer. When these spin waves have a frequency that is less than the lowest propagating spin-wave mode in the ferromagnetic film (the ferromagnetic resonance (FMR) frequency) they are localized in the contact region. The first experimental observations of a magnetization switching driven by spin-polarized current were published during the turn of the century. Katine et al. [73] and Myers et al. [74] reported, using GMR effect, the switching of magnetization in Co|Cu|Co sandwich structures. A few years later, high-frequency dynamics were reported [75–77].

Nowadays, MRAM is a commercial non-volatile memory based on the spin-transfer torque effect [18], providing a low-power consumption and high speed response (in the GHz range). Spin-transfer torque devices have been also proposed as wave emitters and detectors in the GHz range and as an emulator of both neuron and synapses in a neural networ [19].

In free layers with perpendicular magnetic anisotropy (PMA) the excitation of localized spin waves has been predicted by Hoefer et al. to lead the excitation of dissipative droplet solitons, which are expected to be strongly localized in the nanocontact region, as well as to have spins precessing in phase in the film plane [67]. The first experimental evidence of a droplet nucleation was publish

in 2013 [62] and it was extensively studied during the following years [63, 78, 79]. Magnetic droplets were also directly observed using X-ray microscopy [80]. Moreover, topological magnetic solitons (the topological homologous of magnetic droplets) were also predicted by Zhou et al. in 2015 through micromagnetic simulation in PMA materials [81].

Applications require high control of the nucleation and annihilation of magnetic solitons as well as an understanding of their intrinsic stability and their behavior against external perturbations. In this part of the thesis we focus on the study of those characteristic processes. We present both measurements and simulations regarding two different magnetic solitons: the dissipative droplet soliton [67] and the topological homologous, the dynamical skyrmion [81].

6.3 Experimental Setup

Along this part of the thesis we are going to use an electrical nanocontact configuration to an extended magnetic multilayer for experiments and simulations. The layer stack consisted of a Co and Ni multilayer, 6 × (0.2Co|0.6Ni) capped with 0.2Co|5 Pt, separated by 10Cu from a 10Py layer (thicknesses in nanometres). The Cu spacer layer was chosen to magnetically decouple the Py layer with in-plane anisotropy from the Co|Ni multilayer with out-of-plane anisotropy, and the Pt capping layer was used to further enhance the interface-induced perpendicular magnetic anisotropy of the Co|Ni multilayer. The small contacts were patterned by electron-beam lithography with diameters in the range of 80 − 150 nm. Figure 6.5 shows a scheme of the magnetic multilayer and SEM images of a nanocontact of 150 nm on Fig. 6.5A and 100 nm in Fig. 6.5B. A complete description of the fabrication of the samples is available in the Method's section of the ref. [63] and a characterization of similar layer stacks can be found in ref. [82].

The experimental setup is described in Fig. 6.6. Electrical resistances is measured by contacting a non-magnetic probe to the gold pads. The current flows from the bottom electrode to the top electrode only through the nanocontact, because it is a low-resistance area in comparison with the dielectric area. The probes are also used to measure the low and high frequency electrical response of the sample. In order to tilt the fixed layer an out-of-plane field (up to 1.0 T)

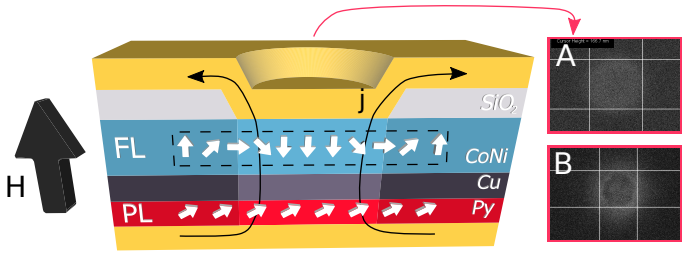

Figure 6.5 **Scheme of the sample and SEM images of nanocontacts.** Scheme of the multilayer sample. The current flows through the nanocontact region interacting with the magnetic layers. **(A)** and **(B)** are SEM images of electrical nanocontacs of nominal diameters 150 nm and 100 nm, respectively. Holes are etched into the SiO_x thin layers and images are taken before depositing the top electrode.

is applied and an in-plane field could be also applied. The sample is connected to a Keithley SourceMeter, that acts as a current source and voltmeter, and to a spectrum analyzer (SA), with working frequencies in the range 1 MHz – 26.5 GHz. The current source and voltmeter is connected to the ac filter of a bias-tee whereas the SA was connected to the dc filter. To contact the sample both wire bondings and probes are used. However, if we are interested in the high-frequency response of the sample (above $1-2$ GHz) only probes can be used. Whereas wire bonding provides better dc MR signal since electrical contact are more stable, probes allow us to make measurements of both high- and low-frequencies in detriment of the dc resistance signal.

The GMR effect produces a change in the resistance when a current flows through the multilayer stack since the PL polarizes the electrons and depending on the polarization—the applied out-of-plane field controls the PL—the resulting resistance could be lower if PL and FL are aligned or higher otherwise. Considering R_P and R_{AP} the resistance when the PL and the FL are parallel or antiparallel we can write the total resistance as

$$\bar{R} = R_0 \frac{1 - \mathbf{m}_{FL} \cdot \mathbf{m}_{PL}}{2}, \quad R_0 = \frac{R_{AP} - R_P}{R_P},$$

where $\mathbf{m}_{FL}$ and $\mathbf{m}_{PL}$ represent the normalized magnetization vector FL and PL. The out-of-plane field tilts the PL changing the resulting resistance. A scheme of the value of the resistance as a function of field values can be seen in Fig. 6.7A.

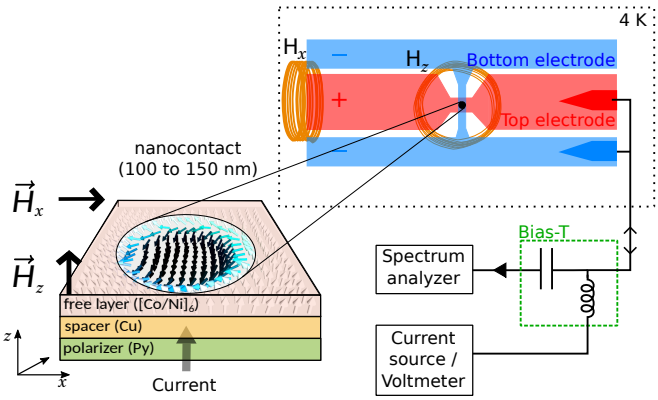

Figure 6.6 **Scheme of the experimental setup.** Scheme of the experimental setup. Top and bottom electrodes are contacted by a probe and the current flows through the sample that is a layer stack. The nanocontact region is represented by the non-shaded area on the top of the FL.

The central point represents the initial state of both FL and PL. Without external field FL and PL are perpendicular since the Py—the PL—present an in-plane magnetization whereas the FL have an intrinsic PMA. Then, increasing the value of

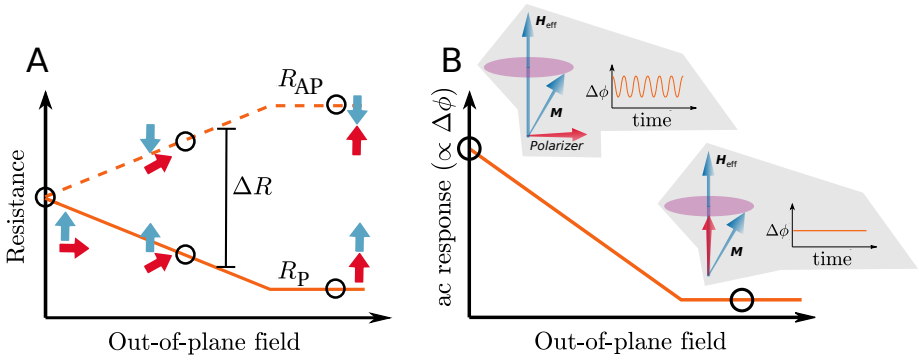

Figure 6.7 **dc and ac resistance response of the layer stack.** **(A)** Magnetoresistance as function of the applied out-of-plane field is shown. The difference in resistance when the FL magnetization reverses is noted. **(B)** Schematics of the ac response measured with the SA, as a function of the out-of-plane field. As the field is increased, the ac response due to the oscillation of the FL around the equilibrium vanishes.

the field the PL tilts out of the plane and aligns with the FL resulting in a reduction of the total resistance, continuous yellow line in Fig. 6.7A. On the other hand, if we are able to fix the FL magnetization in opposite direction to the out-of-plane

applied field then the resulting resistance as a function of the value of the field should describe the dash line, increasing the resistance value since the PL, at the saturation value, becomes antiparallel to the FL.

Figure 6.7B shows the ac response of the resistance measured with the SA. The angle in the XY-plane between the FL and the PL change in time since the FL is oscillating around the effective field. Therefore, a peak appears in the SA spectra response at the frequency of the signal, if any, and its height is proportional to the amplitude of the oscillation. However, the amplitude of the peak also depends on how tilted the PL is. In fact, the amplitude decreases as a function of the out-of-plane field since for higher values of the field the PL and the FL are parallel.

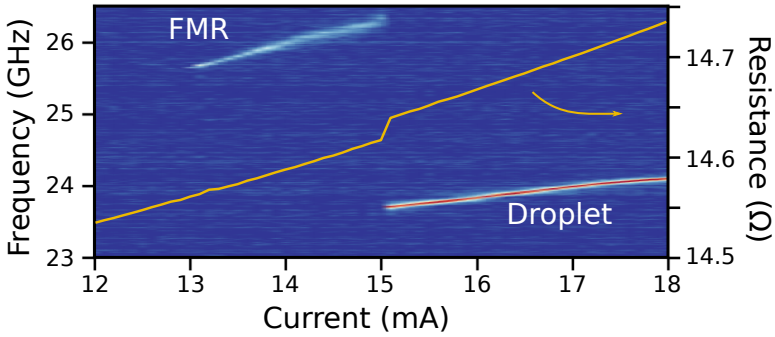

Figure 6.8 **ac resistance response of the layer stack**. High frequency spectra, left Y-axis, and MR curve, right Y-axis, as a function of the current. The nucleation of the droplet is accompanied by a decrease in the high frequency peak.

The step increase in the resistances curve arises from the nucleation of a droplet since the magnetization inside the NC makes the system transit from an almost parallel state, continuous lines in Fig. 6.7A, to a antiparallel state, dash line. Both process, creation and annihilation, cause a step increase or decrease in the nanocontact resistances since the system moves between parallel and antiparallel states. Together with the step decrease in the resistances, the droplet leaves a signal of their nucleation in the ac component of the resistance. Figure 6.8 shows the high frequency spectra response (frequencies in the range 1 - 26 GHz) of the sample (left Y-axis) and the resistance curve (right Y-axis) as a function of the

applied current. The resistance step increase is accompanied by a step decrease in the high frequency spectra peak pointing the droplet nucleation at 15 mA.

For currents below 15 mA the magnetization beneath the NC is oscillating at the ferromagnetic resonance (FMR) around the effective field. Once the current is higher enough the STT component overcomes the damping and the magnetization switches. Then, the effective field is reduced, part of the magnetization—the droplet region—is now pointing down, as well as the frequency of the oscillations since both magnitudes are proportional.

Chapter 7

Stability of Dissipative Magnetic Droplet Solitons

In this chapter room- and low-temperature measurements of droplets are presented. Through the measurement of the low-frequency resistance response of the sample we discuss about the stability of the nucleated droplet states. We relate low-frequency signal with the movement of the droplet beneath the nanocontact as a whole object and show that the introduction of in-plane fields generates more low-frequency signal. We show that, in presence of a gradient of in-plane fields, the droplet moves out of the nanocontact and annihilates because of the damping; immediately another droplet nucleates beneath the nanocontact and the process repeats with a frequency of hundreds of MHz. Low-temperature measurements show that the application of an in-plane field can split a stable droplet state into a superposition of different unstable states. In addition to room- and low-temperature measurements, simulations are used to support the discussion. Room-temperature measurements were performed at the University of Barcelona by Sergi Lendínez at the beginning of my PhD. I performed the simulations that support the idea of drift instabilities. Low-temperature measurements were performed during my stay at the New York University. This time, I performed both measurements and simulations.

7.1 Magnetic Droplets at Room Temperature

Droplets, as indicated in Section 6.3, are excited in a Co|Ni free multilayer by a polarized current. Figure 7.1 shows a summary of the measurements of the nucleation and the annihilation of the droplet for this a sample with 150 nm of diameter at different magnetic fields. Figure 7.1A shows the resistance curves as a function of the current at different fields. The current was swept ramp up to 35 mA and then back to 0 mA. Although we detect the onset at fields $0.5\,\mathrm{T} < \mu_0 H < 0.9\,\mathrm{T}$, it is not until larger field values, $\mu_0 H > 0.9\,\mathrm{T}$, that we observe an hysteretic behavior. In Fig. 7.1B we plot a state map representing nucleation and annihilation currents for all measured fields.

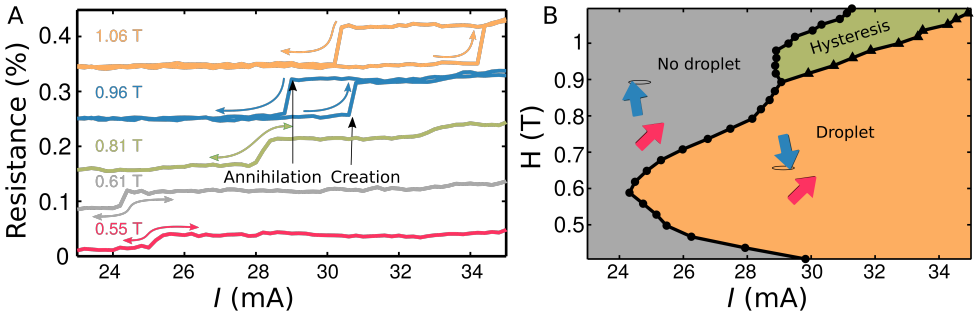

Figure 7.1 **Summary of the nucleation and annihilation of the droplet.** **(A)** Measured normalized resistance $\overline{R} = R/R_P$ as a function of applied current for fields ranging from 0.5 to 1.1 T. **(B)** Stability map of the droplet soliton: on the hysteretic area, triangles show creation of the droplet, and dots annihilation.

High-frequency resistance signal of the droplet at a fixed out-of-plane field of $\mu_0 H = 710$ mT is shown in Fig. 7.2. At the onset current the characteristic frequency of the droplet excitation is $f \approx 20.1$ GHz, below the corresponding FMR frequency (27.5 GHz, measured in the same film).

Now, we focus on the low frequency resistance signal (in the range of hundreds of MHz) that gives us information about the oscillatory dynamics related to the droplet soliton as a whole object. Accompanying the droplet nucleation, we find a strong and broad oscillating signal at about 300 MHz with a weak dependence on applied field and current. The low-frequency signal appears together with the step in resistance—nucleation of the droplet—of all samples in the 100 – 800 MHz

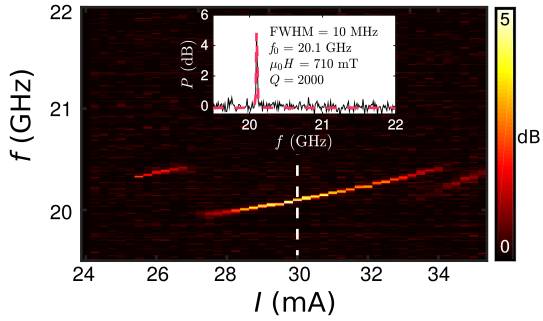

Figure 7.2 **High-frequency spectra**. High-frequency spectra, color scale in dB above the baseline noise, as a function of applied current for a field of 710 mT. (Inset) Signal at a fixed current of $I = 30$ mA (white dashed line). The fitted data (red dashed line) shows a narrow peak with a FWHM = 10 MHz, and quality factor $Q \approx 2000$.

range. However, some of the peaks are well defined whereas in some cases peaks are much broader structures. Figure 7.3 shows the low-frequency spectra as a function of the applied current for different fields. Whereas Fig. 7.3A and Fig. 7.3B consider a field that do not saturate the PL, at Fig. 7.3C and Fig. 7.3D spins in both PL and FL are aligned since PL is saturated. All four cases exhibit low-frequency peaks, in fact, at higher fields the peaks are better defined, which tells us that the low-frequency signal is not a precessing dynamics of the FL magnetization but a motion of the whole droplet as schematically indicated the inset in Fig. 7.3D.

To control the low-frequency signal we use in-plane fields, which in a specific range of values enhance the power of the low-frequency signal. In Fig. 7.4 we measure both dc and low-frequency resistance signals as a function of the angle of the applied field, perpendicular to the plane at an angle $\theta = 0$ deg. The droplet can be sustained for value between -15 to 15 deg field angle (higher values on the resistance signal), however, for values above $\theta = \pm 15$ deg the droplet is annihilated. The low-frequency signal increases with the angle, i.e., with the application of in-plane fields. Stronger low-frequency signal was found for $\theta > 0$ compared to $\theta < 0$ indicating that the low-frequency dynamics depends on the geometry of the in-plane field.

Room temperature droplet measurements show a bistability region for high values of the out-of-plane and exhibit a low-frequency signal raveling the move-

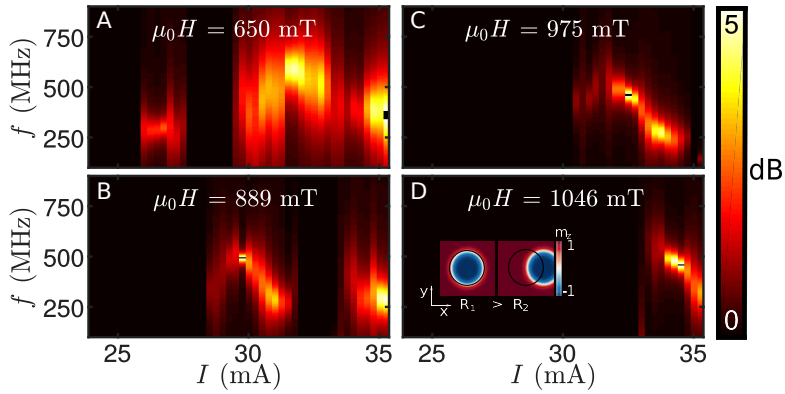

Figure 7.3 **Low-frequency spectra at different fields**. Low-frequency spectra, color scale in dB above the baseline noise, as a function of applied current for fields of **(A)** 650 mT, **(B)** 889 mT, **(C)** 975 mT, and **(D)** 1046 mT. The inset in panel **(D)** is a schematic configuration of a droplet centered beneath the nanocontact (left image) and the same soliton moved sideways (right image).

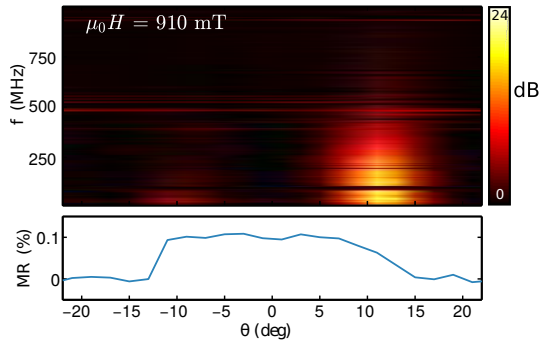

Figure 7.4 **Low-frequency and resistances as a function of the in-plane field**. Top panel: Low frequency spectra as a function of the angle of the applied field for a field of 910 mT. Bottom panel: MR as a function of the angle of the applied field for the same sample. The two measurements were taken at the same time for an applied current of 40 mA.

ment of the droplet as a whole object. The appearance of this signal shows a dependence on both out-of-plane and in-plane magnetic fields.

7.1.1 Micromagnetic Simulation of Drift Instabilities

In order to understand the dynamics causing the low-frequency signal we modeled the nanocontact region and the droplet excitations with micromagnetic simula-

tions (see Appendix A for simulations details). The material parameters were taken from characterization [63] and we consider no temperature effects whereas Oersted fields effects added to the model (full code in Appendix A). A circular nanocontact of 150 nm in diameter was modeled to fit the nominal diameter of the measured samples. We used a damping parameter $\alpha = 0.03$ for the FL and adjusted the spin-torque efficiency to obtain a droplet onset map similar to the measured in Fig. 7.1B.

We simulate the droplet considering an out-of-plane magnetic field of 1.1 T. After some stabilization time (few ns) an in-plane field is applied and causes a dramatic change: the droplet shifts in the direction perpendicular to the applied in-plane field and annihilates when it gets out of the NC region because of the damping. Immediately, a new droplet soliton is created beneath the NC. This process has a frequency, for the simulated parameters, of about 150 MHz and hardly depends on the out-of-plane field and the applied current values.

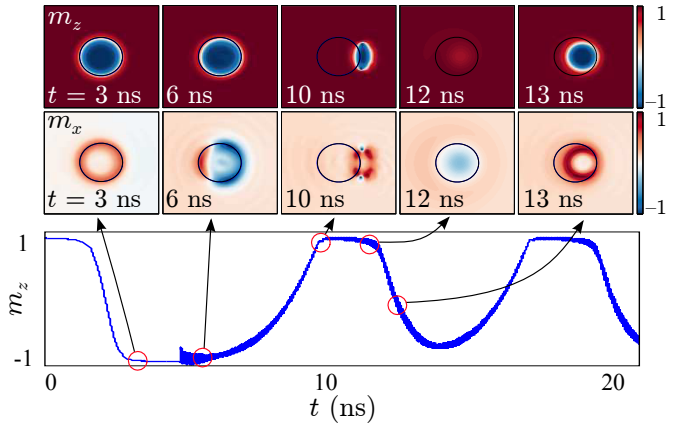

Figure 7.5 **The effect of an in-plane field on a droplet**. Time evolution of the droplet soliton in an applied field of 1.1 T perpendicular to the film plane first and with an additional in-plane field (y direction) of 0.15 T for times $t \geq 5$ ns. The upper panels show magnetization maps for m_z, and m_x, at particular times of the simulation. Images correspond to a 400 × 400 nm^2 field view. The nanocontact region is outlined in black. The lower panel shows the time evolution of the perpendicular component of the magnetization m_z, averaged in the nanocontact area.

Figure 7.5 shows the time evolution of the droplet soliton with an applied field of 1.1 T perpendicular to the film plane and then, after 5 ns, with an additional in-

plane field of 0.15 T (equivalent to a magnetic field with an angle of $\theta \approx 8$ degrees). The upper panels show snapshots of the magnetization, for the components perpendicular to the plane, m_z, and in the plane, m_x, at particular times of the simulation. The lower panel shows the time evolution of the average of the m_z inside the NC area. During the first 5 ns we apply only an out-of-plane magnetic field of 1.1 T and observe how a droplet forms having all spins precessing in phase (see panels for $t = 3$ ns). At $t > 5$ ns an in-plane field, 0.15 T, is applied in the y direction. This creates a drift instability, an imbalance in the precession phases that shifts the droplet in the x direction (perpendicular to the applied field) until it annihilates (see panels for $t = 6$ and 10 ns). At 12 ns it seems that the droplet has dissipated but a new excitation is being created (see panels for $t = 12$ and 13 ns). We note that the time average of m_z beneath the NC—that is the measurable quantity using any dc technique—is only a 36 % of the total, or equivalent to a precession angle of 73 degrees[80].

In our measurements shown in Fig. 7.3 low-frequency dynamics appear even when the applied field was perpendicular to the film. Certainly, experiments are more complex than simulations, which do not exhibit low-frequency dynamics when the field is totally perpendicular. However, simulations give us the intuition that instabilities are produced by asymmetries in the system. Thus, we introduce asymmetric parameters in the simulations. We find that a variation in the anisotropy of only 1 % between the two halves of a nanocontact produces the same effect—with almost the same annihilation and creation frequency. In general we find that any asymmetry in the effective field causes a drift instability and results in an oscillatory signal (drift resonance) of hundreds of MHz corresponding to annihilation and creation of the soliton excitation. Both Figs. 7.6 and 7.7 show the time evolution of the magnetization for the case with a variation in the anisotropy and a variation in the perpendicular applied field inside the nanocontact region, which was divided in half and considered the parameters from each part slightly different. In the first case we have considered that the anisotropy constant value of the two parts of the nanocontact differ by 1 %. Figure 7.6 shows the evolution of the soliton excitation upon an applied perpendicular field of $\mu_0 H_z = 1.1$ T. We notice that in this case the dynamic annihilation and creation occurs at a lower frequency of about 50 MHz. In the second case, we applied a perpendicular field

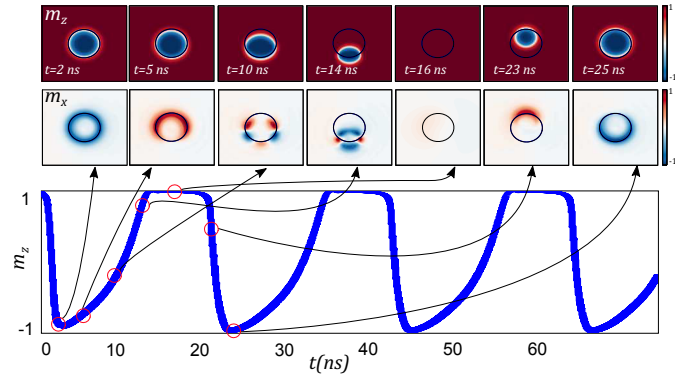

Figure 7.6 **The effect of a variation in the anisotropy at the nanocontact region**. Time evolution of the droplet soliton upon an applied field of 1.1 T perpendicular to the film plane and with an anisotropy that varies 1 % in the two halves of the nanocontact. The upper panels show magnetization maps for m_z, and m_x, at particular times of the simulation. Images correspond to a 400 × 400 nm^2 field view. The contact region is outlined in blue. The lower panel shows the time evolution of the perpendicular component of the magnetization m_z, in the nanocontact area.

of $\mu_0 H_z$ = 1.1 T to one half and a ~1 % higher in the other half ($\mu_0 H_z$ = 1.11 T). Figure 7.7 shows the evolution of the droplet soliton; During the first 3 ns the out-of-plane field of 1.1 T is uniform in all the nanocontact and then the slight variation of 1 % is introduced in half of the nanocontact. Upper panels shows how the soliton excitation shifts in the y direction until it is annihilated and a new excitation appears. The measured low frequency is very similar to the frequency we obtained in presence of an in-plane field (Fig. 7.5).

7.2 Magnetic Droplets at Low Temperature

The temperature in magnetic systems induces noise, thermal noise, which reduces effectively the magnetic energy barriers: the magnetization can change their state just assisted by temperature. Thus, in order to minimize those thermal effects, in this section experiments are done at low temperatures. The sample presets the same layer stack used in previous section with a nanocontact of 150 nm. Low temperature is achieved with a cryoprobe station at constant temperature (T = 4 K), which is equipped with two superconducting magnets: an out-of-plane magnet

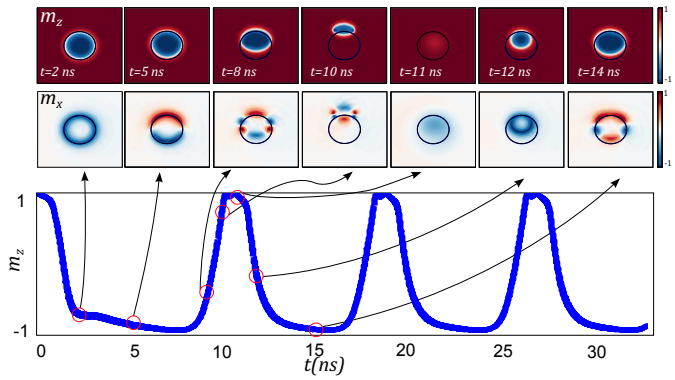

Figure 7.7 **The effect of a variation in the out-of-plane field at the nanocontact region**. Time evolution of the droplet soliton upon an applied field of 1.1 T perpendicular to the film plane ($t < 3$ ns), and with an additional field of 0.01 T in one half of the point contact, applied at $t = 3$ ns. The upper panels show magnetization maps for m_z, and m_x, at particular times of the simulation. Images correspond to a 400 × 400 nm^2 field view. The contact region is outlined in black. The lower panel shows the time evolution of the perpendicular component of the magnetization m_z, in the nanocontact area.

to apply fields up to 1T (H_z) and an in-plane magnet to apply fields up to 0.1T (H_x).

Measurements are perform contacting the sample with probes instead of wire bonding to get access to measure the resistances high-frequency response. The creation of a droplet produces an increase in dc resistance caused by the reversal of magnetization in the nanocontact region as well as a characteristic decrease of the high-frequency peak, on the order of GHz.

Figure 7.8 shows measurements of ac and dc resistance for a current sweep at a fixed applied out-of-plane field of 850 mT and 50 mT of in-plane field. In 7.8A, at low currents (< 12.5 mA) no excitations are detected. Increasing the current value (>12.5 mA) produces a high-frequency peak at ~ 26 GHz associated with the FMR mode with a quality factor of ~500. At a current of 14.9 mA the peak in frequency decreases about 2 GHz and the signal becomes higher in amplitude—with a quality factor up to 2050 (see inset in Fig. 7.8A)—and the dc resistance curve presents an abrupt step increase (see Fig. 7.8C, blue line). All together, these signals are signatures of the nucleation of a droplet.

In the previous section, the droplet nucleation was accompanied by an increment of the low-frequency signal that have been linked to drift resonances.

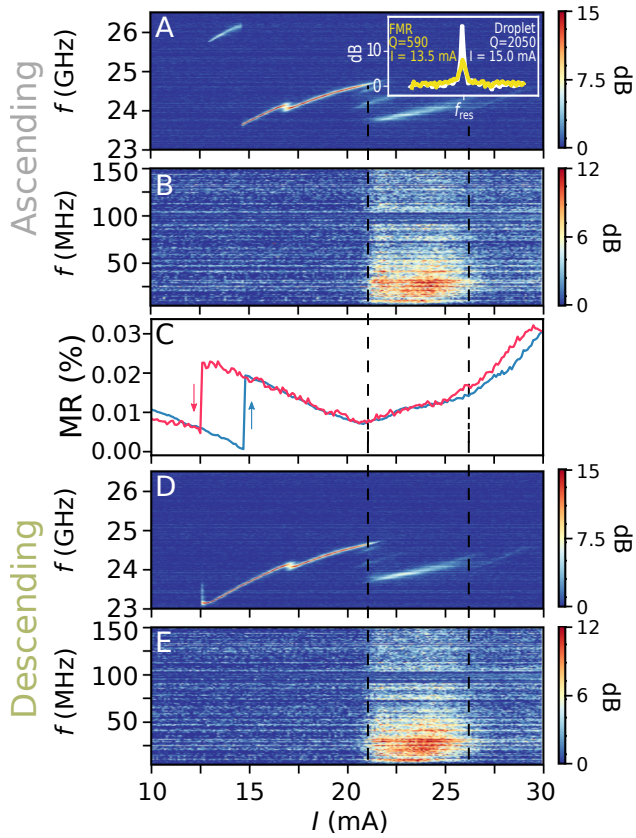

Figure 7.8 **Ascending and descending branches of a current sweep**. High-frequency **(A)** and **(D)** and low-frequency **(B)** and **(E)** and dc **(C)** resistance as a function of the applied current at fixed perpendicular field of 850 mT and in-plane field applied of 50 mT. **(A)** The droplet nucleates at 14.9 mA, where a step in the dc MR is observed (**C**), blue line, together with a decrease of the peak noise frequency by several GHz (**A**). A further increase of current leads to the appearance of multiple droplet modes accompanied by a low-frequency noise **(B)** and changes in trend in the dc MR (**C**). A single parabola is subtracted from the dc MR data. Data on current sweep down can be observed in panels **(D)** and **(E)** , high and low frequency respectively. Red line in panel **(C)** shows the MR for the descending branch showing a small hysteresis that can also be found in panel (**D**). The inset in panel **(A)** shows the spectra for the FMR mode at I = 13.5 mA, red line with a quality factor of 590, and the droplet mode at I = 15 mA, white line with a quality factor of 2090.

However, at low temperature the droplet nucleation does not present this low-frequency peak, characteristic at room temperature. Figure 7.8B plots the low-frequency noise (0 – 150 MHz) in the same range of currents as in Fig. 7.8A.

Between 14.9 and 21 mA the droplet is stable, with a powerful high-frequency peak and no associated low-frequency noise, indicating a more stable droplet state compared with the room temperature measurements. The high-frequency peak has a step down at around 17 mA, which is completely reproducible and reversible (see also Fig. 7.8D and 7.8E for the descending branches of the current sweep). Later on, when the current is higher than 21 mA the situation completely changes. Both three indicators of the droplet state exhibit an abrupt change. The main high-frequency peak splits into three weaker peaks with lower frequencies, the low-frequency noise increase and the MR shows a change in trend. This region with multiple weaker peaks, a quality factor of 320 is measured at $I = 23.2$ mA, extends from to 21 to 26 mA. Increasing the current even more results on a vanish of both high- and low- frequency signal and another change in the trend of the dc resistance, which might be caused partially by an increase in the droplet size: the blue line in Fig. 7.8C shows the dc resistance curve with a parabola subtracted to account for a heating proportional to the square of the applied current (the red curve is the MR for the descending branch).

There is a correlation between ac and dc MR and both measurements show the existence of distinct droplet modes. On the one hand, droplets present a mode with a single and strong high-frequency peak and without low-frequency noise; on the other hand droplets appear as multiple high-frequency peaks and a strong low-frequency noise consistent with superposition between modes. The transition between those two modes is completely reproducible when the current sweeps down as can be seen in Fig. 7.8D and 7.8E, for high and low frequency spectra, respectively.

7.2.1 Effects of the Application of an in-Plane Field

In-plane fields were previously used to introduce asymmetry to the system, which resulted in a shift of the droplet causing drift resonances (the droplet shifts outside of the nanocontact where it dissipates and a new droplet creates beneath the nanocontact). Here, we show that applying a large enough in-plane field not only produces the appearance of drift instabilities—with associated low-frequency noise—but also favors the generation of multiple droplet modes.

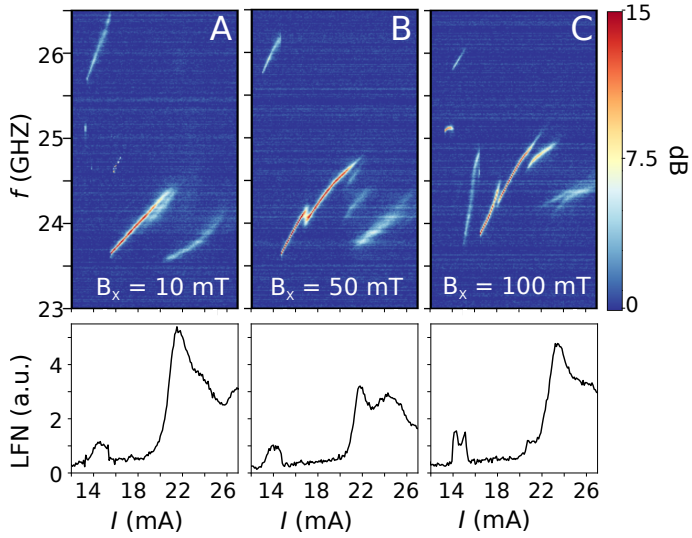

Figure 7.9 **High- and low-frequency response of the droplet at different in-plane field values**. High frequency and integrated low-frequency noise (between 10 MHz and 1 GHz) as a function of the applied current at fixed perpendicular field of 850 mT and at different in-plane fields: in **(A)** 10 mT, in **(B)** 50 mT and in **(C)** 100 mT. A sharp increase of the integrated low-frequency MR is observed at high currents (above 21 mA) when the main droplet mode splits into multiple modes. The in-plane field also promotes the splitting of the main droplet mode at $I = 16$ mA **(B)** and $I = 20$ mA **(C)** .

Figure 7.9 shows the high-frequency and the integrated low-frequency noise (between $10 - 150$ MHz) for the same current sweep shown in Fig. 7.8 under different in-plane fields. The in-plane field splits the single droplet mode into two modes at 17 mA for field values of 50 and 100 mT (Figs. 7.9B and C and again at 20 mA for a field value of 100 mT (Fig. 7.9C. However, there is no low-frequency noise associated with the mode changes. At currents above 21 mA the droplet splits again into a different modes (at ~ 23.5 GHz) with associated low-frequency noise; this time the in-plane field also promotes the appearance of additional modes in between the two modes at $I = 21$ mA in Fig. 7.9A.

The presence of multiple droplet modes is not always associated with low-frequency noise and, conversely, low-frequency noise appears in cases with a single droplet mode. In sum, we found that the effect of in-plane fields when increasing the applied current consists in favoring the splitting of droplet modes with little effect on the modes stability (i.e., no associated low-frequency noise).

The existence of the superposition between modes region also appears at different out-of-plane fields. High frequency data as a function of the applied current at 750 mT out-of-plane field is provided for different in-plane fields in Fig. 7.10[1]. A FMR like signal about 24 GHz is observed at current lowers than 15 mA. Then, at 15 mA, a 3 GHz step decrease indicates the droplet nucleation and the high frequency peak becomes larger. The droplet remains stable until 20 mA where another step decrease is observed accompanied by an increment of the low frequency noise and a decrease of the high frequency signal power, as can be observed at Fig. 7.10D.

The effect of the in-plane field can be observed at Fig. 7.10 in panels B (20 mT), C (50 mT) and D (100 mT). On the one hand, the in-plane field promotes the appearance of superposition between modes just after the nucleation of the droplet, and the stable droplet mode emerges latter, 15 mA without in-plane field and 17.5 mA for a 100 mT of in-plane field. On the other hand, the in-plane field splits the stable droplet mode into two stable modes at 19 mA in panel D.

In conclusion the in-plane fields introduce instability to the system and promotes the appearance of superposition between modes. In general it creates a more complex high frequency spectra landscape.

7.2.2 Out-Of-Plane Field Sweeps

Figures 7.8 and 7.10 show the effects of a current sweep for a fixed out-of-plane field. Now, in order to understand the correlation between multiple droplet modes and low-frequency noise, we studied the effect of variation of the out-of-plane field at fixed current values—constant current-induced Oersted fields. Figure 7.11 shows high frequency spectra, and integrated low-frequency spectra, for out-of-plane magnetic field sweeps at a constant applied current of 18 mA and for different applied in-plane fields. The droplet forms at low out-of-plane fields values ($<$ 300 mT) and the precessing frequency increases as well with the field with a slope of $\sim$ 28 GHz/T, which corresponds to the gyromagnetic ratio ($\gamma/2\pi$), when the value of the field is increased. The integrated low-frequency noise (lower

[1] Resistance curve is not provided because it was too noisy. The fact that we are using probes instead of wire bonding allows to obtain higher frequency data, but at the same time, the contact is less stable and the resistance curve becomes noisy

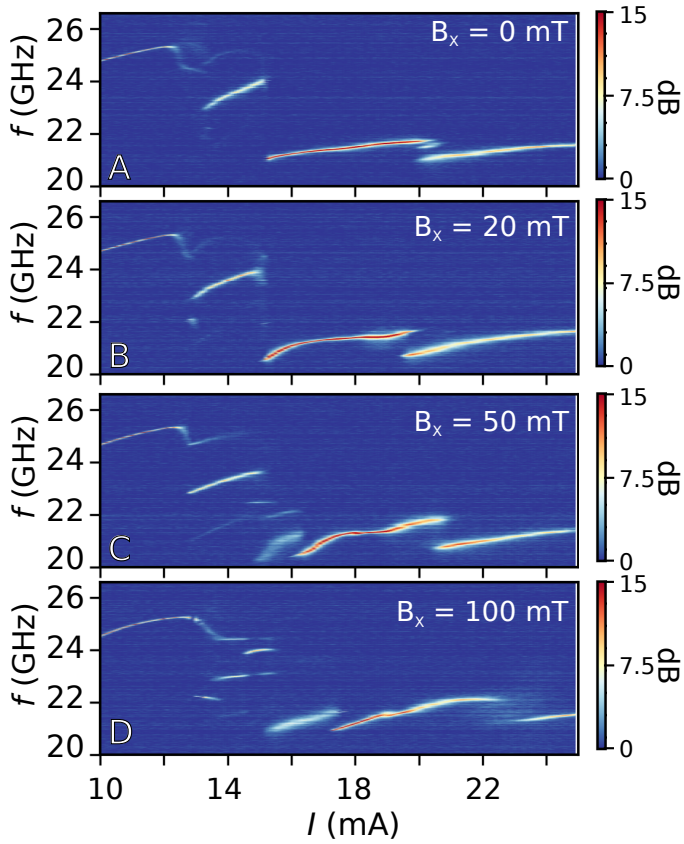

Figure 7.10 **High-frequency spectra for different in-plane fields**. High-frequency spectra as a function of the current for different in-plane field values and fixed out-of-plane field of 750 mT. In-plane fields introduce instability while promoting the appearance of hopping between modes.

panels) indicate that the droplet nucleated at low out-of-plane fields and it is in a non stable state (multiple peaks can be observed for low values of the field). However, by increasing the perpendicular field—and depending on the value of the applied in-plane field—there is a threshold for which the low-frequency noise vanishes and the high-frequency peak becomes stronger, indicating the transition to a stable droplet state. Threshold values are marked with colored lines in Fig. 7.11, which are shifted to higher values of the out-of-plane fields corresponding to the increment of the in-plane field. Quality factors of 2450, 2730 and 1300 are obtained right after the marked field values. Our data indicates that higher fields

tend to stabilize droplet modes in agreement with Wills et al. [83] that predicted that droplet modes would be stable only close to its boundaries of nucleation, which means either at low currents for a given field or at large fields at a fixed current.

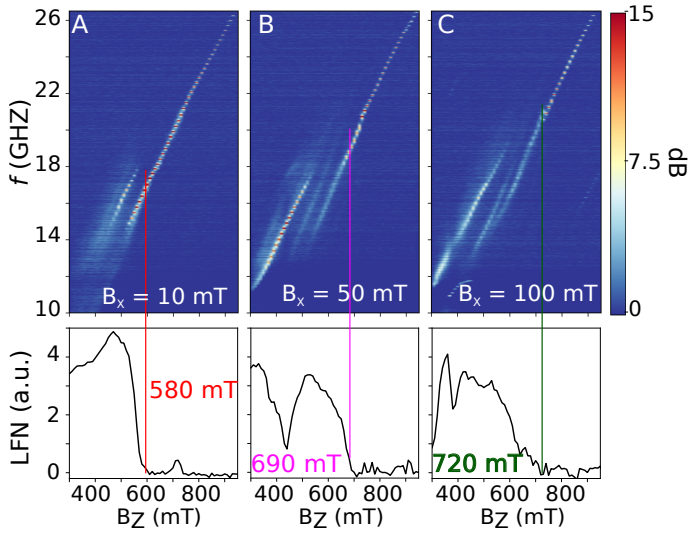

Figure 7.11 **High- and low-frequency spectra as a function of out-of-plane field for different in-plane fields**. High-frequency and integrated low-frequency noise (between 10 MHz and 1 GHz) as a function of the applied field at fixed current of $I = 18$ mA and for different in-plane fields: in **(A)** 10 mT, in **(B)** 50 mT and in **(C)** 100 mT. Multiple droplet modes are present at low applied fields together with low-frequency noise. At field values higher than 580 mT **(A)** , 690 mT **(B)** and 720 mT **(C)** a single peak with high quality factor of 2450, 2730 and 1300 respectively, together with the vanishing low-frequency noise, indicate the stability of the droplet mode.

At this point, and combining the high and low frequency data from both current and field sweeps, we plot a phase diagram of droplet states. Figure 7.12 shows the state of the droplet as a function of the applied current and the out-of-plane magnetic field. Blue squares represent the onset data for the droplet from current sweeps—and the blue line is the onset boundary. Inside the droplet region we can distinguish between stable droplet and superposition-between-droplet-modes regions, marked as red circles (experimental points were the multiple modes with low frequency noise appear). An additional red square is added from

measurements from Fig. 7.11, a field sweep, where the multiple droplet modes disappear.

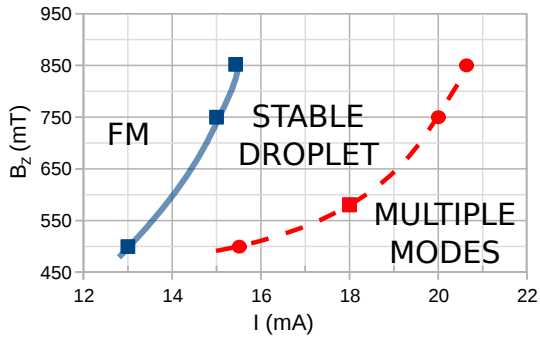

Figure 7.12 **Phase diagram**. Phase diagram of the droplet states for the 100 nm diameter sample. For lower current the droplet can not be excited. Blue squares represent the onset data of the droplet and blue line is the onset boundary. Red circles represent the boundary between the stable droplet state and the multiple hopping modes of the droplet obtained from current sweeps for a fixed values of the out-of-plane field. The red square data point is obtained from a field sweep for a fixed value of the current, 18 mA.

7.2.3 Micromagnetic Modeling

The transition of the droplet from one stable state to another stable state without the appearance of low-frequency noise, as in Fig. 7.8 at 17 mA, as well as the superposition between non-stable modes, as in Fig. 7.8 at 21 mA, are behaviors that can be selected tunning the external parameters as the applied current and the out-of-plane and in-plane fields. It seems to be an energy competition, which results in those different behaviors. In order to investigate this, we have created a toy model to show that a non-uniform energy landscape of the internal applied field of the FL can result in the appearance of discrete droplet modes with slightly different precession frequencies and dimensions, similar to experiments.

Using micromagnetic simulations we define an artificial energy landscape for the out-of-plane applied field consisting of a uniform field perpendicular to the film plane of 850 mT, as in Fig. 7.8, plus a small region of about 35 nm where the applied field decreases smoothly down to 780 mT.

Figure 7.13A shows the magnetization in the perpendicular direction within the nanocontact region for current values of I =13.5, 17.5 and 21.5 mA. Snapshots of the droplet are plotted as insets showing the two different modes. An applied current of 21.5 mA localizes first the droplet mostly beneath the nanocontact with a small shift towards the region where the applied field is smaller. The precession frequency is 24.49 GHz. A much smaller current of 13.5 mA still maintains the droplet mode but now the droplet lies precisely at the region with a smaller field [84, 85]. The precession frequency is now 25.21 GHz. An intermediate applied current of 17.5 mA produces a an oscillation between the two mentioned modes with a frequency of ~230 MHz.

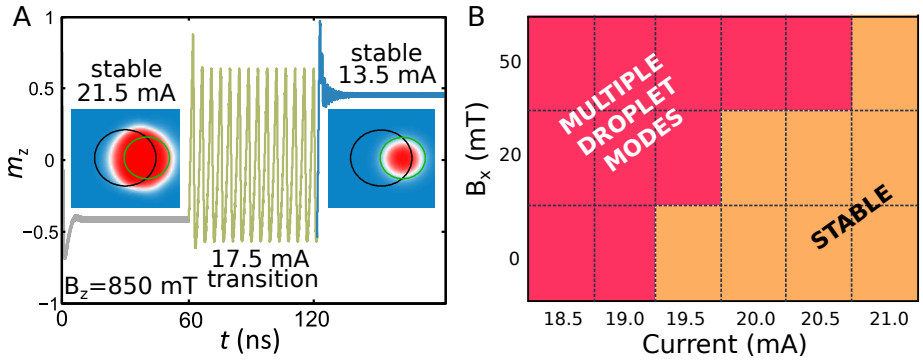

Figure 7.13 **Micromagnetic simulations**. **(A)** Evolution of the magnetization, m_z, under a 100 nm diameter nanocontact for applied currents of I =21.5, 17.5 and 13.5 mA and an applied field perpendicular to the plane of 850 mT. Insets droplet snapshots correspond to the state at I =21.5 mA and I =13.5 mA. The black circle indicates the position of the nanocontact and the green circle indicates the 2σ for the Gaussian function of 50 mT reducing the overall applied field. **(B)** Diagram of the droplet state as a function of the applied current and the in-plane field for a out-of-plane field of 850 mT. For a fixed value of the current, the in-plane can tune the mode of the droplet. For higher values of the in-plane field mode hopping emerges.

Next, we add in-plane fields to the same simulation routine, i.e., we sweep down the applied current from a large value of 21.5 mA and record the moment when the oscillating modes appear. Figure 7.13B shows a phase diagram of the droplet state as a function of the in-plane field and the applied current at a fixed value of the out-of-plane field of 850 mT. At high currents the droplet is stable occupying the full nanocontact (orange region). When the current is lowered,

oscillation between modes occurs—as seen in Fig. 7.13A—and it depends on the applied in-plane field: larger the in-plane field, larger currents for stabilization.

7.3 Conclusions

Low-frequency noise was related with the fact that magnetic solitons move beneath the nanocontact. Signals of instability were observed at room temperature just after the droplet nucleation. The introduction of in-plane fields favored the low-frequency noise response of the sample indicating an increment of the instability. Through simulations, instabilities were related with the movement of the droplet as a whole object. The droplet was driven out of the nanocontact, annihilated because the damping, and created anew.

With measurements at low temperature we studied the effects of in-plane fields on droplet states. In-plane fields can produce a split of a stable droplet state into different stable states as well as the appearance of multiple unstable states. We have observed the existence of different and quantized droplet modes that are accessed by varying applied fields and currents. We found that droplet modes at low currents have a larger high-frequency amplitude and a better quality factor with no associated low-frequency noise.

Chapter 8

Creation and Annihilation Processes of Dissipative Magnetic Solitons

In this chapter we study nucleation and annihilation processes of magnetic solitons combining both experimental results and micromagnetic simulations. We first approach the nucleation process with micromagnetic simulations to investigate the role of the initial magnetization state on the topology of the final soliton state. We also investigate the influence of other parameters such as the external applied field, the current-induced Oersted fields, the temperature, or the velocity of changing the spin-polarized current. Then, we focus on experimental results regarding both nucleation and annihilation processes and we found that they present different time scales. Whereas the annihilation process occurs at the ns timescale, the creation process can take hundreds of ns. Micromagnetic simulations of the experiments reveal that nucleation presents an intrinsic incubation time, which makes it a process much longer than the annihilation (at least two orders of magnitude slower) and depends on the initial magnetization state. Controlling the incubation time we show that both processes can occur at the same timescale.

8.1 Nucleation Process of Magnetic Solitons

We study the nucleation of magnetic solitons in magnetic materials with damping using micromagnetic simulations. We consider a circular nanocontact region, with 100 − 150 nm of diameter, on top of a ferromagnetic thin film with PMA. Current-induced Oersted fields were taken into account whereas temperature, unless indicated, it was not. Parameters of the magnetic material, which were taken from characterization [63, 82], and simulation details can be consulted in Appendix A.

For different values of the spin-polarized current we excite the magnetization beneath the nanocontact. From lower to higher current values we reach a threshold value where STT term compensates the damping. Figure 8.1A shows the frequency of the magnetic excitation, i.e., the frequency of the ac response of the resistance in experiments, on the left Y-axis and the amplitude of the magnetic excitation on the right Y-aixs, blue and red dots respectively, as a function of the current[1]. An FMR mode (∼ 19.5 GHz) is observed for currents below 10 mA whereas for higher values of the current the frequency drops to lower frequencies (∼ 14.6 GHz) and seems to remain at constant frequency for all current values. However, the amplitude of the analyzed peaks reveals a change of the behavior of the nucleated magnetic soliton above 28 mA.

The initial state of the magnetization was arbitrarily chosen as an uniform magnetized state with the magnetization deviated, $\theta_I = 1.5$ deg, from the perpendicular state. Finally, the bottom panel of Fig. 8.1A shows the resultant SN calculated using eq. 6.2, which informs us about the topology of the excited magnetic soliton, which goes from $SN = 0$, for current values below 28 mA, to $SN = 1$. Whereas the drop in the frequency indicates that a magnetic soliton is nucleated, both amplitude of the oscillation and SN value indicate that there is a difference on the excited solitons when the current increases; a non-topological soliton—magnetic droplet—is excited for currents between 10 and 28 mA and a topological soliton, the so called *dynamical skyrmion* (DS)[81], is excited for higher current values. In fact, simulating both droplet and DS for a long period of time and re-calculating

[1]The resonance frequency is calculated performing a fast Fourier transform (FFT) of the X component of the magnetization.

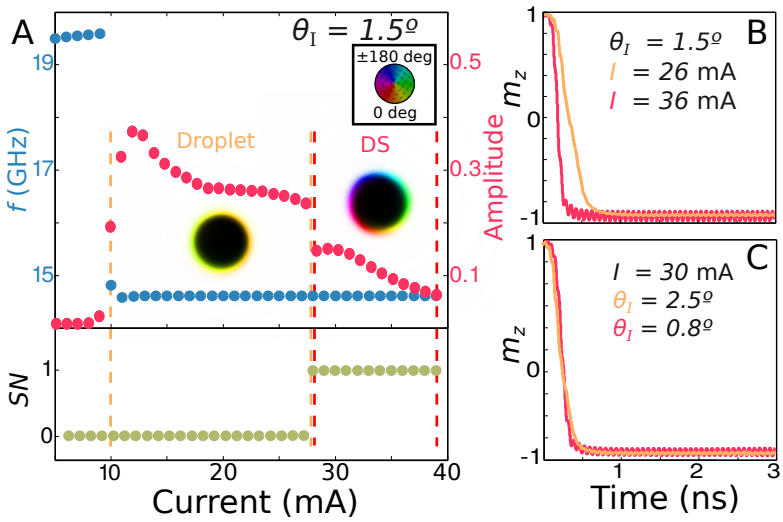

Figure 8.1 **Droplet and dynamical skyrmion creation process**. **(A)** Resonance frequency (in blue dots) and amplitude (red dots) as a function of the applied current for the nanocontact overall magnetization. Both frequency and amplitude correspond to the average over the nanocontact of one of the in-plane components of the magnetization, $m_{x,y}$. The current values are always applied from a same initial magnetization angle in an applied field of 0.5 T and with a polarization of $p = 0.45$. At current values below the threshold (below 10 mA) the nanocontact magnetization precesses close to the ferromagnetic resonance frequency with a small amplitude. A first current threshold at 10 mA corresponds to a droplet formation and shows a much larger amplitude (red curve) and a frequency jump down to a lower value—that remains almost constant with increasing the applied current. A second current threshold at 28 mA corresponds to the DS formation and has a similar precession frequency and a smaller amplitude. The bottom panel show the skyrmion number, S, at each current step. **(B)** and **(C)** time evolution of the normalized magnetization inside the NC for droplet (yellow line) and DS (red line) for the same external applied field of 0.5 T. In **(B)** both solitons are excited at an initial magnetization angle, $\theta_I = 1.5$ deg but using different applied currents. In **(C)** both solitons are exited at 30 mA but changing the initial magnetization angle.

the resonance frequency, a small difference is detected. Whereas the droplet state has a resonance frequency of 14.60 GHz, the DS oscillate at 14.58 GHz.

Topological solitons, $SN > 0$, were predicted to exist as a solutions of the non-dissipative LLG equation [67]. In particular, the $SN = 1$ magnetic soliton was predicted by Zhou et al. using micromagnetic simulations [81]. They consider a PMA material with Dzyaloshinskii-Moriya interaction [86, 87] (DMI) and very large current values, more than 5 times of the current density that can be applied

in an experiment, on their simulation. However, as we show in Fig. 8.1, neither DMI or high current values are strictly necessary since the DS can be nucleated in a experimental setup similar to the experimental setup used in the droplet nucleation, just by controlling the initial magnetization state.

Figure 8.1A provides us both droplet and DS current thresholds for the chosen initial condition. Since the droplet and DS are topologically different the simulation routine does not consider a continuous current sweep, instead of that, any data point in Fig. 8.1A is simulated starting at the initial condition and left it to evolve for 10 ns. Otherwise, since the droplet nucleates before DS and due to the topology, we would never be able to nucleate a DS. Moreover, it is important to remark that in the simulations the current is applied instantaneously—the role of the ramping currents—is investigated later on this chapter.

Next, we investigate the role of the initial magnetization state in order study the effect on the topology of the final soliton state. Panels B and C of Fig. 8.1 show the time evolution of the magnetization in the nanocontact region of a droplet (yellow) and DS (red). For panel B the θ_I was fixed and we need two different currents to nucleate different solitons, as in panel A, whereas in panel C the current was fixed and it was necessary to change the θ_I to obtain different solitons. We observe that small values of the θ_I, i.e., initial magnetization closer to a perpendicular state, result in the nucleation of a DS. Moreover, Fig. 8.1B and C show that higher applied currents have a faster magnetization reversal, which is something that occurs no matter whether the final state is a droplet or a DS and is caused by a larger STT effect—which is proportional to the applied current [6]. In addition, the DS (red line) presents a larger oscillation of the magnetization indicating there is a breathing of the localized object at the precession frequency.

Figure 8.2 shows the phase diagram of droplet and DS formation as a function of the applied current and the initial magnetization angle, θ_I. The threshold for droplet formation is independent of the initial magnetization state, blue dots; different initial states cause the process of droplet formation to become faster or slower as we will show in next section. On the other hand, the threshold for DS formation, red dots, has a strong dependence on the initial magnetization angle, increasing with larger angles.

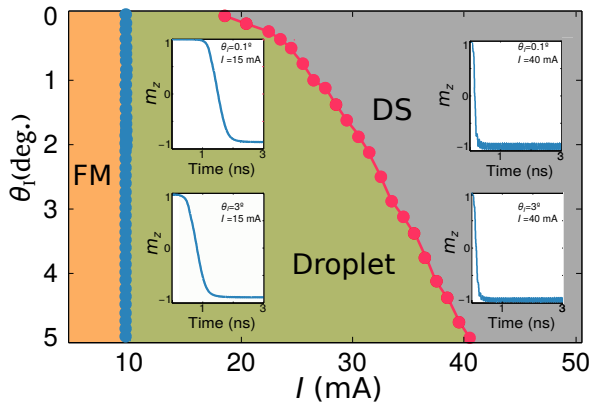

Figure 8.2 **Phase diagram of the droplet and DS formation**. Creation of both solitonic modes as a function of the applied current, I (with polarization $p = 0.45$), and the initial magnetization angle, θ_I. For currents below 10 mA neither droplet nor DS can be excited, orange region. When the current is higher than 10 mA a droplet is excited and droplet's threshold current does not depend on θ_I, green region. If the current is further increased, DS are created, grey region. The current threshold for DS (red line) is higher than the droplet and depends on the initial magnetization state, θ_I. Insets correspond to time evolution curves of nanocontact magnetization at different conditions.

8.1.1 The Role of Nanocontact Size and Current Polarization

DS nucleation threshold is sensitive to the change of others parameter like nanocontact size or polarization of the current. The nanocontact diameter determines the net current required to nucleate solitonic modes whereas a higher value for the polarization increases the STT effect, so it reduces the current needed to nucleate solitonic modes. Droplet and DS thresholds were recomputed for small nanocontacts with diameters of 50 and 100 nm, see Fig. 8.3A, and we obtained values of 4 and 6 mA for the droplet threshold, which represents a decrease of 3 and 5 mA with respect to the diameter of 150 nm presented in Fig. 8.2. However, the DS thresholds does not scale exactly with the current density since the Oersted fields associated with the currents depend on the contact size. Larger reduction of 5 and 9 mA for the DS formation were also observed. We computed the same phase diagram of Fig. 8.2 but considering a different value for the polarization. Figure 8.3b shows both droplet and DS thresholds for polarization of $p = 0.45$ (as Fig. 8.2) and $p = 0.6$. The change in the polarization produces a shift of 2 mA in the droplet threshold and a shift of 5 mA in the DS threshold.

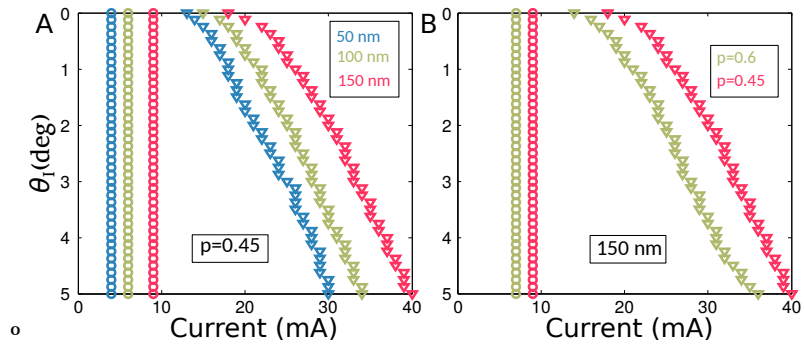

Figure 8.3 **Phase diagrams of the droplet and DS formation as a function of NC diameter and polarization.** **(A)** Creation of droplet and DS as a function of applied current for nanocontact diameters of 50, 100, and 150 nm for a fixed current polarization of 0.45. **(B)** Creation of droplet and DS as a function of applied current for current polarizations of 0.45 and 0.6 at a fixed nanocontact diameter of 150 nm.

In the simulations, two main effects are involved in the magnetization dynamics when a spin-polarized current flows through a nanocontact to a magnetic film. On the one hand, a spin-polarized current of the appropriate polarity interacts with the magnetization via the STT effect trying to align the magnetization in the opposite direction. The STT effect, Section 6.1.2, is proportional to the quantity of magnetization that is not aligned with the polarizer. On the other hand, the electrical current flowing through the nanocontact causes Oersted fields that may curl the magnetization. Here we note that in absence of other effects the magnetization of a PMA layer adopts a configuration with $SN = 1$ in presence of Oersted fields. Whereas polarization of the current affect directly to the value of the STT interaction, the current modify both the value of the STT interaction and the Oersted fields. In Fig. 8.2, where the soliton state was studied as a function of the applied current both STT and Oersted fields were changing. However, we are interested in how STT and Oersted fields interact individually. For this reason we calculate new phase diagrams where the applied current remains fixed at $I = 30$ mA. The first phase diagram sweeps on the value of the polarization of this current, Fig. 8.4, and in the second case we sweep the value of the Oersted fields, Fig. 8.5.

The Oersted-field effects are fixed in Fig. 8.4 and only STT effects vary with spin-polarization. For small polarization values there is a small STT effect and it is no able to compensate the damping, then, no excitations are presented independently

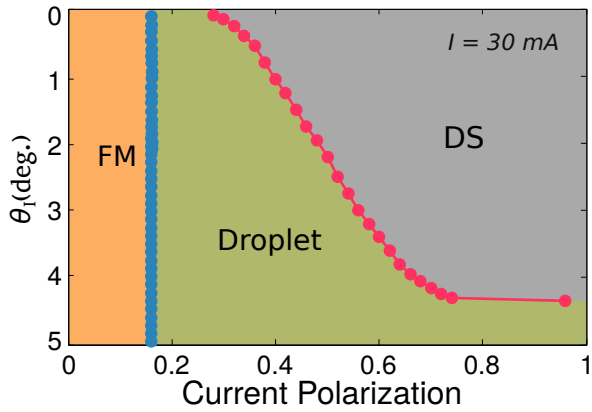

Figure 8.4 **Phase diagram of the droplet and DS formation.** Creation of both solitonic modes as a function of the polarization of the applied current and the initial magnetization angle (θ_{I}) for a fixed current of 30 mA. As the current is fixed the Oersted field effects are fixed and only spin-transfer torque (STT) effects vary with spin-polarization.

of the initial magnetization angle. As the current polarization increases we found first the onset of droplet state and with a further increase, the onset of DS. Again, in this situation, the droplet threshold does not depend on the initial state whereas the DS has a strong dependence requiring larger values of polarization at larger angles of the initial magnetization angle, θ_{I}. For angles higher than 4.5 deg, just a droplet can be excited since the Oersted fields, which are fixed, can not create the vorticity in the magnetization before the STT switches it.

In Fig. 8.5 the current and its polarization are fixed and just the value of the Oersted field is swept. We observe that droplets do not need Oersted fields to be excited and DS need, at least, considering the almost perpendicular situation, a minimum Oersted field (the Oersted field created for a current of 5 mA) what is telling us that Oersted fields are crucial for their excitation.

In general, then nucleation process of solitonic modes involves a competition between the Oersted fields and STT effects. The STT effect increases rapidly as the magnetization tilts from the perpendicular state, $\theta_I = 0$ deg. As we are going to show in next section, there is an incubation time for the nucleation of a droplet and during this incubation time the Oersted field effect plays an important role for the DS nucleation. For higher enough current values, the DS threshold, the Oersted field becomes larger and they create a vorticity in the magnetization during the

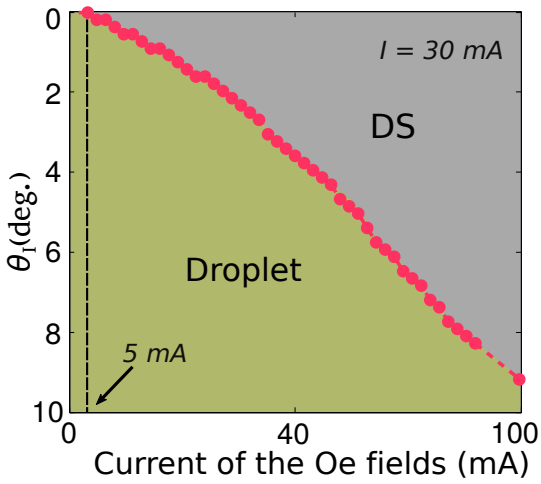

Figure 8.5 **Phase diagram of the droplet and DS formation.** Creation of both solitonic modes as a function of the current of the Oersted fields and the initial magnetization angle (θ_I) for a fixed current of 30 mA.

incubation time before the STT effect can switch it. Then, once the magnetization adopts the Oersted fields topology, $SN = 1$, the magnetization switches down driven by the STT forming a DS. If the incubation time is not so long or the Oersted fields are not so large a droplet forms.

Figure 8.5 highlights the importance of the Oersted fields in the DS nucleation processes. In fact, DS present SN=1 since the induce Oersted fields vorticity has a SN=1. If the induced fields presented higher topological orders the DS would also exhibit such a topology. Figure 8.6 shows the magnetization distribution for the case of a droplet, a DS and a magnetic soliton with $SN = 2$. For their nucleation, we artificially change the current-induce Oersted fields for a field distribution with $SN = 2$.

8.1.2 The Effect of the Out-Of-Plane Field

Out-of-plane fields are required, as we describe in Section 6.3, to tilt the magnetization of the PL, which is the responsible of the polarization of the current. Larger values of the out-of-plane fields require larger current for soliton formation. We have studied the effect on the droplet and DS thresholds in a range of applied fields between 0 and 2 T (experimentally the PL, Py, should saturate at ≈1.1 T).

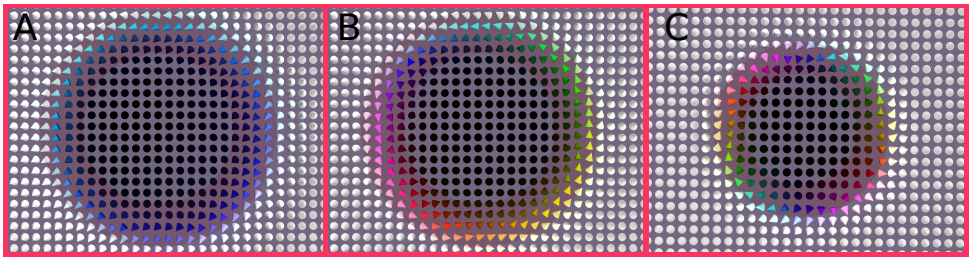

Figure 8.6 **Images of magnetic solitons.** Droplet (**A**), DS (**B**) and magnetic soliton with $SN = 2$ (**C**) created without Oersted fields, with normal Oersted fields and using an artificially field distribution with $SN = 2$, respectively.

We considered an initial magnetization state corresponding to $\theta_I = 0.5$ deg and repeated the procedure to obtain Fig. 8.2. We plot in Fig. 8.7 threshold currents as a function of the applied field for both droplet and DS. We can see that both current thresholds increase equally (and linearly) with the applied field.

One would expect an increase of the STT threshold with applied field proportional to the damping factor [63], $\sigma_0 = h\alpha$, where α is the damping factor, h the applied field (normalized to the magnetization saturation, M_s). The STT variable, $\sigma_0 = I/I_0$, is proportional to the current intensity, I, with

$$I_0 = \frac{2\mu_0 M_s^2 e\pi r_c^2 \delta}{\hbar\epsilon}, \tag{8.1}$$

r_c being the radius of the point contact, δ the film thickness, ϵ the spin-torque efficiency, $\hbar$ Planck's constant and e the electron charge.

If we consider a spin torque efficiency, ϵ, of 0.45 (our spin polarization) we obtained that the slope of the curve I vs H is 7.5 mA/T, which matches well with our simulations. What is remarkable here is that the threshold for DS follows exactly a same trend with the applied field.

8.1.3 The Effect of the Ramping Current

Simulations routines used to calculate diagrams of Figs. 8.2, 8.4 and 8.3 were done with sharp steps of current or polarization. However, the velocity of changing spin-polarized current plays a key role in defining whether a droplet or a DS forms. Figure 8.8 shows a comparison between a current ramp of 100 ps and 1 ns

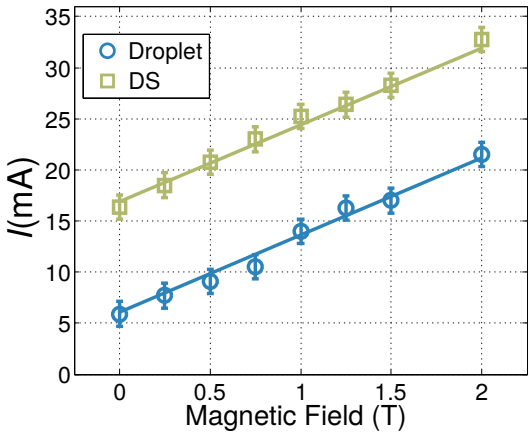

Figure 8.7 **Threshold currents as a function of the applied field.** The initial magnetization was kept constant ($\theta_I = 0.5$ deg) for all different values of the perpendicular magnetic field. Thresholds for both droplet in blue circles and DS in green squares are plotted.

with identical initial conditions showing the formation of DS and droplet states respectively.

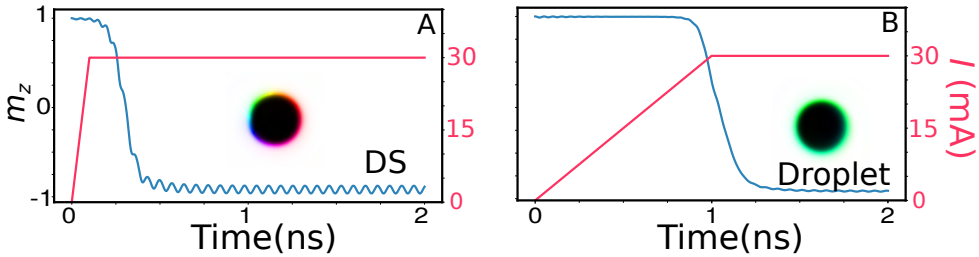

Figure 8.8 **Ramping current pulses.** Time evolution of the normalized magnetization inside the NC (in blue) for a ramping current between 0 and 30 mA for two different times: In **(A)** it takes 100 ps and a DS forms and in **(B)** the ramp takes 1 ns and a droplet forms. The initial condition is the same for both panels and corresponds to an angle of 0.5 deg. The rest of the parameters are the same as in Fig. 8.2.

We observed that slow ramping currents suppress the formation of DS in favor of droplets. When the timescale of the droplet incubation time is similar to the current ramp duration then a droplet nucleates, however, for current ramps faster than the incubation time a DS forms.

8.1.4 The Effect of the Temperature

Experimental detection of DS will imply to take into account of temperature effects. The temperature should modify the initial magnetization state—a temperature of 300 K provides a fluctuation of spins larger than $\theta = 10$ deg for our studied configuration. However, the effect of temperature cannot be compared directly to the studied cases in Fig. 8.2 because temperature also provides fluctuations of spins during the creation process. Figure 8.9 shows a new phase diagram of the droplet and DS nucleation as a function of the temperature and the applied current where the initial magnetization state is defined by the temperature. We found that droplet threshold does not change when temperature is considered. However, the DS threshold increases with temperature.

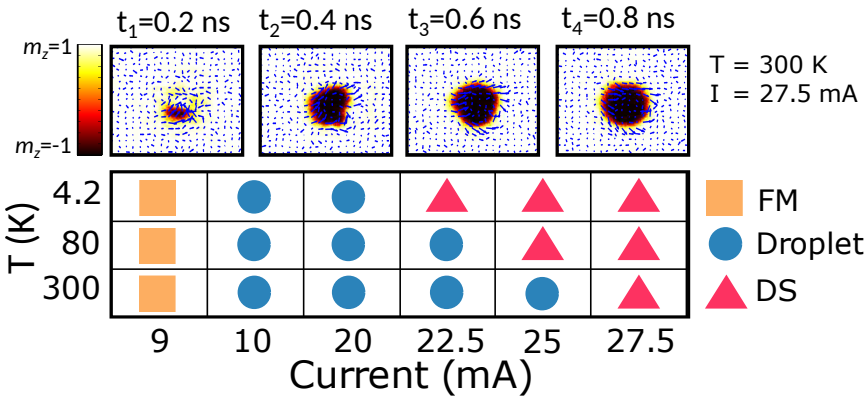

Figure 8.9 **Phase diagram of the droplet and DS formation.** The initial condition is here obtained after magnetic relaxation at a given temperature in presence of an applied field of 0.5 T. Top panels show the evolution of magnetization (m_z in colorscale and m_x and m_y with vector arrows) for a $T = 300$ K and a current of $I = 27.5$ mA a dynamical skryrmion formed. For currents below 10 mA neither droplet nor DS can be excited at any temperature, orange squares. When the current is higher than 10 mA a droplet is excited and the droplet's threshold current does not depend on temperature, blue circles. If the current is further increased, DS are created, red circles, at a different currents for each temperature.

8.1.5 Stability Study for Magnetic Dynamical Skyrmions

DS is a topological version of a droplet, which leaves similar traces in the high-frequency spectra as well as in dc resistances measurements. Both solitons also exhibit magnetic bistability over considerable ranges of applied current and magnetic field [4, 6, 62, 63, 78, 79, 81, 88–90]. However, they present different behavior in front of instabilities such as the reduction of the applied current or the introduction of in-plane fields. Now, we discuss about the differences in the stability between droplet and DS, which is more stable due the so called *topological protection* [81]. The difference in the stability against asymmetries of both magnetic solitons shows us a experimental way to distinguish between them.

Differences in the Bistability Regions of Both Solitons

We firsts investigate the conditions that produce the annihilation of the solitonic modes when a lower degree of spin-transfer torque—a lower current—is applied. Figure 8.10 shows two curves corresponding to the average magnetization within the NC, m_z, as the applied current decreases from an initial value of $I = 30$ mA. In Section 8.1 we show that droplet and DS can be nucleated at the same current just tunning the initial magnetization state, which is controlled either by the angle that the initial magnetization deviate from perpendicular or the relaxing initial time before the application of the spin-polarized current (simulations in Section 8.2). Using $\theta_{\mathrm{I}} = 3$ deg and $\theta_{\mathrm{I}} = 0.1$ deg a droplet and a DS are nucleated respectively at 30 mA and considering a polarization factor of 0.45. Once both solitons are nucleated the current is reduced to observe how solitons are annihilated by damping. When the current arrives to 9 mA the droplet collapses (red curve), however, the DS requires a much lower current value to be annihilated (blue curve). Only when the current is lower that 4 mA the DS vanishes revealing that the DS remains stable over a larger range of applied currents or in other words, the DS requires smaller current values to be sustained.

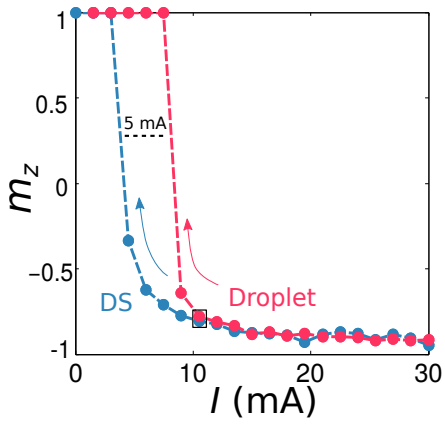

Figure 8.10 **Bistability of Droplet and DS**. Curves of annihilation of droplet (red line) and DS (blue line) with decreasing the applied current. The curves correspond to the averaged normalized magnetization within the nanocontact, m_z, as the applied current decreases from an initial value of $I = 30$ mA. Both droplet and a DS are created at 30 mA (using $\theta_I = 3$ deg and $\theta_I = 0.1$ deg respectively). The droplet collapses at about 9 mA whereas the DS does it at a lower current of about 4 mA.

DS Response to an In-Plane Field

Next, as we did for droplets in Section 7, we investigate the effect of a magnetic field gradient in the NC. Experiments revealed that the low frequency noise in droplets [4, 89, 91] is associated with a periodic process of shifting, annihilation, and creation and simulations showed that an asymmetry of the effective field causes a drift instability resulting in an oscillatory signal of hundreds of MHz—drift resonances.

We excite droplet and DS states at 30 mA using different initial states (same as in Fig. 8.10 and after a stabilization period of 5 ns we reduce the applied current until 10 mA, black squares in Fig. 8.10. The current reduction drive both solitons to a more unstable situation, droplet can not be sustained with lower current. Then, a small in-plane field of 50 mT is applied. The in-plane field ends up destabilizing the solitonic modes. The combination of a fixed in-plane field with the Oersted fields creates an in-plane field gradient in the nanocontact. Figure 8.11 shows the time evolution of the magnetization for a droplet (red line) and a DS (blue line). The small in-plane applied field causes a shift of the droplet away from the NC followed by a re-nucleation of a droplet state. The process of creation and

annihilation is repeated at a frequency in the MHz range (~ 80 MHz), similar to simulations performed in Section 7 [4]. The effect of an in-plane field to the DS is different; DS has an initial change as a result of the abrupt change of the magnetic field but later on, the DS stabilizes again.

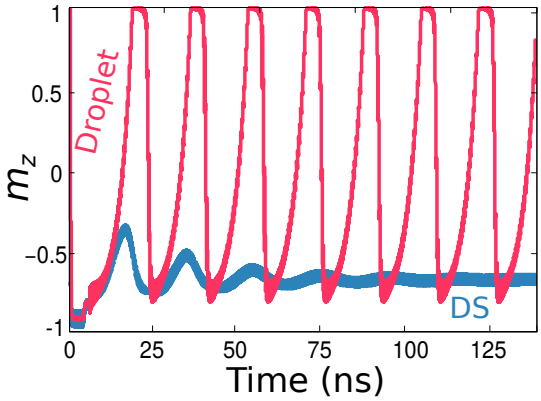

Figure 8.11 **Drift instabilities**. Time evolution of m_z for a droplet (red line) and a DS (blue line) in the presence of an in-plane magnetic field. Both droplet and DS states are created at 30 mA using different initial states (same as in a)) and after stabilization the applied current is reduced to 10 mA, black squares in a), and a small in-plane field of 50 mT is applied. The magnetization of droplet and DS behaves completely differently; the droplet's magnetization oscillates caused by a drift resonance (~ 40 MHz) while the DS's magnetization, although it initially oscillates, it stabilizes after ~ 80 ns and remains with the initial topology having $S = 1$.

The behavior of DS in front of a reduction of the applied current and the introduction of an asymmetry with in-plane fields indicates that DS are more robust against perturbation. Moreover, those differences with its non-topological analogue allows us to design an experimental process to distinguish between them. Here, based on simulations presented in Fig. 8.10 and Fig. 8.11 we claim that, if a topological soliton can be nucleated beneath the NC, a study like the one done in Chapter 7 for droplet where in-plane fields were applied while the low-frequency response were registered can determine that the nucleated soliton is not a droplet. This, together with the fact that the histeretic region should be slightly different may be a prove for the experimental observation of DS in PMA materials without DMI.

8.1.6 Experimental Speculation for DS

We, thus, speculate about the possibility of observing DS experimentally in a experimental setup similar to one used for the study of droplets (see Section 6.3)[4, 62, 63, 78, 79, 88, 89, 92]. Recently, Liu et al.[90] present an experimental observation of a solitonic mode modulation that could indicate the existence of a DS. So far, the existence of DS has been associated to the DMI present in some magnetic films [81, 90].

In order to nucleate a DS instead of a droplet we propose different approaches. On the one hand, large out-of-plane fields can be used to obtain an initial magnetization state close to all perpendicular. Moreover, low temperatures can be used to reduce the thermal noise that might produce fluctuations of the magnetization. It could be that experiments performed at low temperatures and large fields [63, 91] have already created DS.

On the other hand, we can provide a large current that is not polarized, producing large Oersted fields but no STT effect. Then, the current polarization has to increase so that the STT becomes predominant and promotes the creation of a solitonic mode. If the magnetization was already curled due to the Oersted fields it could result in the creation of a solitonic mode with topological protection: a DS.

This later realization is feasible by using a perpendicular polarizer [92] with appropriate coercivity so that it switches at a field that can create the DS. One could then apply a constant current to the nanocontact while the magnetic field sweeps, the perpendicular polarizer would then switch and create an abrupt change in the spin-polarization of the applied current while maintaining the Oersted fields. Figure 8.12 shows a simulation where we depart from an equilibrium configuration consisting of having an applied current of 30 mA with no polarization and then changing the polarization to a given value. Low polarizations (below 0.16) results in no solitonic excitation. However, at 0.16 the droplet threshold is found whereas the DS formation requires 0.26. The results are similar to what we obtained with increasing current with a fixed polarization but here we always depart from an initial equilibrium configuration. DS can be create at certain values of the polarization with no need of an artificial canted initial magnetization state—the Oersted fields

associated to the electrical current with no spin-polarization provide an initial magnetization state with $\theta_I \neq 0$.

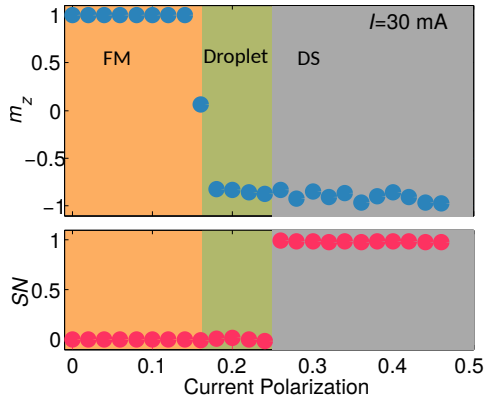

Figure 8.12 **Droplet and dynamical skyrmion creation process**. The upper panel shows the averaged nanocontact magnetization as a function of the current polarization and the lower panel shows the corresponding skyrmion number, $SN >$, of the magnetization configuration. A constant current of 30 mA is applied from the beginning for a few ns to allow magnetization relax before a change in polarization is applied. As the polarization increases we cross a first threshold at 0.16 that corresponds to the creation of a droplet. A further increase of polarization creates a DS (above 0.26).

It is necessary however to distinguish experimentally the two solitonic modes once they are created. The differences in precession frequency, ~20 MHz, is to small to serve as a signature of droplet or DS. Instead, studying the stability of the solitonic modes is the best option. One could study the hysteretic response or the response to small in-plane fields and the appearance of low frequency noise as will be shown in next chapter.

8.2 Experiments on Nucleation and Annihilation of Magnetic Solitons

The knowledge about the required time to nucleate or annihilate a droplet soliton, as well as those processes by themselves are crucial towards technological applications. However, experiments only investigated the steady-state of droplet solitons, i.e., their properties when the current was applied for a long period of time com-

pared to their intrinsic dynamics. In this section we determine the current pulse amplitude and duration needed to generate and annihilate a droplet soliton.

Figure 8.13A shows a phase diagram of the nucleated droplet state where it can be identified three different regions for three different states of the magnetization beneath the nanocontact. Considering a fixed out-of-plane magnetic field two critical currents are observed: I_{c1} (green line), below which the droplet state do not form and I_{c2} ($> I_{c1}$) (blue line) above which there is always a droplet state. Between the two critical currents a hysteretic response is observed.

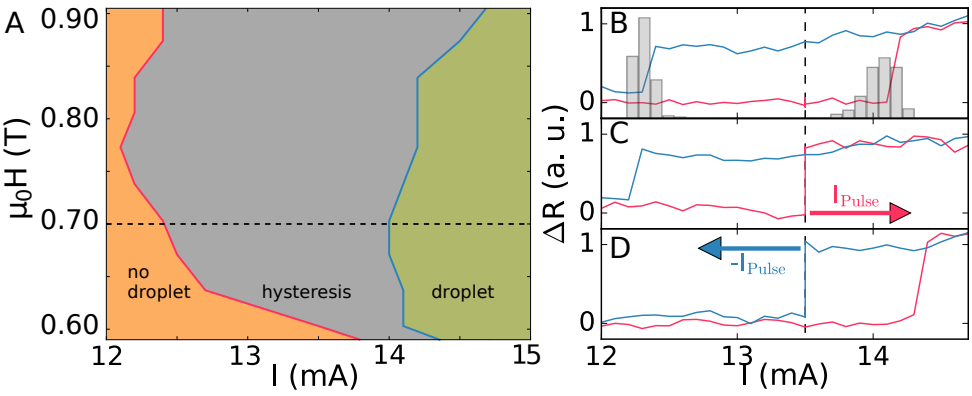

Figure 8.13 **Phase diagram and resistance measurements**. **(A)** Stability field-current map of the droplet. For a fixed perpendicular field the droplet present an hysteretic region, (blue region). **(B)** Resistance vs. current at a fixed field of 0.7 T after subtracting a background caused by Joule heating. The overlaid histogram indicates the distribution of generation and annihilation currents. **(C)** Starting in the non-droplet state a positive current pulse can generate the droplet, as seen by the step increase in nanocontact resistance. **(D)** The nanocontact is biased at 13.5 mA in the higher resistance state (dashed line). A negative current pulse annihilates the droplet, as seen by the step decrease in nanocontact resistance.

Figure 8.13B shows the nanocontact resistance at a fixed out-of-plane field of 0.7 T, horizontal dash line in Fig. 8.13A. At this external field the current sweep was measured 50 times allowing us to obtain statistics about the critical currents. Ramping the current up (red curve) we find $I_{c2} = 14.2 \pm 0.14$ mA whereas ramping the current down (blue curve) $I_{c1} = 12.3 \pm 0.07$ mA, been I_{c1} and I_{c2} the critical currents for the annihilation and creation respectively, and the bound for the

bistability region. Overlaid on Fig. 8.13A, distributions of I_{c1} and I_{c2} are shown as histograms. A higher stochasticity is present in the nucleation process since its standard deviation is twice of the annihilation process.

To study separately both nucleation and annihilation processes we apply current pulses of different amplitude and duration. We choose a value for the current, $I_{c1} < I < I_{c2}$, that is inside the bistability region where both droplet and non-droplet states are achievable at the same current value. Pulses for the nucleation, starting in a non-droplet state, should increase the current value whereas pulses for the annihilation, starting in a droplet state, should reduce the current value. Whether the current pulse is enough to nucleate or annihilate the droplet, then, the new state, droplet or non-droplet, will be stable when the pulse is finished due to the bistability at the chosen current. Figure 8.13C and 8.13D show MR curves for nucleation and annihilation from a intermediate current value of 13.5 mA.

Repeating these measurements for different amplitudes of the pulse a probability of nucleation and annihilation can be calculated as function of the duration of the pulse. Figure 8.14A shows the probability of a droplet annihilation as a function of the pulse duration for different pulse amplitudes whereas Fig. 8.14B shows the probability of a droplet nucleation. Results for both nucleation and annihilation indicate that the critical pulse duration (where probability ~ 50%) is reduced by increasing the amplitude of the current amplitude and that a monotonic increase of the probability is observed with the pulse duration. We find that timescales of the pulse duration for both processes are different. The annihilation occurs in the nanosecond scale whereas nucleation in the microsecond scale. For a pulse amplitude of 3.15 mA applied from a droplet state, the probability to annihilate it reaches almost a 100% with a 2 ns pulse duration whereas with the same amplitude the nucleation reaches only 50% for pulses of 70 ns and need more than 500 ns to reach the 75% of the probability.

8.2.1 Micromagnetic Simulations

In this section we model our system with micromagnetic simulations. Parameters were taken from characterization of the sample [82] and simulation details can be consulted at Appendix A.

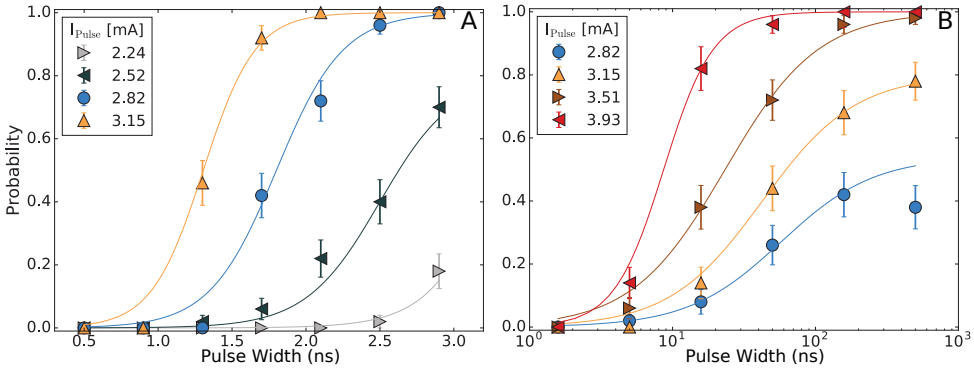

Figure 8.14 **Probability of annihilation and nucleation**. **(A)** The annihilation probability versus pulse duration at different pulse amplitudes. Pulses were added to a dc current of 13.5 mA and a 0.7 T field was applied. The lines are guides to the eye. **(B)** The generation probability versus pulse duration for different pulse amplitudes. The dc current was fixed at 13.5mA and a 0.7 T field was applied. The lines are guides to the eye.

To recreate the experimental conditions we have to find the hysteresis region first. The simulated hysteresis is shown in Fig. 8.15, which shows the average z-component of magnetization in the nanocontact, m_z, as a function of the applied current.

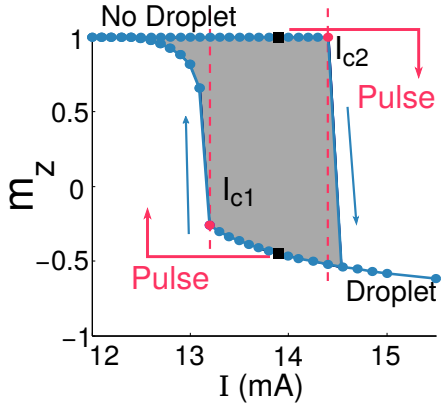

Figure 8.15 **Simulated hysteresis region**. Average magnetization of the nanocontact as a function of the current and the resulting hysteresis: $I_{c1} = 13.1$ mA and $I_{c2} = 14.5$ mA and between these currents both droplet and non-droplet states are stable. Black squares represent the initial current for the application of the pulses, 13.8 mA.

Simulations consider an out-of-plane field of 0.7 T as in experiments. The initial current for the pulses is 13.8 mA, which is in the middle of the bistability region (black squares in Fig. 8.15), and a simulation of the nucleation and the annihilation are shown in Fig. 8.16. Panel B shows the time evolution of the magnetization of the nanocontact in the annihilation process, left panel, and for the generation process, right panel whereas panel C shows the applied current as a function of time. In the annihilation process we excite a droplet and then, a negative polarity pulse of −1.7 mA is applied to a dc current of 13.8 mA. The pulse needed to annihilate the droplet state is of 1.3 ns. On the other hand, in the nucleation process, starting in a non-droplet state, a positive polarity pulse of 1.7 mA is applied. Under these conditions it takes 21 ns to create a droplet. After 21 ns the current is reduced to the initial value, 13.8 mA, and this current sustains the droplet. We thus see that for the same pulse amplitude the generation and annihilation processes occur on different time scales. We observe that the generation process has a waiting time and after that time the droplet forms rapidly, in a transition time of just nanoseconds, 20 % to 80% of the initial to final m_z. The 2D images in Fig. 8.16A show the magnetization at different times in the annihilation and the generation processes where the blue ring represents the NC region.

The final state of the generation process and the initial ($m_z \approx 0.8$) state in annihilation process ($m_z \approx 0.45$) are not the same, as after some time the droplet moves in the nanocontact and the spins at the boundary of the droplet dephase. Figure 8.17 shows the time evolution of the magnetization inside the nanocontact region during the dephasing process. The droplet is exited with at 18 mA and after the nucleation the current is reduced until 14 mA, which should sustain the droplet since is a value inside the bistability region. The magnetization is diminished after the reduction of the current due to a change in the size of the droplet, which becomes smaller, remain in a stable droplet state. However, after a few ns the new droplet state becomes unstable and starts to oscillate around the NC. The dephase leads to displacement of the droplet from the nanocontact region, similar to those reported in Ref. [62]. Once displaced, the droplet rotates around the nanocontact region with a frequency in the kHz range. The magnetization seems to be again

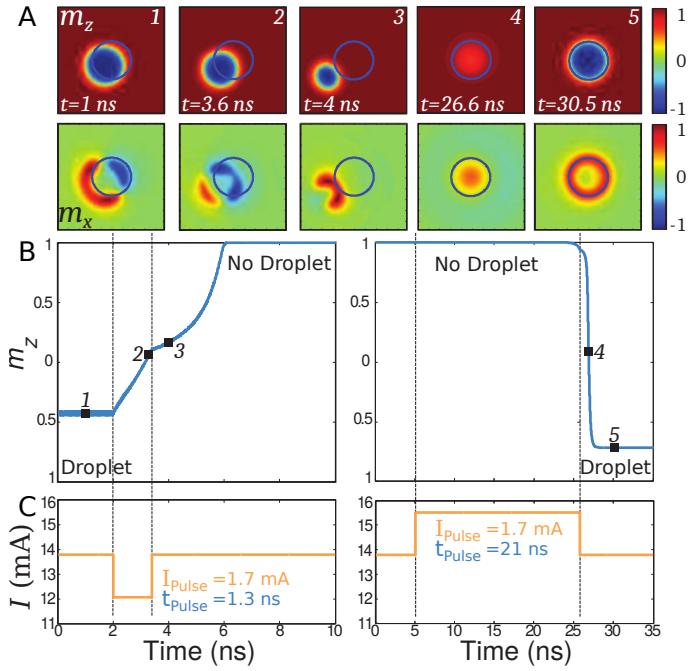

Figure 8.16 **Creation and annihilation process.** **(A)** images of the magnetization at times in the simulation. Images correspond to a 290×290 nm^2 field of view. The blue circle shows the boundary of the nanocontact. **(B)** Time evolution of the nanocontact magnetization for the annihilation and the creation processes, left and right images, respectively. The black squares correspond to the time shown in the images. **(C)** Current applied as a function of time for the annihilation and generation processes. The vertical dashed black lines show the time where the pulse was applied.

reduced, however, this time it is because of the droplet is slightly out of the NC and the m_z is an average of the magnetization inside the NC.

Even though generation and annihilation present different time scales, a long droplet generation time is not fundamental. We found that the droplet generation occurs always in a short time, in the ns timescale, but it is preceded by an incubation time which strongly depends on the initial state of the magnetization in the FL. This incubation time can be understood as the required time to building up spin precession angle starting from a small initial angle [93, 94]. A pathway to control the initial magnetization state of FL is considering the relaxation time, the time between the application of the initial current and the pulse, as a parameter. Then, we can simulate the same current pulse starting at different relaxing times.

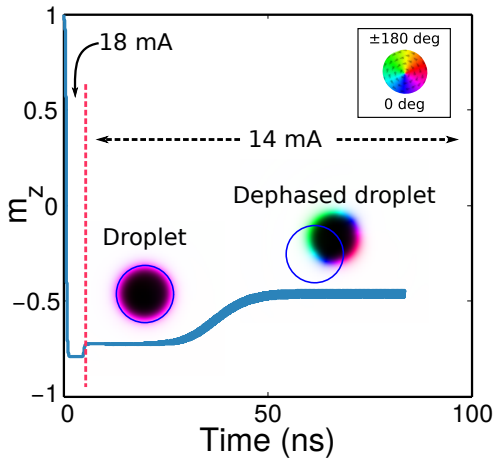

Figure 8.17 **Time evolution of the magnetization inside the nanocontact**. A droplet is created with a current of 18 mA and after 10 ns the current is changed to 13.8 mA (and the corresponding Oersted fields changed as well). The droplet takes a few nanoseconds to reach a new steady state. After an additional 20 to 25 ns, the droplet begins to drift out of the nanocontact and because of an asymmetry caused by the Oersted fields, it dephases. The color scale indicates the direction of the spins at the droplet boundary and show the droplet with the spins at its boundary in phase and dephased.

We simulate the droplet nucleation at the same pulse conditions but with different initial magnetization relaxation times 1.5, 3 and 10 ns. Higher relaxation times means that the magnetization is more close to a complete perpendicular state, which leads to a smaller STT contribution and the creation process take longer since the incubation times becomes higher.

Figure 8.18 shows the waiting time, a measure of the time needed for the creation and annihilation process, with different relaxation times as a function of the current pulse amplitude. The waiting time, t_W, is defined as the time between the application of the pulse and the time with maximum variation of magnetization, calculated as the maximum of the derivative of the magnetization curve, m_z, of the nanocontact versus time. In Fig. 8.18 clear asymmetries between droplet generation and annihilation processes can be observed. The waiting time for the creation process is reduced if the initial magnetization state is strongly tilted, as indicated by the dashed grey line in Fig. 8.18 and this can be achieved by applying an in-plane field pulse during the creation. This data was obtained by the same procedure as that used to obtain the blue curve, with 1.5 ns of relaxation,

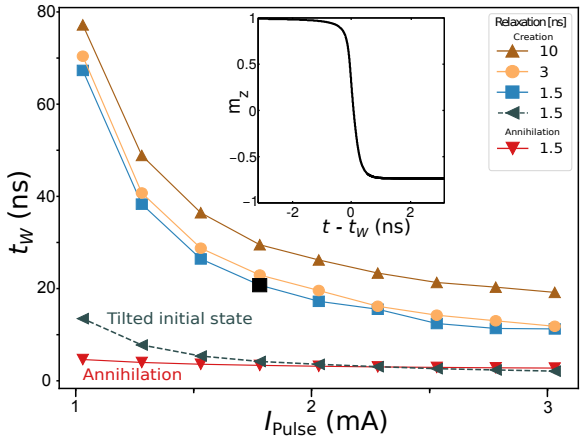

Figure 8.18 **Waiting time for annihilation and creation process as a function of the pulse amplitude**. The red curve shows the annihilation time for different current pulse amplitudes. Droplet annihilation time does not exhibits a strongly dependence on the current-pulse amplitude. The other curves represent the creation processes. The waiting time increases exponentially when the pulse amplitude is reduced and also shows a dependence on the initial state of the magnetization. Different curves are for different initial magnetization states, achieved by using different relaxation times before applying the pulse; pulses were applied after 1.5, 3 and 10 ns of magnetization evolution. The dashed grey line represent a creation process using the same procedure as the blue curve with 1.5 ns of relaxation but with a small in-plane field (5 mT) applied during the current pulse. The inset represents all creation curves, which collapse to one curve when are shifted by their correspondent waiting time. The black square represents the curve in Fig. 8.16B, right panel.

but with a small in-plane field (5 mT) applied during the creation process, to tilt the magnetization away from the z axis. The inset of Fig. 8.18 shows an overlay of the time evolution of magnetization for generation events of different pulse amplitudes, shifted by their individual waiting time, which shows that the generation process is fast and self-similar: the main contribution to the droplet generation time is the time it takes to build up an initial magnetization angle.

8.3 Conclusions

We have studied, with simulations, the conditions required for the nucleation of dynamical skyrmions (DS) and droplet solitons in a metallic nanocontact to a ferromagnetic thin film with PMA. We have shown that both droplet and DS can

be created with a same configuration of applied magnetic field and spin-polarized current by controlling the initial magnetization state, the degree of spin polarized current, or the speed at which the current—or the polarization—is changed. We also propose two plausible methods for the experimental observation of DS.

We reported experimental measurements of the timescales for nucleation and annihilation processes that initially seemed to be different. We found that annihilation occurs in the ns timescale whereas the nucleation timescale is of the order of μs. Simulation were necessary to a better understanding of the droplet incubation time, the required time to building up spin precession angle starting from a small initial angle, and we found that we can be reduced it by increasing the pulse amplitude or creating an initial tilt of the magnetization. We note that the measured annihilation time underestimates the actual droplet lifetime, as it is possible for the droplet to move away from the nanocontact and still exist after application of the pulse.

Chapter 9

General Conclusions

The main result of the first part of the thesis is the simultaneous time- and space-resolved observation of both the piezoelectric voltage wave associated to the SAW and the induced magnetization excitations on the ferromagnetic thin film of Nickel (Ni). We have found that manipulation of magnetization states in ferromagnetic thin films with SAWs is possible at the picosecond scale with efficiencies as high as for the static case. In Chapter 3 we have studied Ni nanostructures whose magnetization dynamics are governed by the intrinsic configuration of the magnetic domains and by their orientation with respect to the SAW-induced strain resulting in considerable delays between strain and magnetization. In Chapter 4 we have studied extended Ni thin films, on which SAWs induce spin waves propagate millimeter distances and have a rotation amplitude of about ±25 deg. We have studied magnetization dynamics on only one magnetostrictive material and there is still further work pending. New materials presenting other properties such as perpendicular magnetic anisotropy or different values of the magnetorestrictive constant should be studied. Additionally, higher frequencies of SAW are becoming available (up to few GHz) and might be the case of study in order to achieve fast and more efficient coupling between SAW and spin waves.

The main results of the second part of the thesis are related with the stability and the nucleation process of magnetic droplet solitons. On the one hand, we have shown that magnetic solitons can exhibit multiple stable states, which are tunable with current or magnetic field. We have also correlated the existence of unstable

states with an increment of low-frequency noise. Using simulations, we have identified the low-frequency spectra with the existence of drift resonances and we have observed that any asymmetry on the effective magnetic field in the magnetic soliton can lead to drift resonances. On the other hand, we have experimentally observed that the processes of nucleation and annihilation of magnetic solitons have different intrinsic time scales, and using simulations we have identified a waiting time associated with the creation process, which makes it much longer than annihilation. We also have studied, using micromagnetic simulations, the initial magnetization states that lead to the nucleation of topological and non-topological magnetic solitons. There is still further work pending in the study of magnetic solitons. Until today, there is no experimental evidence of topological magnetic solitons, which represent a more robust version of the magnetic solitons. Moreover, time-resolved imaging techniques may lead us to understand better the magnetic solitons low-frequency response, which is closely related to their stability.

List of Publications

- S. Lendínez, **N. Statuto**, D. Backes, A. D. Kent, and F. Macià, "Observation of droplet soliton drift resonances in a spin-transfer-torque nanocontact to a ferromagnetic thin film," *Phys. Rev. B*, vol. 92, p. 174426, Nov 2015.

- M. Foerster, F. Macià, **N. Statuto**, S. Finizio, A. Hernández-Mínguez, S. Lendínez, P. V. Santos, J. Fontcuberta, J. M. Hernàndez, M. Kläui, and L. Aballe, "Direct imaging of delayed magneto-dynamic modes induced by surface acoustic waves," *Nat. Comm.*, vol. 8, p. 407, 2017.

- J. Hang, C. Hahn, **N. Statuto**, F. Macià, and A. D. Kent, "Generation and annihilation time of magnetic droplet solitons," *Scientific Reports*, vol. 8, May 2018.

- **N. Statuto**, J. M. Hernàndez, A. D. Kent, and F. Macià, "Generation and stability of dynamical skyrmions and droplet solitons," *Nanotechnology*, vol. 29, p. 325302, June 2018.

- M. Foerster, **N. Statuto**, B. Casals, A. Hernández-Mínguez, S. Finizio, A. Mandziak, L. Aballe, J. M. Hernàndez Ferràs, and F. Macià, "Quantification of propagating and standing surface acoustic waves by stroboscopic X-ray photoemission electron microscopy," *Journal of Synchrotron Radiation*, vol. 26, Jan 2019.

- **N. Statuto**, C. Hahn, J. M. Hernàndez, A. D. Kent, and F. Macià, "Multiple magnetic droplet soliton modes," *in press Phys. Rev. B*, 2019.

Other Publications

- J. Espín, R. Zarzuela, **N. Statuto**, J. Juanhuix, D. Maspoch, I. Imaz, E. Chudnovsky, and J. Tejada, "Narrowing the zero-field tunneling resonance by decreasing the crystal symmetry of mn12 acetate," *Journal of the American Chemical Society*, vol. 138, pp. 9065–9068, July 2016.

- J. Tejada, E. M. Chudnovsky, R. Zarzuela, **N. Statuto**, J. C. de la Rosa, P. V. Santos, and A. Hernández-Mínguez, "Switching of magnetic moments of nanoparticles by surface acoustic waves," *EPL (Europhysics Letters)*, vol. 118, p. 37005, May 2017.

Bibliography

[1] M. Hilbert and P. Lopez, "The worlds technological capacity to store, communicate, and compute information," *Science*, vol. 332, no. 6025, p. 60–65, 2011.

[2] M. Foerster, N. Statuto, B. Casals, A. Hernández-Mínguez, S. Finizio, A. Mandziak, L. Aballe, J. M. Hernàndez Ferràs, and F. Macià, "Quantification of propagating and standing surface acoustic waves by stroboscopic X-ray photoemission electron microscopy," *Journal of Synchrotron Radiation*, vol. 26, Jan 2019.

[3] M. Foerster, F. Macià, N. Statuto, S. Finizio, A. Hernández-Mínguez, S. Lendínez, P. V. Santos, J. Fontcuberta, J. M. Hernàndez, M. Kläui, and L. Aballe, "Direct imaging of delayed magneto-dynamic modes induced by surface acoustic waves," *Nat. Comm.*, vol. 8, p. 407, 2017.

[4] S. Lendínez, N. Statuto, D. Backes, A. D. Kent, and F. Macià, "Observation of droplet soliton drift resonances in a spin-transfer-torque nanocontact to a ferromagnetic thin film," *Phys. Rev. B*, vol. 92, p. 174426, Nov 2015.

[5] N. Statuto, C. Hahn, J. M. Hernàndez, A. D. Kent, and F. Macià, "Multiple magnetic droplet soliton modes," *in press Phys. Rev. B*, 2019.

[6] J. Hang, C. Hahn, N. Statuto, F. Macià, and A. D. Kent, "Generation and annihilation time of magnetic droplet solitons," *Scientific Reports*, vol. 8, May 2018.

[7] N. Statuto, J. M. Hernàndez, A. D. Kent, and F. Macià, "Generation and stability of dynamical skyrmions and droplet solitons," *Nanotechnology*, vol. 29, p. 325302, June 2018.

[8] J. Stöhr and H. C. Siegmann, *Magnetism: From Fundamentals to Nanoscale Dynamics*. Springer Berlin Heidelberg, 2006.

[9] S. J. Blundell, *Magnetism in condensed matter*. Oxford University Press, 2014.

[10] A. A. Timopheev, R. Sousa, M. Chshiev, H. T. Nguyen, and B. Dieny, "Second order anisotropy contribution in perpendicular magnetic tunnel junctions," *Scientific Reports*, vol. 6, Jan 2016.

[11] A. Hubert and W. Rave, "Systematic analysis of micromagnetic switching processes," *physica status solidi (b)*, vol. 211, no. 2, p. 815–829, 1999.

[12] A. Hubert and S. Rudolf, *Magnetic domains: the analysis of magnetic microstructures*. Springer, 1998.

[13] E. M. Chudnovsky and J. Tejada, *Macroscopic Quantum Tunneling of the Magnetic Moment*. Cambridge Univ Pr, 2005.

[14] J. H. E. Griffiths, "Anomalous high-frequency resistance of ferromagnetic metals," *Nature*, vol. 158, no. 4019, p. 670–671, 1946.

[15] S. S. Kalarickal, P. Krivosik, M. Wu, C. E. Patton, M. L. Schneider, P. Kabos, T. J. Silva, and J. P. Nibarger, "Ferromagnetic resonance linewidth in metallic thin films: Comparison of measurement methods," *Journal of Applied Physics*, vol. 99, p. 093909, may 2006.

[16] B. A. Auld, vol. 2. New York: John Wiley and Sons, 1973.

[17] M. F. Lewis, "On Rayleigh waves and propagating acoustic waves," in *Rayleigh-Wave Theory and Application*, vol. 2 of *Springer Series on Wave Phenomena*, pp. 37–58, Springer Berlin Heidelberg, 1985.

[18] J. Åkerman, "Toward a universal memory," *Science*, vol. 308, no. 5721, pp. 508–510, 2005.

[19] N. Locatelli, V. Cros, and J. Grollier, "Spin-torque building blocks," *Nat. Materials*, vol. 13, pp. 11–20, 2014.

[20] D. Chiba, M. Sawicki, Y. Nishitani, Y. Nakatani, F. Matsukura, and H. Ohno, "Magnetization vector manipulation by electric fields," *Nature*, vol. 455, pp. 515–518, sep 2008.

[21] Y.-H. Chu, L. W. Martin, M. B. Holcomb, M. Gajek, S.-J. Han, Q. He, N. Balke, C.-H. Yang, D. Lee, W. Hu, Q. Zhan, P.-L. Yang, A. Fraile-rodríguez, A. Scholl, S. X. Wang, and R. Ramesh, "Erratum: Electric-field control of local ferromagnetism using a magnetoelectric multiferroic," *Nature Materials*, vol. 7, pp. 678–678, aug 2008.

[22] A. Bur, T. Wu, J. Hockel, C.-J. Hsu, H. K. D. Kim, T.-K. Chung, K. Wong, K. L. Wang, and G. P. Carman, "Strain-induced magnetization change in patterned ferromagnetic nickel nanostructures," *Journal of Applied Physics*, vol. 109, p. 123903, jun 2011.

[23] J. L. Hockel, A. Bur, T. Wu, K. P. Wetzlar, and G. P. Carman, "Electric field induced magnetization rotation in patterned ni ring/pb(mg1/3nb2/3)o3](1-0.32)-[PbTiO3]0.32 heterostructures," *Applied Physics Letters*, vol. 100, p. 022401, jan 2012.

[24] S. Finizio, M. Foerster, M. Buzzi, B. Krüger, M. Jourdan, C. A. F. Vaz, J. Hockel, T. Miyawaki, A. Tkach, S. Valencia, F. Kronast, G. P. Carman, F. Nolting, and M. Kläui, "Magnetic anisotropy engineering in thin film ni nanostructures by magnetoelastic coupling," *Phys. Rev. Applied*, vol. 1, p. 021001, Mar 2014.

[25] I. Yeo, P.-L. de Assis, A. Gloppe, E. Dupont-Ferrier, P. Verlot, N. S. Malik, E. Dupuy, J. Claudon, J.-M. Gérard, A. Auffèves, G. Nogues, S. Seidelin, J.-P. Poizat, O. Arcizet, and M. Richard, "Strain-mediated coupling in a quantum dot–mechanical oscillator hybrid system," *Nature Nanotechnology*, vol. 9, pp. 106–110, dec 2013.

[26] J. Hernandez, M. F. Santos, P.V. and, G.-S. A., and J. Tejada, "Acoustomagnetic pulse experiments in $linbo_3/mn_{12}$ hybrids," *Appl. Phys. Lett.*, vol. 88, p. 012503, 2006.

[27] X. Li, D. Labanowski, S. Salahuddin, and C. S. Lynch, "Spin wave generation by surface acoustic waves," *Journal of Applied Physics*, vol. 122, p. 043904, jul 2017.

[28] A. V. Scherbakov, A. S. Salasyuk, A. V. Akimov, X. Liu, M. Bombeck, C. Brüggemann, D. R. Yakovlev, V. F. Sapega, J. K. Furdyna, and M. Bayer, "Coherent magnetization precession in ferromagnetic (ga,mn)as induced by picosecond acoustic pulses," *Phys. Rev. Lett.*, vol. 105, p. 117204, Sep 2010.

[29] S. Davis, Baruth, and S. Adenwalla, "Magnetization dynamics triggered by surface acoustic waves," *Appl. Phys. Lett.*, vol. 97, p. 232507, 2010.

[30] L. Thevenard, I. S. Camara, S. Majrab, M. Bernard, P. Rovillain, A. Lemaître, C. Gourdon, and J.-Y. Duquesne, "Precessional magnetization switching by a surface acoustic wave," *Phys. Rev. B*, vol. 93, p. 134430, Apr 2016.

[31] J. Tejada, E. M. Chudnovsky, R. Zarzuela, N. Statuto, J. C. de la Rosa, P. V. Santos, and A. Hernández-Mínguez, "Switching of magnetic moments of nanoparticles by surface acoustic waves," *EPL (Europhysics Letters)*, vol. 118, p. 37005, May 2017.

[32] M. Weiler, H. Huebl, F. S. Goerg, F. D. Czeschka, R. Gross, and S. T. B. Goennenwein, "Spin pumping with coherent elastic waves," *Phys. Rev. Lett.*, vol. 108, p. 176601, Apr 2012.

[33] M. Weiler, L. Dreher, C. Heeg, H. Huebl, R. Gross, M. S. Brandt, and S. T. B. Goennenwein, "Elastically driven ferromagnetic resonance in nickel thin films," *Phys. Rev. Lett.*, vol. 106, p. 117601, Mar 2011.

[34] V. Kavalerov, T. Fujii, and M. Inoue, "Observation of highly nonlinear surface-acoustic waves on single crystal lithium–niobate plates by means of an optical sampling probe," *Journal of Applied Physics*, vol. 87, no. 2, pp. 907–913, 2000.

[35] B. Capelle, Y. Epelboin, A. Soyer, and J. Détaint, "Observation of surface acoustic waves using synchrotron radiation x-ray topography," pp. 1–6, May 2012.

[36] "Roditi international, http://www.roditi.com/singlecrystal/linbo3," 2019.

[37] "Circe endstation at alba, https://intranet.cells.es/beamlines/circe," 2019.

[38] R. Munoz Horta, G. Benedetti, D. Lanaia, J. Moldes, F. Pérez, M. Pont, and L. Torino, "Single bunch bucket selection injection modes in the alba storage ring," *Proceedings of the 8th Int. Particle Accelerator Conf.*, vol. IPAC2017, pp. Denmark–, 2017.

[39] T. Schmidt, S. Heun, J. Slezak, J. Diaz, K. C. Prince, G. Lilienkamp, and E. Bauer, "SPELEEM: Combining LEEM and spectroscopic imaging," *Surface Review and Letters*, vol. 05, pp. 1287–1296, dec 1998.

[40] M. Foerster, J. Prat, V. Massana, N. Gonzalez, A. Fontsere, B. Molas, O. Matilla, E. Pellegrin, and L. Aballe, "Custom sample environments at the alba xpeem," *Ultramicroscopy*, vol. 171, pp. 63 – 69, 2016.

[41] O. Matilla, D. Beltran, D. Fernandez-Carreiras, J. Jan Jamroz, J. Klora, J. Moldes, and R. Sune, "Alba timing system - a known architecture with fast interlock system upgrade," *Proceedings of ICALEPCS*, p. 1423, 2012.

[42] F. W. Beil, A. Wixforth, W. Wegscheider, D. Schuh, M. Bichler, and R. H. Blick, "Shock waves in nanomechanical resonators," *Phys. Rev. Lett.*, vol. 100, p. 026801, Jan 2008.

[43] M. M. de Lima, P. V. Santos, Y. A. Kosevich, and A. Cantarero, "Tunable coupled surface acoustic cavities," *Applied Physics Letters*, vol. 100, no. 26, p. 261904, 2012.

[44] J. Raabe, C. Quitmann, C. H. Back, F. Nolting, S. Johnson, and C. Buehler, "Quantitative analysis of magnetic excitations in landau flux-closure structures using synchrotron-radiation microscopy," *Phys. Rev. Lett.*, vol. 94, p. 217204, Jun 2005.

[45] A. Vansteenkiste, J. Leliaert, M. Dvornik, M. Helsen, F. Garcia-Sanchez, and B. VanWaeyenberge, "The design and verification of mumax3," *AIP Adv.*, p. 107133, 2014.

[46] T. McGuire and R. Potter, "Anisotropic magnetoresistance in ferromagnetic 3d alloys," *IEEE Trans. Magn.*, vol. 11, pp. 1018–1038, July 1975.

[47] G. Binasch, P. Grünberg, F. Saurenbach, and W. Zinn, "Enhanced magnetoresistance in layered magnetic structures with antiferromagnetic interlayer exchange," *Phys. Rev. B*, vol. 39, pp. 4828–4830, Mar 1989.

[48] M. N. Baibich, J. M. Broto, A. Fert, F. N. V. Dau, F. Petroff, P. Etienne, G. Creuzet, A. Friederich, and J. Chazelas, "Giant magnetoresistance of (001)fe/(001)cr magnetic superlattices," *Physical Review Letters*, vol. 61, no. 21, p. 2472–2475, 1988.

[49] M. Julliere, "Tunneling between ferromagnetic films," *Phys. Lett. A*, vol. 54, pp. 225–226, Sept. 1975.

[50] G. Jonker and J. V. Santen, "Ferromagnetic compounds of manganese with perovskite structure," *Physica*, vol. 16, pp. 337–349, Mar. 1950.

[51] S. A. Solin, "Enhanced room-temperature geometric magnetoresistance in inhomogeneous narrow-gap semiconductors," *Science*, vol. 289, pp. 1530–1532, Sept. 2000.

[52] R. Càndid, S. Cardoso, and S. C. Mukhopadhyay, *Giant magnetoresistance (GMR) sensors: from basis to state-of-the-art applications.* Springer, 2015.

[53] J. C. Slonczewski, "Current-driven excitation of magnetic multilayers," *J. Magn. Magn. Mater.*, vol. 159, pp. L1–L7, June 1996.

[54] A. D. Kent, "Spin-transfer in high magnetic fields and single magnetic layer nanopillars," *Handbook of Magnetism and Advanced Magnetic Materials*, 2007.

[55] B. Divinskiy, S. Urazhdin, V. E. Demidov, A. Kozhanov, A. P. Nosov, A. B. Rinkevich, and S. O. Demokritov, "Magnetic droplet solitons generated by pure spin currents," *Phys. Rev. B*, vol. 96, p. 224419, Dec 2017.

[56] J. E. Hirsch, "Spin hall effect," *Phys. Rev. Lett.*, vol. 83, pp. 1834–1837, Aug 1999.

[57] A. Brataas, A. D. Kent, and H. Ohno, "Current-induced torques in magnetic materials.," *Nat. Mater.*, vol. 11, pp. 372–81, May 2012.

[58] J. Grollier, V. Cros, A. Hamzic, J. M. George, H. Jaffrès, A. Fert, G. Faini, J. B. Youssef, and H. Legall, "Spin-polarized current induced switching in co/cu/co pillars," *Applied Physics Letters*, vol. 78, pp. 3663–3665, jun 2001.

[59] S. Boyn, J. Sampaio, V. Cros, J. Grollier, A. Fukushima, H. Kubota, K. Yakushiji, and S. Yuasa, "Twist in the bias dependence of spin torques in magnetic tunnel junctions," *Physical Review B*, vol. 93, jun 2016.

[60] L. Heyne, J. Rhensius, D. Ilgaz, A. Bisig, U. Rüdiger, M. Kläui, L. Joly, F. Nolting, L. J. Heyderman, J. U. Thiele, and F. Kronast, "Direct determination of large spin-torque nonadiabaticity in vortex core dynamics," *Physical Review Letters*, vol. 105, oct 2010.

[61] F. Macià, A. D. Kent, and F. C. Hoppensteadt, "Spin-wave interference patterns created by spin-torque nano-oscillators for memory and computation.," *Nanotechnology*, vol. 22, p. 095301, Mar. 2011.

[62] S. M. Mohseni, S. R. Sani, J. Persson, T. N. A. Nguyen, S. Chung, Y. Pogoryelov, P. K. Muduli, E. Iacocca, A. Eklund, R. K. Dumas, S. Bonetti, A. Deac, M. A. Hoefer, and J. Åkerman, "Spin torque-generated magnetic droplet solitons.," *Science*, vol. 339, pp. 1295–8, Mar. 2013.

[63] F. Macià, D. Backes, and A. D. Kent, "Stable magnetic droplet solitons in spin-transfer nanocontacts.," *Nat. Nanotechnol.*, vol. 9, pp. 992–6, Dec. 2014.

[64] Q. Mistral, M. van Kampen, G. Hrkac, J.-V. Kim, T. Devolder, P. Crozat, C. Chappert, L. Lagae, and T. Schrefl, "Current-driven vortex oscillations in metallic nanocontacts," *Physical Review Letters*, vol. 100, jun 2008.

[65] A. M. Kosevich, B. A. Ivanov, and A. S. Kovalev, "Magnetic Solitons," *Phys. Rep.*, vol. 194, pp. 117–238, Oct. 1990.

[66] B. A. Ivanov and A. M. Kosevich, "Bound states of large number of magnons in a three-dimensional ferromagnet (magnons drops)," *Zh. Eksp. Teor. Fiz.*, vol. 24, no. 9, pp. 495–499, 1976.

[67] M. A. Hoefer, T. J. Silva, and M. W. Keller, "Theory for a dissipative droplet soliton excited by a spin torque nanocontact," *Phys. Rev. B*, vol. 82, p. 054432, Aug. 2010.

[68] S. Heinze, K. von Bergmann, M. Menzel, J. Brede, A. Kubetzka, R. Wiesendanger, G. Bihlmayer, and S. Blügel, "Spontaneous atomic-scale magnetic skyrmion lattice in two dimensions," *Nat. Phys.*, vol. 7, pp. 713–718, July 2011.

[69] L. Berger, "Low-field magnetoresistance and domain drag in ferromagnets," *Journal of Applied Physics*, vol. 49, pp. 2156–2161, mar 1978.

[70] P. P. Freitas and L. Berger, "Observation ofs-dexchange force between domain walls and electric current in very thin permalloy films," *Journal of Applied Physics*, vol. 57, pp. 1266–1269, feb 1985.

[71] C.-Y. Hung and L. Berger, "Exchange forces between domain wall and electric current in permalloy films of variable thickness," *Journal of Applied Physics*, vol. 63, pp. 4276–4278, apr 1988.

[72] L. Berger, "Emission of spin waves by a magnetic multilayer traversed by a current," *Phys. Rev. B*, vol. 54, pp. 9353–9358, Oct. 1996.

[73] J. A. Katine, F. J. Albert, R. A. Buhrman, E. B. Myers, and D. C. Ralph, "Current-Driven Magnetization Reversal and Spin-Wave Excitations in Co / Cu / Co Pillars," *Phys. Rev. Lett.*, vol. 84, pp. 3149–3152, Apr. 2000.

[74] E. B. Myers, "Current-Induced Switching of Domains in Magnetic Multilayer Devices," *Science*, vol. 285, pp. 867–870, Aug. 1999.

[75] S. I. Kiselev, J. C. Sankey, I. N. Krivorotov, N. C. Emley, R. J. Schoelkopf, R. A. Buhrman, and D. C. Ralph, "Microwave oscillations of a nanomagnet driven by a spin-polarized current.," *Nature*, vol. 425, pp. 380–3, Sept. 2003.

[76] W. Rippard, M. Pufall, S. Kaka, S. Russek, and T. Silva, "Direct-Current Induced Dynamics in $Co_{90}Fe_{10}$ / $Ni_{80}Fe_{20}$ Point Contacts," *Phys. Rev. Lett.*, vol. 92, p. 027201, Jan. 2004.

[77] S. Bonetti, V. Tiberkevich, G. Consolo, G. Finocchio, P. Muduli, F. Mancoff, A. Slavin, and J. Åkerman, "Experimental Evidence of Self-Localized and Propagating Spin Wave Modes in Obliquely Magnetized Current-Driven Nanocontacts," *Phys. Rev. Lett.*, vol. 105, p. 217204, Nov. 2010.

[78] S. Chung, S. M. Mohseni, S. R. Sani, E. Iacocca, R. K. Dumas, T. N. Anh Nguyen, Y. Pogoryelov, P. K. Muduli, A. Eklund, M. Hoefer, and J. Åkerman, "Spin transfer torque generated magnetic droplet solitons (invited)," *J. Appl. Phys.*, vol. 115, p. 172612, May 2014.

[79] S. M. Mohseni, S. R. Sani, R. K. Dumas, J. Persson, T. N. Anh Nguyen, S. Chung, Y. Pogoryelov, P. K. Muduli, E. Iacocca, A. Eklund, and J. Åkerman, "Magnetic droplet solitons in orthogonal nano-contact spin torque oscillators," *Phys. B Condens. Matter*, vol. 435, pp. 84–87, Feb. 2014.

[80] D. Backes, F. Macià, S. Bonetti, R. Kukreja, H. Ohldag, and A. D. Kent, "Direct observation of a localized magnetic soliton in a spin-transfer nanocontact," *Phys. Rev. Lett.*, vol. 115, p. 127205, Sep 2015.

[81] Y. Zhou, E. Iacocca, A. A. Awad, R. K. Dumas, F. C. Zhang, H. B. Braun, and J. Åkerman, "Dynamically stabilized magnetic skyrmions," *Nat. Commun.*, vol. 6, p. 8193, Sep 2015.

[82] F. Macià, P. Warnicke, D. Bedau, M.-Y. Im, P. Fischer, D. Arena, and A. Kent, "Perpendicular magnetic anisotropy in ultrathin Co|Ni multilayer films studied with ferromagnetic resonance and magnetic x-ray microspectroscopy," *J. Magn. Magn. Mater.*, vol. 324, pp. 3629–3632, Nov. 2012.

[83] P. Wills, E. Iacocca, and M. A. Hoefer, "Deterministic drift instability and stochastic thermal perturbations of magnetic dissipative droplet solitons," *Phys. Rev. B*, vol. 93, p. 144408, Apr 2016.

[84] V. E. Demidov, S. Urazhdin, and S. O. Demokritov, "Direct observation and mapping of spin waves emitted by spin-torque nano-oscillators," *Nat. Mater.*, vol. 9, p. 984, 2010.

[85] S. Bonetti, R. Kukreja, Z. Chen, F. Macià, J. M. Hernàndez, A. Eklund, D. Backes, J. Frisch, J. Katine, G. Malm, S. Urazhdin, A. D. Kent, J. Stöhr, H. Ohldag, and H. A. Dürr, "Direct observation and imaging of a spin-wave soliton with p-like symmetry," *Phys. Rev. B*, vol. 6, no. Nat. Communications, p. 8889, 1996.

[86] I. Dzyaloshinsky, "A thermodynamic theory of "weak" ferromagnetism of antiferromagnetics," *Journal of Physics and Chemistry of Solids*, vol. 4, no. 4, pp. 241 – 255, 1958.

[87] T. Moriya, "Anisotropic superexchange interaction and weak ferromagnetism," *Phys. Rev.*, vol. 120, pp. 91–98, Oct 1960.

[88] S. Chung, S. M. Mohseni, A. Eklund, P. Dürrenfeld, M. Ranjbar, S. R. Sani, T. N. Anh Nguyen, R. K. Dumas, and J. Åkerman, "Magnetic droplet solitons in orthogonal spin valves," *Low Temp. Phys.*, vol. 41, p. 833, 2015.

[89] S. Chung, A. Eklund, E. Iacocca, S. M. Mohseni, S. R. Sani, L. Bookman, M. A. Hoefer, R. K. Dumas, and J. Äkerman, "Magnetic droplet nucleation boundary in orthogonal spin-torque nano-oscillators," *Nature Communications*, vol. 7, p. 11209, 2016.

[90] R. H. Liu, W. L. Lim, and S. Urazhdin, "Dynamical skyrmion state in a spin current nano-oscillator with perpendicular magnetic anisotropy," *Phys. Rev. Lett.*, vol. 114, p. 137201, Mar 2015.

[91] S. Lendínez, J. Hang, S. Vélez, J. M. Hernández, D. Backes, A. D. Kent, and F. Macià, "Effect of temperature on magnetic solitons induced by spin-transfer torque," *Phys. Rev. Applied*, vol. 7, p. 054027, May 2017.

[92] S. Chung, Q. T. Le, M. Ahlberg, A. A. Awad, M. Weigand, I. Bykova, R. Khymyn, M. Dvornik, H. Mazraati, A. Houshang, S. Jiang, T. N. A. Nguyen, E. Goering, G. Schütz, J. Gräfe, and J. Åkerman, "Direct observation of zhang-li torque expansion of magnetic droplet solitons," *Phys. Rev. Lett.*, vol. 120, p. 217204, May 2018.

[93] J. Z. Sun, "Spin-current interaction with a monodomain magnetic body: A model study," *Phys. Rev. B*, vol. 62, p. 570, July 2000.

[94] T. Devolder, J. Hayakawa, K. Ito, H. Takahashi, S. Ikeda, P. Crozat, N. Zerounian, J. Kim, C. Chappert, and H. Ohno, "Single-Shot Time-Resolved measurements of Nanosecond-Scale Spin-Transfer induced switching: Stochastic versus deterministic aspects," *Physical Review Letter*, vol. 100, pp. 057206–4, Feb. 2008.

Appendix A

Micromagnatic Simulations

All numerical simulations along the thesis were performed using a MuMax^3 code [45] on a graphics card with 2048 processing cores. MuMax^3 calculates the space- and time-dependent magnetization dynamics in nano- to micro-sized ferromagnets using a finite-difference discretization. Simulation solves the Landau–Lifshitz–Gilbert–Slonczewski equation to describe the magnetization dynamics.

A.1 Ni Nanostructures and SAWs Simulations

A 2048×2048×20 (with units in nm) grid was consider for the simulations. Simulations solve the Landau–Lifshitz–Gilbert equation for describe magnetization dynamics. In addition to Ni uniaxial anisotropy an oscillating term of uniaxial anisotropy was added to take into account the SAWs interaction. The new term has a wavelength set by the SAW ($\lambda_{SAW} \approx 8\ \mu$m) and simulations covered frequencies from 10s of MHz to 10s of GHz.

Parameters

The parameters of the magnetic layer, a Nickel film, were taken from the sample characterization: saturation magnetization $M_s = 490 \cdot 10^3$ (A/m), Gilbert damping

constant $\alpha = 0.03$, exchange stiffness constant $A_{ex} = 5 \cdot 10^{-12}$ (J/m) and an uniaxial anisotropy $K_u = 1.2 \cdot 10^3$ (J/m^3).

A.1.1 Code for the Ni Thin Film with SAWs

Full code of the excitation of Ni thin film with SAW is provided. The initial state of the simulation is the *Landau flux closure state* and is defined as *m = vortex(1,1)*.

```
//GRID
NumCells := 512
CellSize:=4.e-9
SetGridSize(NumCells, NumCells, 1)
SetCellSize(CellSize, CellSize, 20.e-9)
Setgeom(universe())

//MATERIAL PARAMETERS FOR STANDARD Ni
Msat = 490e3 //Saturation
Ku1 = 200e3 //Uniaxial Anisotropy
Aex = 5·10e-12 //Exchange
alpha = 0.03 //Damping

//INITIAL MAGNETIZATION STATE
m = vortex(1,1)

//REGIONS
MaxRegion:=200
CellsPerRegion:=NumCells/MaxRegion
RegionWidth:=CellsPerRegion*CellSize
SampleCenter:= CellSize*NumCells/2.


    for i:=0; i<=MaxRegion; i++ {
        defregion(i, xrange(i*RegionWidth-SampleCenter,1))
}

//DEFINING ANISOTROPY VECTOR
for i:=0; i<=MaxRegion; i++{
        AnisU.SetRegion(i,vector(1.,0.,0.))
}
//DEFINING ANISOTROPY CONSTANT
freq:=500000. //SAW freq
Kuav:=1.2e3 //Nominal Anisotropy
Kumod:=1.e3
Lambd:=4. //in sample width units
for i:=0; i<=MaxRegion; i++{
        ku1.SetRegion(i, Kuav + Kumod * cos( 2*pi*((i* 1/MaxRegion -0.5)/Lambd - freq*t)))
}
relax()
Run(20e-9)
```

A.2 Droplet and Dynamical Skyrmion Simulations

For the simulation of both topological and non-topological magnetic solitons, Part II, we fixed the material parameters we measured experimentally [4, 63] in a circle nanocontact of 100-150 nm in diameter. In addition to the LLG equation Slonczewski term was also added in order to introduce the spin-transfer torque to simulations.

Parameters

We used a damping parameter $\alpha = 0.03$ and adjusted the spin torque efficiency, the polarization, to obtain a droplet onset map similar to measurements. Oersted fields effect were also taking into the account. The value for the saturation was $M_s = 500 \cdot 10^3$ (A/m), the uniaxial anisotropy constant $K_u = 200 \cdot 10^3$ (J/m^3) and the exchange stiffness constant $A_{ex} = 10^{-12}$ (J/m).
We consider a 1024×1024×4 (with units in nm) grid. Then, a circular region of 100 - 150 nm was consider as the nanocontact, the region where the current was applied.

A.2.1 Code for the Excitation of a Droplet or a DS

Full code of the excitation of a droplet or a dynamical skyrmions (DS) is provided. In order to obtain one or the other just the *angle* should be modified.

```
//GRID
NumCells := 256
CellSize:=4.e-9
SetGridSize(NumCells, NumCells, 1)
SetCellSize(CellSize, CellSize, CellSize)
SETPBC(4, 4, 0)

//REGIONS
setGeom(layer(0))
diam_circ := 150e-9
r_circ := diam_circ / 2
A_circ := pi * pow(r_circ, 2)
DefRegion(1, layer(0).intersect(circle(diam_circ)))

//MATERIAL PARAMETERS FOR STANDARD CoNi
```

```
lambda = 1 //Slonczewski parameter
epsilonprime = 0 // Slonczewski secondairy STT term
Msat = 500e3 //Saturation
Ku1 = 200e3 //Uniaxial Anisotropy
anisU = vector(0, 0, 1)
Aex = 10e-12 //Exchange
alpha = 0.03 //Damping

//OERSTED FIELDS————————————
posX := 0.
posY := 0.
mask := newSlice(3, LL, LL, Lz)
current := vector(0., 0., 1.)

for i := 0; i < LL; i++ {
        for j := 0; j < LL; j++ {
            r := index2coord(i, j, 0)
            r = r.sub(vector(posX, posY, 0))
            b := vector(0, 0, 0)
            if r.len() >= r_circ {
               b = r.cross(current).mul(mu0 / (2 * pi * r.len() * r.len()))
            }
        else {
               b = r.cross(current).mul(mu0 / (2 * pi * r_circ * r_circ))
            }
        for k := 0; k < Lz; k++ {
            mask.set(0, i, j, k, b.X())
            mask.set(1, i, j, k, b.Y())
            mask.set(2, i, j, k, b.Z())
            }
        }
}
//END OERSTED———————————————

//RUNNING
B_ext.RemoveExtraTerms()
Curr := -30e-3
B_ext = vector(0, 0, 0.5)
Pol = 0.45
Angle := 85.0 //use 89.9 for dynamical skyrmion
my := cos(angle * pi / 180)
mz := sin(angle * pi / 180)
m = Uniform(0, my, mz)

j.SetRegion(1, vector(0, 0, Curr/A_circ))
B_ext.RemoveExtraTerms()
B_ext.add(mask, Curr)
Run(20e-9)
```